Paired Pulse Basis Functions and Triangular Patch Modeling for the Method of Moments Calculation of Electromagnetic Scattering from Three-Dimensional, Arbitrarily-Shaped Bodies

Except where reference is made to the work of others, the work described in this dissertation is my own or was done in collaboration with my advisory committee. This dissertation does not include proprietary or classified information.

Anne I. Mackenzie

Certificate of Approval:

Lloyd S. Riggs
Professor
Electrical and Computer Engineering

Sadasiva M. Rao, Chair
Professor
Electrical and Computer Engineering

Stuart M. Wentworth
Associate Professor
Electrical and Computer Engineering

Hulya Kirkici
Associate Professor
Electrical and Computer Engineering

George T. Flowers
Dean
Graduate School

Paired Pulse Basis Functions and Triangular Patch Modeling for the Method of Moments Calculation of Electromagnetic Scattering from Three-Dimensional, Arbitrarily-Shaped Bodies

Anne I. Mackenzie

A Dissertation

Submitted to

the Graduate Faculty of

Auburn University

in Partial Fulfillment of the

Requirements for the

Degree of

Doctor of Philosophy

Auburn, Alabama
December 19, 2008

Paired Pulse Basis Functions and Triangular Patch Modeling for the Method of Moments Calculation of Electromagnetic Scattering from Three-Dimensional, Arbitrarily-Shaped Bodies

Anne I. Mackenzie

Permission is granted to Auburn University to make copies of this dissertation at its discretion, upon the request of individuals or institutions and at their expense. The author reserves all publication rights.

Signature of Author

Date of Graduation

Vita

Anne Isobel Mackenzie was born in Cottingham, Yorkshire, England on March 16, 1953. Her parents, James Ross and Veronica Mackenzie, who were medical doctors, emigrated with Anne in 1956 to Canada. After attending grade school in Woodstock, Ontario and secondary schools in Corpus Christi, Texas and Indianapolis, Indiana, Anne attended Purdue University in West Lafayette, Indiana, where she obtained a B.S. degree in General Biology (1974). While working for the Biology Department at the Indiana University-Purdue University campus at Indianapolis, she completed an A.A.S. degree in Electrical Engineering Technology (1980). She then worked for five years as an electronics repair technician at Wavetek Electronics in Beech Grove, Indiana. Following this period, Anne obtained a B.S. degree in Electrical Engineering (1986) from Purdue University in Indianapolis and moved to Virginia to work at the NASA Langley Research Center, where she is still employed as a researcher in the Electromagnetics & Sensors Branch. Anne obtained an M.S. degree in Electrical Engineering from Virginia Tech in 1992. Her work at NASA has included weather radar analysis and design, radiometry, materials measurements, and electromagnetic modeling. Anne's parents and her siblings, Judith Marie Mackenzie, Veronica Jane Martin, and James Willis Mackenzie, now reside in Indianapolis, Indiana.

Dissertation Abstract

Paired Pulse Basis Functions and Triangular Patch Modeling for the Method of Moments Calculation of Electromagnetic Scattering from Three-Dimensional, Arbitrarily-Shaped Bodies

Anne I. Mackenzie

Doctor of Philosophy, December 19, 2008
(M.S.E.E., Virginia Polytechnic Institute and State University, 1992)
(B.S.E., Purdue University, 1986)

106 Typed Pages

Directed by Sadasiva M. Rao

Due to an increasing emphasis on fabrication with composite materials, it is important to be able to model accurately the electromagnetic properties of composite structures. In this work, we demonstrate a new pair of orthogonal pulse vector basis functions for the calculation of electromagnetic scattering from arbitrarily-shaped material bodies. These subdomain basis functions are intended for use with triangular surface patch modeling applied to a method of moments (MoM) solution. For modeling the behavior of dielectric materials, several authors have used the same set of basis functions to represent equivalent electric and magnetic surface currents. This practice can result in zero-valued or very small diagonal terms in the moment matrix and an unstable numerical solution. To provide a more stable solution, we have developed orthogonally placed, pulse basis vectors: one for the electric surface current and one for the magnetic surface current. The basis function for the electric surface current is placed perpendicular to each patch edge, while the basis function for the magnetic surface current is placed parallel to each patch edge. This combination, together with appropriate testing functions, ensures strongly diagonal moment matrices. The basis functions are suitable for implementing solutions using the

electric field integral equation (EFIE) or the magnetic field integral equation (HFIE.) To obtain unique solutions at all frequencies, including characteristic frequencies for closed bodies, the EFIE and HFIE may be expanded with paired pulse vector basis functions and then arithmetically combined by any of the combined-field methods such as combined field integral equation (CFIE), Poggio-Miller-Chang-Harrington-Wu-Tsai (PMCHWT), or Müller formulations. In this work, we describe the numerical implementations of EFIE and HFIE solutions and show example results for three-dimensional, canonical figures. Those scattering results obtained by using pulse vector basis functions are compared to results obtained from an exact method or a more accurate numerical method specialized for a particular type of geometry, such as a body of revolution. In successive chapters, the numerical procedures and solutions are shown for perfect conductors (PEC's), dielectric bodies, and PEC/dielectric composites. The composite scatterers may contain multiple dielectric and PEC parts, either touching or non-touching.

Acknowledgments

I wish to acknowledge my major professor, Dr. S. M. Rao, for sharing his insights into electromagnetics during the past four years. Dr. Mike Baginski has provided much practical help and encouragement, and without him I may not have embarked on this most recent adventure. My undergraduate teachers Drs. Ahmet Fer and Han Paik inspired me to start off in this direction many years ago. Thanks to the faculty and staff of Auburn University who did more than they had to. Thanks to NASA Langley Research Center for giving me the time to work on this graduate degree. Thanks to all of my family, friends, and coworkers, who were surprisingly positive about the whole thing. Early in my mathematical career, Dad recognized the importance of the directed segment. And thanks to Kitty Columbus, who was a constant friend for as long as he could be.

Style manual or journal used IEEE Editorial Style Manual (together with the Auburn dissertation style known as "auphd.")

Computer software used The document preparation package LaTeX2e together with the style file auphd.sty. Figures were prepared with MATLAB, PowerPoint, and Acrobat.

Table of Contents

List of Figures xi

List of Tables xiv

1 Introduction 1
1.1 Overview . . . 1
1.2 Background . . . 1
1.2.1 Scattering Solutions . . . 1
1.2.2 Method of Moments . . . 3
1.3 Statement of the Problem . . . 6
1.4 The Proposed Method . . . 7
1.5 Scope . . . 9
1.6 Organization . . . 10

2 New Basis Functions for the Electromagnetic Solution of Arbitrarily-shaped, Three-dimensional Conducting Bodies Using Method of Moments 11
2.1 Overview . . . 11
2.2 Introduction . . . 11
2.3 Description of the Problem . . . 12
2.4 Description of Basis Functions . . . 13
2.5 Numerical Solution Procedure . . . 15
2.6 Numerical Results . . . 18
2.7 Summary . . . 18

3 An Alternate Set of Basis Functions for the Electromagnetic Solution of Arbitrarily-Shaped, Three-Dimensional, Closed Conducting Bodies Using Method of Moments 22
3.1 Overview . . . 22
3.2 Introduction . . . 22
3.3 Description of the Problem . . . 23
3.4 Description of Basis Functions . . . 24
3.5 Numerical Solution Procedure . . . 26
3.6 Numerical Results . . . 30
3.7 Summary . . . 31

4 Electromagnetic Scattering from Arbitrarily-Shaped Dielectric Bodies Using Paired Pulse Vector Basis Functions and Method of Moments 34
4.1 Overview . . . 34
4.2 Introduction . . . 34
4.3 Integral Equations . . . 36
4.4 Basis and Testing Functions . . . 39
4.5 Numerical Solution Procedure . . . 40
4.5.1 Calculation of $\boldsymbol{A}$ and $\boldsymbol{F}$ . . . 45
4.5.2 Calculation of $\nabla \times \boldsymbol{F}$ and $\nabla \times \boldsymbol{A}$ . . . 46
4.5.3 Calculation of Φ and Ψ . . . 46
4.5.4 Testing the Incident Fields . . . 51
4.6 Numerical Examples . . . 51
4.7 Summary . . . 56

5 Electromagnetic Scattering from Arbitrarily Shaped Composites Using Paired Pulse Vector Basis Functions and Method of Moments 57
5.1 Overview . . . 57
5.2 Introduction . . . 57
5.3 Integral Equations . . . 59
5.4 Basis and Testing Functions . . . 63
5.5 Numerical Solution Procedure . . . 65
5.5.1 Calculation of $\boldsymbol{A}$ and $\boldsymbol{F}$ . . . 68
5.5.2 Calculation of $\nabla \times \boldsymbol{F}$ and $\nabla \times \boldsymbol{A}$ . . . 69
5.5.3 Calculation of Φ and Ψ . . . 69
5.5.4 Testing the Incident Fields . . . 74
5.6 Numerical Examples . . . 74
5.7 Summary . . . 80

6 Conclusion 81

Bibliography 83

Appendices 86

A Derivation of Dielectric Field Equations 87

B Pulse Basis Functions in EFIE and HFIE Solutions 91

List of Figures

1.1 Basis functions $\boldsymbol{f}_n$ and $\boldsymbol{g}_n$ associated with the n^{th} edge. 7

1.2 Testing functions $\boldsymbol{t}_m$ and $\boldsymbol{\ell}_m$ associated with the m^{th} edge. 9

2.1 Arbitrarily-shaped conducting body excited by an incident electromagnetic plane wave. 12

2.2 Basis function description. 14

2.3 Testing paths associated with the m^{th} edge. 15

2.4 Electric charge patch within the T_i^{th} triangle. 17

2.5 Bistatic RCS of a square plate of length $0.15\,\lambda$ excited by a plane wave traveling in the -z direction. 19

2.6 Bistatic RCS of a circular disk of diameter $0.15\,\lambda$ excited by a plane wave traveling in the -z direction. 20

2.7 Bistatic RCS of a sphere of diameter $0.15\,\lambda$ excited by a plane wave traveling in the -z direction. 20

2.8 Bistatic RCS of a circular cylinder of diameter $0.15\,\lambda$ and height $0.15\,\lambda$ excited by a plane wave traveling in the -z direction. 21

3.1 Arbitrarily-shaped conducting body excited by an incident electromagnetic plane wave. 23

3.2 Basis function description. 25

3.3 Testing path associated with the m^{th} edge. 26

3.4 Electric charge patch around the i^{th} node. 28

3.5 Electric source patches S_{n1} and S_{n2} for Φ_{mn} calculation. 31

3.6 Bistatic RCS of a sphere of diameter $0.15\ \lambda$ excited by a plane wave traveling in the -z direction. 32

3.7 Bistatic RCS of a cube of length 0.15 λ excited by a plane wave traveling in the -z direction. 32

4.1 An arbitrarily-shaped dielectric body with surface S excited by an external source. 36

4.2 Basis functions $\boldsymbol{f}_n$ and $\boldsymbol{g}_n$ associated with the n^{th} edge. 41

4.3 Testing functions $\boldsymbol{t}_m$ and $\boldsymbol{\ell}_m$ associated with the m^{th} edge. 41

4.4 Observation points for mn^{th} vector (o) and scalar (x) potentials. 45

4.5 Normal electric current components for Φ calculation. 47

4.6 Magnetic charge source area for Ψ calculation. 49

4.7 Magnetic source patches S_{n1} and S_{n2} for Ψ_{mn} calculation. 50

4.8 Orientation of dielectric sphere and cube to the incident plane wave. Sphere radius = 0.1 λ; $\epsilon_R = 4$. Cube length = 0.2 λ; $\epsilon_R = 4$. 52

4.9 Orientation of dielectric cone to the incident plane wave. Cone radius = 0.1 λ; apex half-angle = 30 °; $\epsilon_R = 3$. 52

4.10 Bistatic RCS for a dielectric sphere at $\phi = 0\,°$, radius = 0.1 λ, $\epsilon_R = 4$. . . . 53

4.11 Bistatic RCS for a dielectric sphere at $\phi = 90\,°$, radius = 0.1 λ, $\epsilon_R = 4$. . . 53

4.12 Bistatic RCS for a dielectric cube at $\phi = 0\,°$, length = 0.2 λ, $\epsilon_R = 4$. 54

4.13 Bistatic RCS for a dielectric cube at $\phi = 90\,°$, length = 0.2 λ, $\epsilon_R = 4$. . . . 54

4.14 Bistatic RCS for a dielectric cone at $\phi = 0\,°$, radius = 0.1 λ, apex half-angle = 30 °, $\epsilon_R = 3$, incident wave traveling toward apex. 55

4.15 Bistatic RCS for a dielectric cone at $\phi = 90\,°$, radius = 0.1 λ, apex half-angle = 30 °, $\epsilon_R = 3$, incident wave traveling toward apex. 55

5.1 Arbitrarily-shaped PEC and dielectric bodies with surfaces C, *D1*, and *D2* excited by an external source. 59

5.2 Basis functions $\boldsymbol{f}_n$ and $\boldsymbol{g}_n$ associated with the n^{th} edge. 63

5.3 Testing functions $\boldsymbol{t}_m$ and $\boldsymbol{\ell}_m$ associated with the m^{th} edge. 64

5.4 Observation points for mn^{th} vector (o) and scalar (x) potentials. 68

5.5 Normal electric current components for Φ calculation. 70

5.6 Magnetic charge source area for Ψ calculation. 71

5.7 Magnetic source patches S_{n1} and S_{n2} for Ψ_{mn} calculation. 73

5.8 Geometries for which bistatic RCS was calculated, including a) two spheres, b) a disk/cone, and c) a missile. 75

5.9 Bistatic RCS for two nontouching spheres, one dielectric, $\epsilon_R = 4$, and one PEC. 76

5.10 Bistatic RCS for a composite disk/cone, cone $\epsilon_R = 2$, PEC disk. 76

5.11 Bistatic RCS for a composite missile, nose cone $\epsilon_R = 7.5$, PEC cylinder, incident wave approaching the nose of the missile. 77

5.12 Bistatic RCS for a composite missile, nose cone $\epsilon_R = 7.5$, PEC cylinder, incident wave approaching the tail of the missile. 77

5.13 Dielectric cube of length $0.1\,\lambda$ capped with PEC plates, $\epsilon_R = 4$. 78

5.14 Bistatic RCS at $\phi = 0°$ for a dielectric cube of length $0.1\,\lambda$ capped with PEC plates, $\epsilon_R = 4$. 79

5.15 Bistatic RCS at $\phi = 90°$ for a dielectric cube of length $0.1\,\lambda$ capped with PEC plates, $\epsilon_R = 4$. 79

B.1 Bistatic RCS for a PEC sphere, diameter = 0.18 λ. 91

B.2 Bistatic RCS for a PEC sphere, diameter = 0.18 λ. 92

List of Tables

5.1 Integral Equation Surfaces 60

Chapter 1

Introduction

1.1 Overview

In this work we present a new method for calculating the electromagnetic scattering from arbitrarily shaped, three-dimensional objects in the resonant size [1] range up to a few wavelengths; the objects may be electrical conductors, dielectrics, or a composite of materials having different conducting properties. The novelty of the method lies in the application of new basis functions specially designed for electromagnetic field problems. Two spatially orthogonal, unit pulse basis vectors are defined in conjunction with flat, triangular patches on the scattering surfaces. The pulse basis functions represent the unknown electric and magnetic equivalent surface currents [2] that will be determined by application of the method of moments (MoM) [3]. The geometric properties of the new basis functions allow unique and accurate solutions to be obtained for any geometry/material configuration using any standard combined field formulation such as Combined Field Integral Equation (CFIE) [4], Poggio-Miller-Chang-Harrington-Wu-Tsai (PMCHWT) [5], [6], or the Müller [7] formulation.

1.2 Background

1.2.1 Scattering Solutions

How can we calculate the radiation from the surface of an object that has been electrified, either by the attachment of a current-carrying wire, or by irradiation from an exterior or interior source? If the scatterer's surface geometry conforms to the coordinate surfaces in one of eleven known orthogonal coordinate systems [8], the Helmholtz equation variables in each coordinate may be separated and solved for analytically to produce an exact scattering

solution. This is the case for the sphere [2], the infinite cylinder, the prolate and oblate spheroids, and a variety of conic sections. However, most scattering objects do not conform to these geometries, and for other shapes, approximations must suffice.

Balanis [9] and Richmond [10] have given informative reviews of calculation techniques for PEC and dielectric scatterers, respectively. For electrically large, smooth objects longer than ten wavelengths, simple analytic solutions are available. The ray-optics, or geometric optics (GO) method, for example, has been used for dielectric cylinders and spheres [11]. Biggs [12] applied GO to calculate the RCS for a PEC prolate spheroid. According to Richmond, this method "often provides reasonably accurate results for slightly curved dielectric shells but is inaccurate for rapidly curving shells and the edge region of a truncated shell." The geometric theory of diffraction (GTD), originated by Keller [13], and the physical theory of diffraction (PTD), originated by Ufimtsev [14], are two further refinements that incorporate edge diffraction into the ray-optics solutions. Molinet [15] observes that ray tracing methods have been greatly improved for more complex geometries, and eventually accurate results can be found for scatterers of about one wavelength if special attention and methods are applied to all discontinuities such as corners, vertices, edges, and curve discontinuities.

For scattering problems with no exact solution, perturbation theory and variational methods are two mathematical approximation methods [2]. Perturbation methods start from a geometrically similar problem that does have an exact solution and calculate the change in the solution; Eftimiu [16], [17] used this method to compute scattering from corrugated PEC cylinders. Variational methods approximate the desired quantities themselves; Cohen [18] employed a variational approach for a circular dielectric cylinder. However, Richmond states that this approach becomes complicated and lengthy for dielectric bodies of arbitrary shape.

For layered dielectric bodies of revolution (BOR's) of up to a few wavelengths, iterative methods have been used. In the 1950's, Rhodes [19] and Andreasen [20] calculated the scattering from thin dielectric shells. Govind, Wilton, and Glisson [21] later modeled

inhomogeneous missile plumes by dividing the plumes into piecewise homogeneous layers. Their method was an extension of Mei's unimoment method for BOR's [22].

For arbitrary geometries in the resonant size range, numerical methods provide a practical means of obtaining a very good approximation for scattering. Numerical methods may be classified into integral equation (IE) and differential equation (DE) methods. Using integral equation methods such as MoM, we solve first for equivalent currents and second for the scattered fields resulting from those currents. In contrast, using differential equation methods such as finite element analysis and the finite difference time domain method, we solve directly for the scattered fields. In our opinion, integral equations provide the most accurate solutions because they incorporate Green's functions that enforce the radiation condition: the scattered fields diminish to zero at infinite distance. If the scattering object contains regions of homogeneous permittivity ϵ and permeability μ, it is sufficient to write boundary equations to express the continuity of the tangential electric and magnetic fields across the region boundaries. Our work is based on such a technique, the MoM surface integral equation technique.

1.2.2 Method of Moments

Harrington [23] has written a history of the development of MoM, beginning with Galerkin's work with linear matrix equations circa 1915. In his development, Harrington wove Galerkin's method together with Rumsey's reaction concept [24] and the Rayleigh-Ritz variational method; in a departure from Galerkin's method, he decided that weighting and testing functions could be made different from each other in order to facilitate the speed of calculation. Harrington chose the name "method of moments" to describe his method because it most closely followed the work of Kantorovich and Akilov [25], who used that name. Some of the earliest MoM solutions were published in 1963 by Mei and Van Bladel [26], who calculated scattering from PEC rectangular cylinders. Richmond [10] in 1965 calculated the fields from a thin dielectric cylinder of arbitrary shape after first using surface integrals and MoM to find the polarization currents. In 1968, Harrington [3]

popularized MoM with his text book, *Field Computation by Moment Methods*. Since then, continuous increases in digital computer processing speed and memory size have served to make numerical methods commonplace tools for electromagnetic analysis and design. Due to their faster computational speed, surface MoM techniques have remained more popular than volume integral MoM techniques for solving three-dimensional problems.

Chang and Harrington used fictitious equivalent electric and magnetic surface currents, a concept described by Schelkunoff [27], to calculate the characteristic modes for two-dimensional dielectric bodies. We will use the electric field integral equation (EFIE) and magnetic field integral equation (HFIE) in the form given in their 1977 paper [5] to calculate the scattered fields from arbitrarily-shaped, three-dimensional dielectric scatterers. For each region of interest:

$$EFIE: \left[j\,\omega \boldsymbol{A} + \nabla \Phi + \frac{1}{\varepsilon} \nabla \times \boldsymbol{F} \right]_{tan} = \left[\boldsymbol{E}^{\,i} \right]_{tan} \tag{1.1}$$

$$HFIE: \left[j\,\omega \boldsymbol{F} + \nabla \Psi - \frac{1}{\mu} \nabla \times \boldsymbol{A} \right]_{tan} = \left[\boldsymbol{H}^{\,i} \right]_{tan} \tag{1.2}$$

where the magnetic and electric vector potentials, $\boldsymbol{A}$ and $\boldsymbol{F}$, respectively, are defined in terms of the equivalent electric and magnetic surface currents $\boldsymbol{J}_S$ and $\boldsymbol{M}_S$ as

$$\boldsymbol{A} = \mu \iint_S \boldsymbol{J}_S \; G \; dS' \tag{1.3}$$

$$\boldsymbol{F} = \epsilon \iint_S \boldsymbol{M}_S \; G \; dS' \,, \tag{1.4}$$

the electric scalar potential Φ is defined as

$$\Phi = \frac{1}{\epsilon} \iint_S q_S^e \; G \; dS' \tag{1.5}$$

$$= \frac{j}{\omega \epsilon} \iint_S \nabla \bullet \boldsymbol{J}_S \; G \; dS' \,, \tag{1.6}$$

the magnetic scalar potential Ψ is defined as

$$\Psi = \frac{1}{\mu} \iint_S q_S^m \, G \, dS' \tag{1.7}$$

$$= \frac{j}{\omega\mu} \iint_S \nabla \bullet \boldsymbol{M}_S \, G \, dS' \,, \tag{1.8}$$

q_S^e is the electric surface charge density related to the electric current density by the equation

$$\nabla \bullet \boldsymbol{J}_S = -j\omega \, q_S^e \,, \tag{1.9}$$

q_S^m is the magnetic surface charge density related to the magnetic current density by the equation

$$\nabla \bullet \boldsymbol{M}_S = -j\omega \, q_S^m \,, \tag{1.10}$$

the Green's function G is defined as

$$G = \frac{e^{-jkR}}{4\pi R} \tag{1.11}$$

$$R = |\boldsymbol{r} - \boldsymbol{r}'| \,, \tag{1.12}$$

μ and ϵ are the permeability and permittivity constants of the surrounding medium, S' denotes the source surface, and k is the wave number. The vectors $\boldsymbol{r}$ and $\boldsymbol{r}'$ are position vectors to observation and source points, respectively, from a global coordinate origin. The left sides of (1.1) and (1.2) represent tangential reflected fields, while the right sides represent tangential incident fields. The derivation of (1.1) and (1.2) is given in Appendix A.

How can the surface integral method equate the incident and scattered fields at the surface of a dielectric body? Chang and Harrington write separate equations for the inner and outer sides of the surface. The total solution is viewed as the superposition of two cases; in the first case, the inner region has zero field and in the second case, the outer region has zero field. When both cases are added together, the tangential fields have a nonzero sum in both inner and outer regions. The equivalent surface currents $\boldsymbol{J}_S$ and $\boldsymbol{M}_S$ are expressions

of the actual fields $\hat{\boldsymbol{n}} \times \boldsymbol{H}_{tan}$ and $\boldsymbol{E}_{tan} \times \hat{\boldsymbol{n}}$, rather than actual currents, where $\hat{\boldsymbol{n}}$ is a unit vector normal to the surface and pointing into the region of scattering. It is assumed that the outer and inner equivalent surface currents have opposite direction, and therefore, sum to zero.

1.3 Statement of the Problem

Maue's integral equation [29] is commonly employed to expand the portions of (1.1) and (1.2) containing $\frac{1}{\varepsilon}\nabla \times \boldsymbol{F}$ and $\frac{1}{\mu}\nabla \times \boldsymbol{A}$. Most often, this equation is seen in the form:

$$\begin{aligned} \boldsymbol{H}^s(\boldsymbol{J}) &= -\frac{1}{\mu}\nabla \times \boldsymbol{A} = -\nabla \times \iint_S \boldsymbol{J}_S \, G \, dS' \\ &= -\hat{\boldsymbol{n}} \times \frac{\boldsymbol{J}_S}{2} - \iint\!\!\!\!\!\!-_S \nabla G \times \boldsymbol{J}_S \, dS' \end{aligned} \tag{1.13}$$

where the deleted integral symbol $\iint\!\!\!\!\!\!-$ indicates the principal value. By duality [2],

$$\begin{aligned} \boldsymbol{E}^s(\boldsymbol{M}) &= \frac{1}{\varepsilon}\nabla \times \boldsymbol{F} = \nabla \times \iint_S \boldsymbol{M}_S \, G \, dS' \\ &= \hat{\boldsymbol{n}} \times \frac{\boldsymbol{M}_S}{2} + \iint\!\!\!\!\!\!-_S \nabla G \times \boldsymbol{M}_S \, dS' \, . \end{aligned} \tag{1.14}$$

In MoM scattering solutions, (1.13) and (1.14) are usually treated with Rao-Wilton-Glisson (RWG) [28] basis functions together with triangular patch modeling. In the RWG method, the testing functions are the same as the basis functions. It may be noted that the RWG basis functions were originally defined for PEC MoM problems. The application of these basis functions for dielectric/composite body problems is not entirely satisfactory for the following reason.

When (1.13) and (1.14) are expanded and tested, unstable and incorrect solutions can occur if the basis and testing functions are not carefully chosen. For example, if we call the testing vectors $\boldsymbol{t}$ and $\boldsymbol{\ell}$, the expressions $\boldsymbol{\ell} \bullet (-\hat{\boldsymbol{n}} \times \frac{\boldsymbol{J}_S}{2})$ or $\boldsymbol{t} \bullet (\hat{\boldsymbol{n}} \times \frac{\boldsymbol{M}_S}{2})$ will tend to be insignificantly small if, in either expression, the testing vector and the current basis vector are parallel. Unfortunately, use of the RWG basis functions for both currents $\boldsymbol{J}_S$

and $\boldsymbol{M}_S$ tends to create this scenario. In the MoM matrix equation, the terms $-\hat{\boldsymbol{n}} \times \frac{\boldsymbol{J}_S}{2}$ and $\hat{\boldsymbol{n}} \times \frac{\boldsymbol{M}_S}{2}$ are moment matrix self terms, which lie on the diagonal and should be dominant. We implement basis and testing functions that will preserve these self term portions as well as the principal values of the curl terms in (1.1) and (1.2).

At certain frequencies, known as characteristic frequencies, false or spurious mathematical solutions exist for the EFIE and HFIE for a closed body, whether the body is made of PEC, dielectric or composite material. Yaghjian [30] has discussed this problem thoroughly. In order to eliminate these spurious solutions, a number of combined field methods have been devised, such as CFIE, PMCHWT, and Müller. Each of these methods combines the EFIE and HFIE in a particular way that obtains correct solutions at all frequencies including the characteristic frequencies. The paired pulse basis functions presented in this work allow the implementation of any of these formulations accurately and efficiently. Use of the basis and testing functions presented here represents a relatively straightforward approach and a simpler composite solution, when compared to the methods proposed by Sheng, Jin, Song et al. [31] or Kishk and Shafai [32].

1.4 The Proposed Method

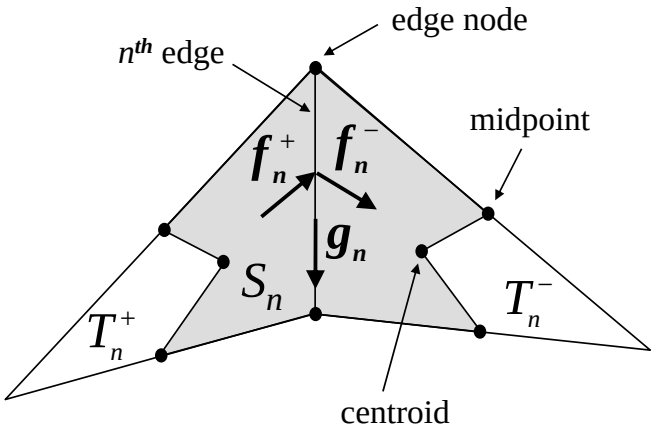

Figure 1.1: Basis functions $\boldsymbol{f}_n$ and $\boldsymbol{g}_n$ associated with the n^{th} edge.

At the outset, we assume a triangular patch model for the given object. Within the triangular surface mesh, T_n^+ and T_n^- represent two triangles connected to the n^{th} edge as shown in Fig. 1.1. The edges of each triangle other than the n^{th} edge we will call *free* edges. Within each triangle, the surface is planar. We define two mutually orthogonal vector basis functions associated with the n^{th} edge as

$$\boldsymbol{f}_n(\boldsymbol{r}) = \begin{cases} \hat{\boldsymbol{n}}^{\pm} \times \boldsymbol{g}_n, & \boldsymbol{r} \in S_n\,, \\ 0, & \text{otherwise} \end{cases} \tag{1.15}$$

and

$$\boldsymbol{g}_n(\boldsymbol{r}) = \begin{cases} \text{unit vector} \parallel n^{th} \text{ edge}, & \boldsymbol{r} \in S_n\,, \\ 0, & \text{otherwise} \end{cases} \tag{1.16}$$

where $\hat{\boldsymbol{n}}^{\pm}$ represents the unit vector normal to the plane of the triangle $T_n^{\pm}$. The domain of the basis functions is S_n, the region whose perimeter is drawn by connecting the mid-points of the free edges to the centroids of triangles $T_n^{\pm}$ and to the nodes of edge n. Shown as a shaded area in Fig. 1.1, S_n is 2/3 of the total triangular patch area. The basis functions defined in (1.15) and (1.16) are unit pulse functions that are orthogonal to each other. In dielectric scattering problem solutions, we will use $\boldsymbol{f}_n$ to expand $\boldsymbol{J}_S$ and $\boldsymbol{g}_n$ to expand $\boldsymbol{M}_S$ in the integral equations.

We further define the testing functions associated with edge m as vectors $\boldsymbol{t}_m^{\pm}$ and $\boldsymbol{\ell}_m$, as shown in Fig. 1.2. Vector $\boldsymbol{t}_m^+$ extends from the triangle T_m^+ centroid to the edge m midpoint; $\boldsymbol{t}_m^-$ extends from the edge m midpoint to the triangle T_m^- centroid. Vector $\boldsymbol{\ell}_m$ extends from the beginning to the end of edge m, in the direction of $\boldsymbol{g}_m$. The testing vector $\boldsymbol{t}$ is used in conjunction with the EFIE, while the testing vector $\boldsymbol{\ell}$ is used in conjunction with the HFIE to solve dielectric problems. Testing the expanded integral equations then results in the nonzero products $\boldsymbol{t} \bullet \boldsymbol{f}$, $\boldsymbol{t} \bullet (\hat{\boldsymbol{n}} \times \frac{\boldsymbol{g}}{2})$, $\boldsymbol{\ell} \bullet \boldsymbol{g}$, and $\boldsymbol{\ell} \bullet (-\hat{\boldsymbol{n}} \times \frac{\boldsymbol{f}}{2})$. With this arrangement, all of the currents are well-tested.

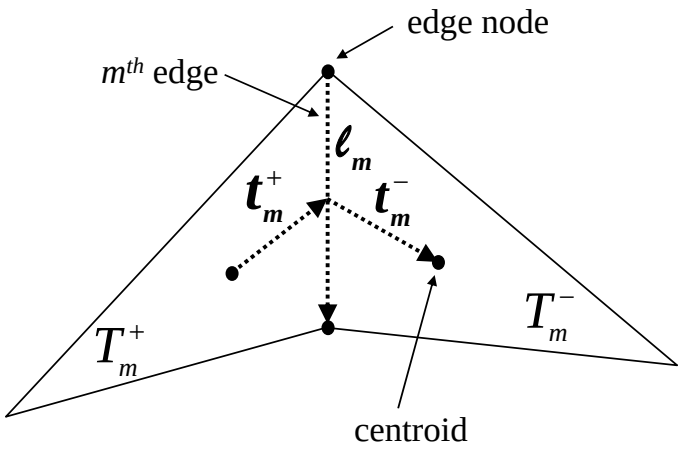

Figure 1.2: Testing functions $\boldsymbol{t}_m$ and $\boldsymbol{\ell}_m$ associated with the m^{th} edge.

1.5 Scope

The example problems we address are frequency domain problems concerning scattering bodies that may be decomposed into homogeneous regions having real or complex ϵ. While the accuracy of a given solution may be somewhat affected by the meshing and integral evaluation techniques chosen, such questions are not the focus of the paper and are not dwelt upon. The triangular meshes have been drawn fine enough to produce solutions that appear to the eye to be reasonably well converged when plotted. Meshes in the example problems follow the rule of thumb of at least 300 unknowns per square wavelength of scattering surface area. Also, the meshes have been drawn somewhat irregularly to avoid a particular type of model-induced error called *grid* error. The intent of the dissertation is to make a mathematical argument for the pulse basis pair method and to demonstrate correct scattering solutions for a number of mostly canonical geometries that can be solved by another trusted method for comparison. Numerical integrations have been performed using the Gaussian quadrature method for triangles.

1.6 Organization

The body of this document contains four chapters that were initially written to be published as individual journal articles. They have been reformatted and slightly expanded for inclusion here. Each chapter is self-contained and may contain some repetition of previous text. Chapter 2 discusses the $\boldsymbol{f}$ basis function for equivalent electric surface currents in PEC bodies. Chapter 3 discusses the $\boldsymbol{g}$ basis function, also for equivalent electric surface currents in PEC bodies. While either basis function may be employed for EFIE or HFIE solutions for PEC bodies, chapters 2 and 3 present EFIE solutions only. Chapter 4 describes the use of the $\boldsymbol{f}$ and $\boldsymbol{g}$ basis functions for equivalent electric and magnetic surface currents, respectively, in dielectric bodies. In chapter 4, EFIE and HFIE solutions are compared for the same problems; the two solutions can be combined in the appropriate manner to obtain any of the combined field formulations. In chapter 5, the use of $\boldsymbol{f}$ and $\boldsymbol{g}$ basis functions is described for the solution of composite scattering bodies. For those examples, EFIE solutions are shown for composites modeled as combinations of open and closed bodies, and an HFIE solution is shown for a composite modeled as a combination of two closed bodies.

A derivation of the dielectric integral equations may be found in Appendix A. Appendix B contains an example of the flexibility of the pulse vector basis functions; a PEC sphere scattering problem is solved four times consecutively by using either $\boldsymbol{f}$ or $\boldsymbol{g}$ basis functions for the EFIE or HFIE method.

Chapter 2

New Basis Functions for the Electromagnetic Solution of Arbitrarily-shaped, Three-dimensional Conducting Bodies Using Method of Moments

2.1 Overview

In this chapter, we present a new set of basis functions, defined over a pair of planar triangular patches, for the solution of electromagnetic scattering and radiation problems associated with arbitrarily-shaped surfaces using the method of moments solution procedure. The basis functions are constant over the function subdomain and resemble pulse functions for one- and two-dimensional problems. Further, another set of basis functions, orthogonal to the first set, is also defined over the same physical space. The primary objective of developing these basis functions is to utilize them for electromagnetic solutions involving conducting, dielectric, and composite bodies. The present chapter, however, involves only conducting bodies along with several numerical results.

2.2 Introduction

The solution of electromagnetic scattering/radiation problems involving arbitrary shapes and material composition is of much interest to commercial as well as defense industries. The method of moments (MoM) [2] solutions to these problems generally involve triangular patch modeling, utilizing Rao-Wilton-Glisson (RWG) [28] basis functions. It may be noted that the RWG basis functions have been defined for the solution of conducting bodies and the utilization of the same basis functions for dielectric/composite bodies is less than satisfactory. The primary difficulty associated with a material body solution is the requirement of two orthogonal basis functions to express unknown electric and magnetic surface currents

$\boldsymbol{J}_S$ and $\boldsymbol{M}_S$. In our opinion, using the same basis functions for both $\boldsymbol{J}_S$ and $\boldsymbol{M}_S$ is not a good idea and invariably results in numerical difficulties. Consequently, a host of techniques has been developed which involve either tinkering with the basis functions or modifying the testing procedures to apply for material bodies [31, 33, 34]. Keeping these difficulties in perspective, in this work, we present two orthogonal sets of basis functions that can be used for conducting as well as material bodies. The solution of the material body problem will be presented in due course.

2.3 Description of the Problem

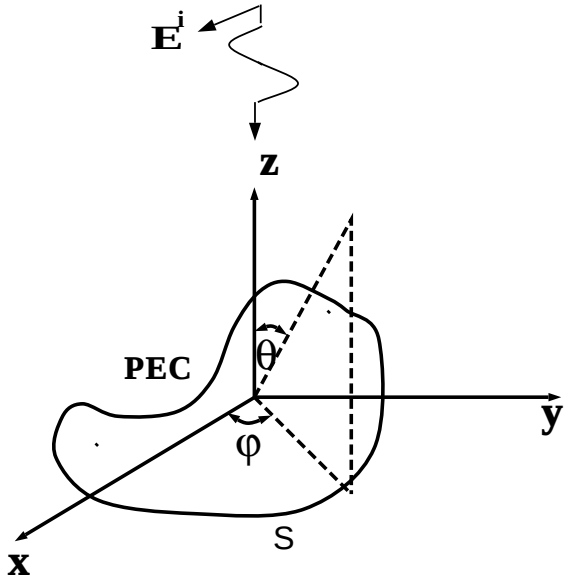

Figure 2.1: Arbitrarily-shaped conducting body excited by an incident electromagnetic plane wave.

Let S denote the surface of an arbitrarily-shaped perfectly conducting body illuminated by an incident electromagnetic plane wave $\boldsymbol{E}^i$ as shown in Fig. 2.1. We assume S to be open or closed and orientable, possessing a piecewise continuous normal. S may be composed of intersecting surfaces. Using the equivalence principle, potential theory, and the free-space

Green's function [2], the electric field integral equation (EFIE) is given by

$$[j\omega \boldsymbol{A} + \nabla \Phi]_{tan} \quad = \quad \boldsymbol{E}^i_{tan} \tag{2.1}$$

where the subscript *tan* refers to the tangential component. In (2.1),

$$\boldsymbol{A} \quad = \quad \mu \iint_S \boldsymbol{J}_s \, G \, dS' \tag{2.2}$$

$$\Phi \quad = \quad \epsilon^{-1} \iint_S q_s \, G \, dS' \tag{2.3}$$

$$G \quad = \quad \frac{e^{-jkR}}{4\pi R} \tag{2.4}$$

$$R \quad = \quad |\boldsymbol{r} - \boldsymbol{r}'| \, , \tag{2.5}$$

ϵ and μ are the permittivity and permeability constants of the surrounding medium, k is the wave number, and $\boldsymbol{r}$ and $\boldsymbol{r}'$ represent the position vectors to observation and source points, respectively, from a global coordinate origin. The unknown surface current density $\boldsymbol{J}_s$ is related to the charge density q_s by the continuity equation, given by

$$\nabla \bullet \boldsymbol{J}_s \quad = \quad -j\omega \, q_s \, . \tag{2.6}$$

For the numerical solution of (2.1), we apply the method of moments formulation using planar triangular patch modeling and the basis functions as described in the following section:

2.4 Description of Basis Functions

Let T_n^+ and T_n^- represent two triangles connected to the edge n of the triangulated surface model as shown in Fig. 2.2. We define two mutually orthogonal vector basis

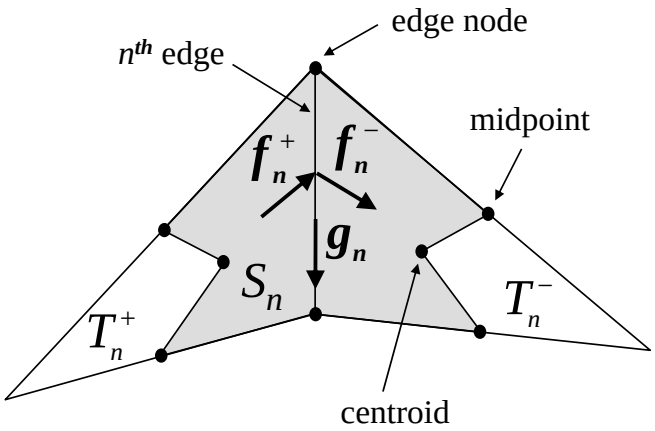

Figure 2.2: Basis function description.

functions associated with the n^{th} edge as

$$\boldsymbol{f}_n(\boldsymbol{r}) = \begin{cases} \hat{\boldsymbol{n}}^{\pm} \times \hat{\boldsymbol{\ell}}, & \boldsymbol{r} \in S_n\,, \\ 0, & \text{otherwise} \end{cases} \tag{2.7}$$

and

$$\boldsymbol{g}_n(\boldsymbol{r}) = \begin{cases} \hat{\boldsymbol{\ell}}, & \boldsymbol{r} \in S_n\,, \\ 0, & \text{otherwise} \end{cases} \tag{2.8}$$

where S_n represents the region obtained by connecting the mid-points of the free edges to the centroids of triangles $T_n^{\pm}$, and to the nodes of edge n. This is shown shaded in Fig. 2.2. Also, $\hat{\boldsymbol{\ell}}$ and $\hat{\boldsymbol{n}}^{\pm}$ represent the unit vector along the n^{th} edge and the unit vector normal to the plane of the triangle $T_n^{\pm}$, respectively. Note that the basis functions defined in (2.7) and (2.8) are actually the pulse functions defined over the region S_n. It is well-known that the pulse functions do not have continuous derivatives but result in delta distributions along the boundary. This point is crucial in modeling the charge density and the calculation of scalar potential, which may be accomplished as described in the following section. Also, note that in this chapter, only perfect electric conductor (PEC) bodies are analyzed and hence only $\boldsymbol{f}_n$'s are used in the method of moments solution.

2.5 Numerical Solution Procedure

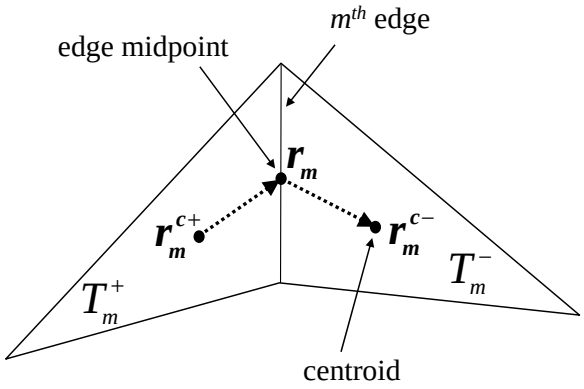

Figure 2.3: Testing paths associated with the m^{th} edge.

As a first step, we consider the testing procedure. Consider the m^{th} interior edge, associated with triangles $T_m^{\pm}$, as shown in Fig. 2.3. We integrate the vector component of (2.1) parallel to the path from the centroid $\boldsymbol{r}_m^{c+}$ of T_m^+ to the midpoint of the edge $\boldsymbol{r}_m$ and thence from $\boldsymbol{r}_m$ to the centroid of T_m^- given by $\boldsymbol{r}_m^{c-}$. For each section of the path integration, we approximate $\boldsymbol{A}$ and $\boldsymbol{E}^i$ by their respective values at the mid-points of the path. Thus, we have,

$$\begin{aligned} j\omega \boldsymbol{A}\left(\frac{\boldsymbol{r}_m+\boldsymbol{r}_m^{c+}}{2}\right)\bullet(\boldsymbol{r}_m-\boldsymbol{r}_m^{c+})+j\omega \boldsymbol{A}\left(\frac{\boldsymbol{r}_m+\boldsymbol{r}_m^{c-}}{2}\right)\bullet(\boldsymbol{r}_m^{c-}-\boldsymbol{r}_m)+ \\ \left[\Phi(\boldsymbol{r}_m^{c-})-\Phi(\boldsymbol{r}_m^{c+})\right]=\boldsymbol{E}^i\left(\frac{\boldsymbol{r}_m+\boldsymbol{r}_m^{c+}}{2}\right)\bullet(\boldsymbol{r}_m-\boldsymbol{r}_m^{c+})+ \\ \boldsymbol{E}^i\left(\frac{\boldsymbol{r}_m+\boldsymbol{r}_m^{c-}}{2}\right)\bullet(\boldsymbol{r}_m^{c-}-\boldsymbol{r}_m) \end{aligned} \tag{2.9}$$

for $m=1,2,3,\cdots,N$, where N represents the total number of interior edges in the triangulation scheme, *i.e.*, excluding the edges on the boundary for an open body.

Next, we consider the expansion procedure. Using the basis functions $\boldsymbol{f}_n$ defined in (2.7), we approximate the unknown current $\boldsymbol{J}_S$ as

$$\boldsymbol{J}_S \;=\; \sum_{n=1}^{N} I_n \boldsymbol{f}_n \,. \tag{2.10}$$

Next, substituting the current expansion (2.10) into (2.9) yields an $N \times N$ system of linear equations which may be written in matrix form as $\boldsymbol{ZI} = \boldsymbol{V}$, where $\boldsymbol{Z} = [Z_{mn}]$ is an $N \times N$ matrix and $\boldsymbol{I} = [I_n]$ and $\boldsymbol{V} = [V_m]$ are column vectors of length N. The elements of $\boldsymbol{Z}$ and $\boldsymbol{V}$ are given by

$$Z_{mn} = j\omega \left[\boldsymbol{A}^{+}_{mn} \bullet (\boldsymbol{r}_m - \boldsymbol{r}^{c+}_m) + \boldsymbol{A}^{-}_{mn} \bullet (\boldsymbol{r}^{c-}_m - \boldsymbol{r}_m) \right] + \Phi^{-}_{mn} - \Phi^{+}_{mn} \tag{2.11}$$

$$V_m = \boldsymbol{E}^{+}_m \bullet (\boldsymbol{r}_m - \boldsymbol{r}^{c+}_m) + \boldsymbol{E}^{-}_m \bullet (\boldsymbol{r}^{c-}_m - \boldsymbol{r}_m) \tag{2.12}$$

where

$$\boldsymbol{A}^{\pm}_{mn} = \mu \iint_S \boldsymbol{f}_n \, \frac{e^{-jkR^{\pm}_m}}{4\pi R^{\pm}_m} \, dS' \tag{2.13}$$

$$\Phi^{\pm}_{mn} = \frac{-1}{j\omega\epsilon} \iint_S \nabla_s \bullet \boldsymbol{f}_n \, \frac{e^{-jkR^{c\pm}_m}}{4\pi R^{c\pm}_m} \, dS' \tag{2.14}$$

$$R^{\pm}_m = \left| \frac{\boldsymbol{r}_m + \boldsymbol{r}^{c\pm}_m}{2} - \boldsymbol{r}' \right| \tag{2.15}$$

$$R^{c\pm}_m = |\boldsymbol{r}^{c\pm}_m - \boldsymbol{r}'| \tag{2.16}$$

$$\boldsymbol{E}^{\pm}_m = \boldsymbol{E}^{i} \left(\frac{\boldsymbol{r}_m + \boldsymbol{r}^{c\pm}_m}{2} \right) . \tag{2.17}$$

The numerical evaluation of the vector potential, shown in (2.13), is straightforward and may be accomplished by the procedure described in [35]. However, the numerical evaluation of the scalar potential term, described in (2.14), may be carried out as follows:

Let us define the unknown charge density q_S in (2.3) as

$$q_S = \sum_{i=1}^{N_p} \alpha_i P_i \tag{2.18}$$

where N_P represents the number of triangular patches in the model, α_i is the unknown coefficient, and

$$P_i(\boldsymbol{r}) = \begin{cases} 1, & \boldsymbol{r} \in T_i \, , \\ 0, & \text{otherwise} \, . \end{cases} \tag{2.19}$$

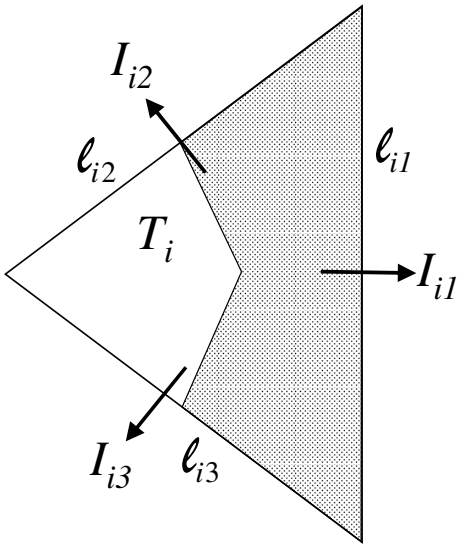

Figure 2.4: Electric charge patch within the T_i^{th} triangle.

Next, consider a triangular patch T_i with associated non-boundary edges, i_1, i_2, and i_3. Then, using (2.6), the well-known divergence theorem, and simple vector calculus, we have

$$\begin{aligned} \iint_{T_i} q_S dS &= \iint_{T_i} \frac{\nabla_S \bullet \boldsymbol{J}_S}{-j\omega}\, dS \\ &= \frac{j}{\omega} \oint_{C_i} \boldsymbol{J}_S \bullet \hat{\boldsymbol{n}}_\ell \\ &= \frac{j}{\omega}[I_{i_1}\ell_{i_1} + I_{i_2}\ell_{i_2} + I_{i_3}\ell_{i_3}] \end{aligned} \tag{2.20}$$

where C_i is the contour bounding the triangle T_i, $\hat{\boldsymbol{n}}_\ell$ is the unit vector normal to the contour C_i in the plane of T_i, and $\ell_{i_j},\ j = 1, 2, 3$ represent the edge lengths. This scheme is shown in Fig. 2.4. Also, note that

$$\begin{aligned} \iint_{T_i} q_S dS &= \iint_{T_i} \alpha_i dS \\ &= \alpha_i \mathcal{A}_i \end{aligned} \tag{2.21}$$

where $\mathcal{A}_i$ represents the area of the triangle T_i. Lastly, using (2.20) and (2.21), we have

$$\alpha_i = \frac{j}{\omega}\left[\frac{I_{i_1}\ell_{i_1} + I_{i_2}\ell_{i_2} + I_{i_3}\ell_{i_3}}{\mathcal{A}_i}\right]. \tag{2.22}$$

Thus, we can write the scalar potential term in (2.14) as

$$\Phi_{mn}^{\pm} = \frac{j\ell_n}{\omega\epsilon}\left[\frac{1}{\mathcal{A}_{n^+}}\iint_{T_n^+}\frac{e^{-jkR_m^{c\pm}}}{4\pi R_m^{c\pm}}\,dS' + \frac{1}{\mathcal{A}_{n^-}}\iint_{T_n^-}\frac{e^{-jkR_m^{c\pm}}}{4\pi R_m^{c\pm}}\,dS'\right]. \tag{2.23}$$

Finally, once the matrices $\boldsymbol{Z}$ and $\boldsymbol{V}$ are determined, we may easily solve the system of linear equations to obtain $\boldsymbol{I}$.

2.6 Numerical Results

In this section, we present numerical results for a square plate (length = $0.15\,\lambda$), a circular disk (diameter = $0.15\,\lambda$), a sphere (diameter = $0.15\,\lambda$) and a circular cylinder (diameter = $0.15\,\lambda$, length = $0.15\,\lambda$), and compare with the solutions obtained using the procedure presented in [28]. Also, for the case of the sphere, the results are compared with the exact solution. The plate, the disk, the sphere, and the cylinder are modeled with 312, 258, 500, and 320 triangles, respectively. In every case, the body is placed at the center of the coordinate system and illuminated by an x-polarized plane wave traveling in the negative direction along the z-axis. Further, the square plate and the circular disk are oriented parallel to the xy-plane. The bistatic radar cross sections (RCS's) are presented in Figs. 2.5–2.8. We note that the results compare well with the other numerical results.

2.7 Summary

In this chapter, we have presented a new set of basis functions, which we called the $\boldsymbol{f}$ basis functions, for the method of moments solution of electromagnetic scattering by bodies of arbitrary shape. The $\boldsymbol{f}$ basis functions are vectors perpendicular to the mesh edges. Another set of basis functions, orthogonal to the first set, has also been presented; these are

the $\boldsymbol{g}$ basis functions, vectors parallel to the mesh edges. Both of these new basis functions are pulse vectors defined over adjacent pairs of triangular patches. It is hoped that these two sets of basis functions, in conjunction with the method of moments solution procedure, will provide a more stable solution to material problems. However, in the present chapter, only conducting scatterers were analyzed with the new basis function $\boldsymbol{f}$ and the results were compared with those from other solution methods. The new basis functions will be applied to material bodies in chapters 4 and 5.

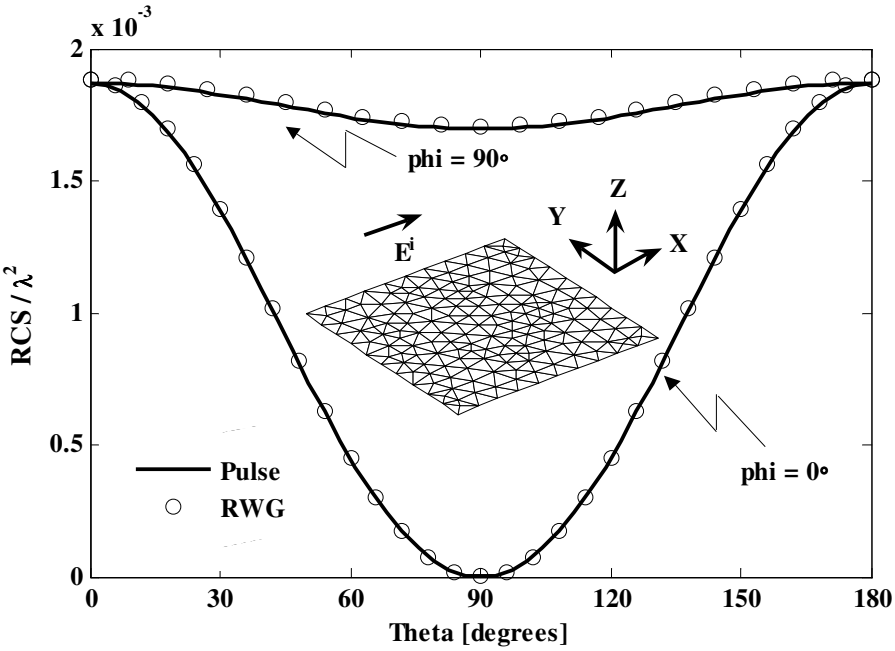

Figure 2.5: Bistatic RCS of a square plate of length $0.15\,\lambda$ excited by a plane wave traveling in the -z direction.

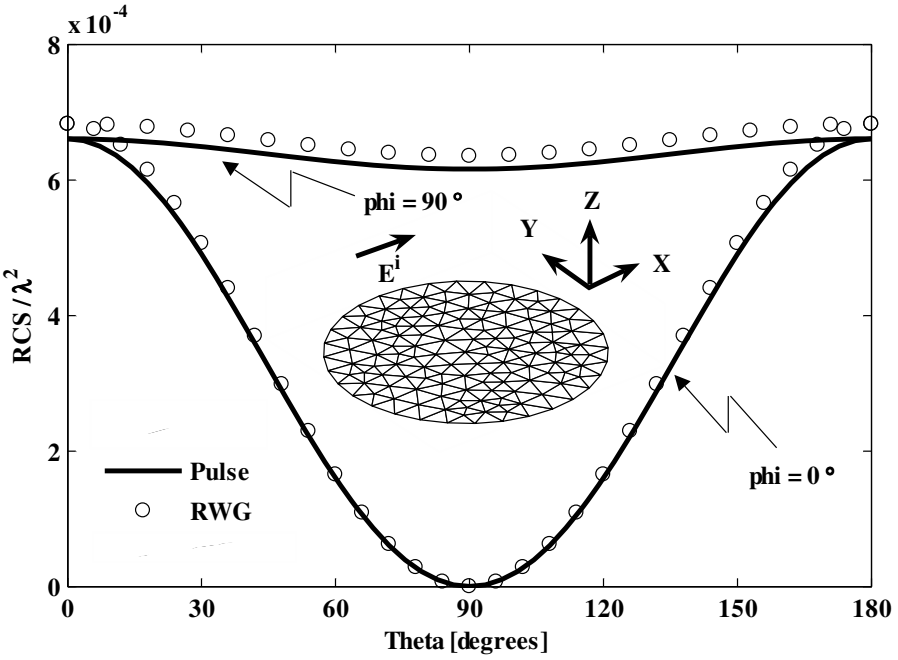

Figure 2.6: Bistatic RCS of a circular disk of diameter $0.15\,\lambda$ excited by a plane wave traveling in the -z direction.

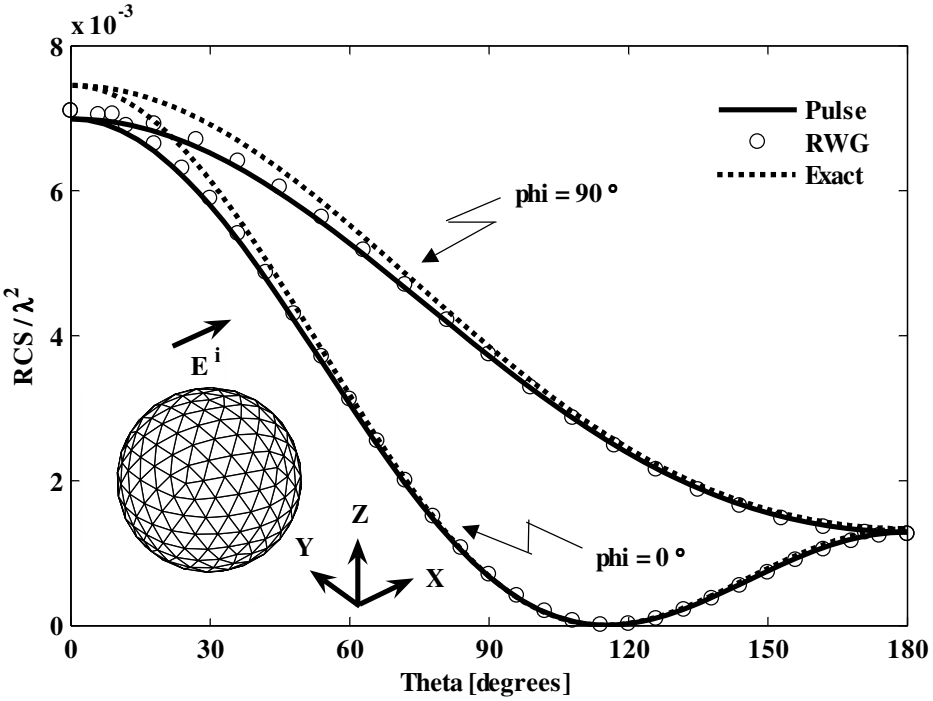

Figure 2.7: Bistatic RCS of a sphere of diameter $0.15\,\lambda$ excited by a plane wave traveling in the -z direction.

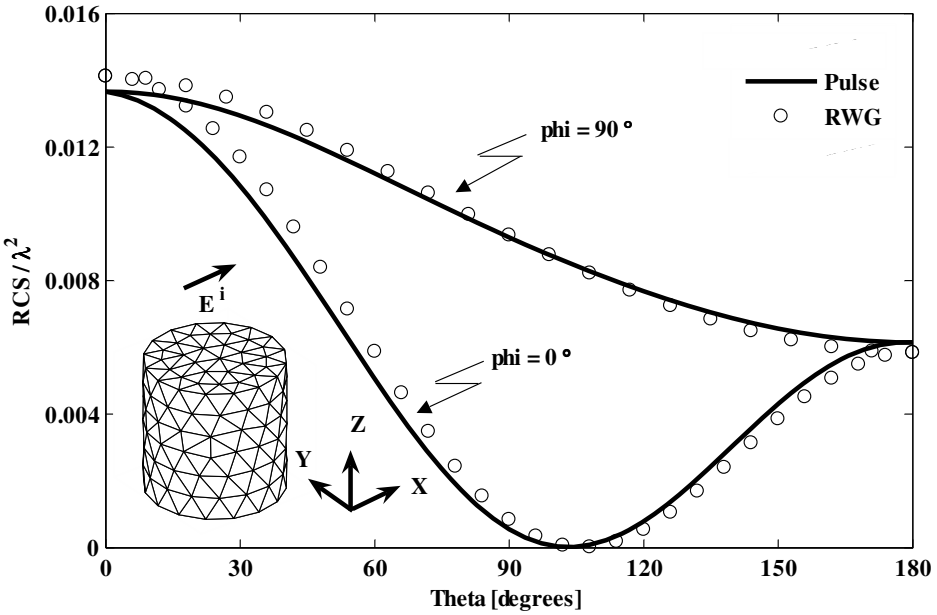

Figure 2.8: Bistatic RCS of a circular cylinder of diameter $0.15\,\lambda$ and height $0.15\,\lambda$ excited by a plane wave traveling in the -z direction.

Chapter 3

An Alternate Set of Basis Functions for the Electromagnetic Solution of Arbitrarily-Shaped, Three-Dimensional, Closed Conducting Bodies Using Method of Moments

3.1 Overview

In chapter 2, we introduced two new sets of pulse-type basis functions, each defined over adjacent pairs of planar triangular patches, to calculate the electromagnetic scattering/radiation associated with three-dimensional, arbitrarily-shaped material bodies. We then explored in detail the suitability of one set of basis functions, the $\boldsymbol{f}$ pulse basis vectors, to calculate electromagnetic scattering from arbitrarily-shaped conducting bodies, either open or closed. In this chapter, we explore the use of an alternate set of basis functions, the $\boldsymbol{g}$ pulse basis vectors, which are orthogonal to the $\boldsymbol{f}$ pulse basis functions previously defined. We describe the numerical solution scheme using $\boldsymbol{g}$ basis vectors and calculate the perfect electric conductor (PEC) scattering for two canonical closed geometries. The pulse basis results are then compared with the results calculated by other means.

3.2 Introduction

The primary motivation for this work is to develop an efficient and well-conditioned method of moments (MoM) [3] solution for dielectric material bodies via a surface integral equation (SIE) approach [36]. It may be noted that since the SIE approach involves both electric and magnetic currents as unknowns in the MoM formulation, it is necessary to define two mutually orthogonal sets of basis functions to generate a well-conditioned moment matrix. We emphasize here that the mathematical equations appearing in the dielectric

body SIE formulation are very similar to the equations we encounter in the PEC body problem; therefore, solving the PEC case provides confidence in the solution methodology.

3.3 Description of the Problem

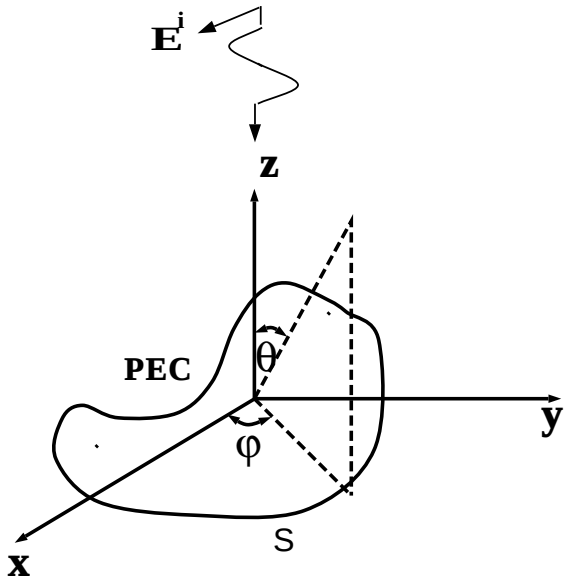

Figure 3.1: Arbitrarily-shaped conducting body excited by an incident electromagnetic plane wave.

Let S denote the surface of an arbitrarily-shaped, perfectly conducting body illuminated by an incident electromagnetic plane wave $\boldsymbol{E}^i$ as shown in Fig. 3.1. We assume S to be closed and orientable, possessing a piecewise continuous normal. S may be composed of intersecting surfaces. Using the equivalence principle, potential theory, and the free-space Green's function [2], the electric field integral equation (EFIE) is given by

$$[j\omega \boldsymbol{A} + \nabla \Phi]_{tan} \quad = \quad \boldsymbol{E}^i_{tan} \tag{3.1}$$

where the subscript *tan* refers to the tangential component. In (3.1),

$$\boldsymbol{A} = \mu \iint_S \boldsymbol{J}_S \, G \, dS' \tag{3.2}$$

$$\Phi = \epsilon^{-1} \iint_S q_S \, G \, dS' \tag{3.3}$$

$$G = \frac{e^{-jkR}}{4\pi R} \tag{3.4}$$

$$R = |\boldsymbol{r} - \boldsymbol{r}'| \,, \tag{3.5}$$

ϵ and μ are the permittivity and permeability constants of the surrounding medium, k is the wave number, and $\boldsymbol{r}$ and $\boldsymbol{r}'$ represent the position vectors to observation and source points, respectively, from a global coordinate origin. The unknown surface current $\boldsymbol{J}_S$ is related to the charge density q_S by the continuity equation, given by

$$\nabla \bullet \boldsymbol{J}_S = -j\omega \, q_S \,. \tag{3.6}$$

For the numerical solution of (3.1), we apply the method of moments formulation using planar triangular patch modeling and the basis functions as described in the following:

3.4 Description of Basis Functions

Let T_n^+ and T_n^- represent two triangles connected to the edge n of the triangulated surface model as shown in Fig. 3.2. We define two mutually orthogonal vector basis functions associated with the n^{th} edge as

$$\boldsymbol{f}_n(\boldsymbol{r}) = \begin{cases} \hat{\boldsymbol{n}}^{\pm} \times \hat{\boldsymbol{\ell}}, & \boldsymbol{r} \in S_n \,, \\ 0, & \text{otherwise} \end{cases} \tag{3.7}$$

and

$$\boldsymbol{g}_n(\boldsymbol{r}) = \begin{cases} \hat{\boldsymbol{\ell}}, & \boldsymbol{r} \in S_n \,, \\ 0, & \text{otherwise} \end{cases} \tag{3.8}$$

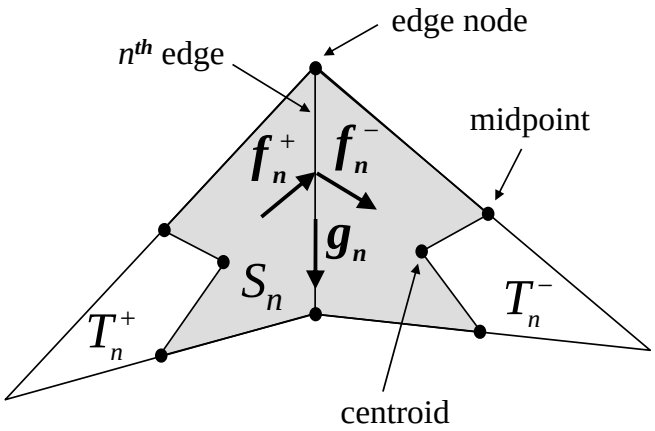

Figure 3.2: Basis function description.

where S_n represents the region obtained by connecting the mid-points of the free edges to the centroids of triangles $T_n^{\pm}$ and to the nodes of edge n. This area is shown shaded in Fig. 3.2. Also, $\hat{\boldsymbol{\ell}}$ and $\hat{\boldsymbol{n}}^{\pm}$ represent the unit vector along the n^{th} edge and the unit vector normal to the plane of the triangle $T_n^{\pm}$, respectively. Note that the basis functions defined in (3.7) and (3.8) are actually pulse functions, orthogonal to each other, defined over the region S_n. The electromagnetic solution procedure using the basis functions $\boldsymbol{f}_n$ was described in the previous chapter, and in this chapter we present a similar solution using the basis functions $\boldsymbol{g}_n$.

It may also be noted here that the basis functions $\boldsymbol{g}_n$ are less versatile than the basis functions $\boldsymbol{f}_n$. Unlike the basis functions $\boldsymbol{f}_n$, which are applicable to both open and closed bodies as demonstrated in chapter 2, the basis functions $\boldsymbol{g}_n$ are applicable to closed bodies only. The main reason for this restriction is that the functions $\boldsymbol{g}_n$ are defined parallel to the edges of the planar triangular patches and represent the tangential component of the current. It is well-known that the tangential component of the surface current is undefined for an open surface at the boundary. However, our primary motivation to use these functions is their applicability in the solution of the dielectric body problem, which is always posed for a closed body. Hence, the basis functions $\boldsymbol{g}_n$ do not hinder our purpose.

3.5 Numerical Solution Procedure

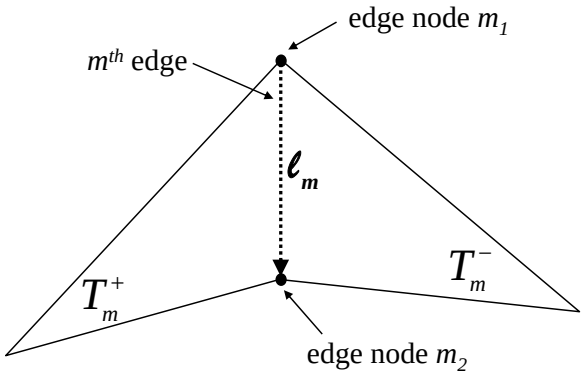

Figure 3.3: Testing path associated with the m^{th} edge.

As a first step, we consider the testing procedure. Consider the m^{th} interior edge, associated with triangles $T_m^{\pm}$. We integrate the vector component of (3.1) along the m^{th} edge, shown in Fig. 3.3, to obtain

$$\int_{\boldsymbol{\ell}_m} j\omega \boldsymbol{A}(\boldsymbol{r}) \bullet d\boldsymbol{\ell} + \int_{\boldsymbol{\ell}_m} \nabla \Phi(\boldsymbol{r}) \bullet d\boldsymbol{\ell} \;\; = \;\; \int_{\boldsymbol{\ell}_m} \boldsymbol{E}^i(\boldsymbol{r}) \bullet d\boldsymbol{\ell} \tag{3.9}$$

which may be re-written as

$$\int_{\boldsymbol{\ell}_m} j\omega \boldsymbol{A}(\boldsymbol{r}) \bullet d\boldsymbol{\ell} + \Phi_n^{m2} - \Phi_n^{m1} \;\; = \;\; \int_{\boldsymbol{\ell}_m} \boldsymbol{E}^i(\boldsymbol{r}) \bullet d\boldsymbol{\ell} \tag{3.10}$$

for $n = 1, 2, 3, \cdots, N$, where n represents the source charge region and N represents the total number of edges in the triangulation scheme. Note that in (3.10), Φ_n^{m1} and Φ_n^{m2} represent the scalar potentials evaluated at the nodes connected to the m^{th} edge. Further, the integrals appearing in (3.10) may be easily evaluated using any accurate numerical integration algorithm such as the one-point, two-point or four-point trapezoidal rule. In this work, we choose to use a two-point method.

Next, we consider the expansion procedure. Using the basis functions $\boldsymbol{g}_n$ defined in (3.8), we approximate the unknown current $\boldsymbol{J}_S$ as

$$\boldsymbol{J}_S = \sum_{n=1}^{N} I_n \, \boldsymbol{g}_n \, . \tag{3.11}$$

This is followed by a substitution of the current expansion (3.11) into (3.10), yielding an $N \times N$ system of linear equations which may be written in matrix form as $\boldsymbol{ZI} = \boldsymbol{V}$, where $\boldsymbol{Z} = [Z_{mn}]$ is an $N \times N$ matrix and $\boldsymbol{I} = [I_n]$ and $\boldsymbol{V} = [V_m]$ are column vectors of length N. The elements of the $\boldsymbol{Z}$ and $\boldsymbol{V}$ are given by

$$Z_{mn} = j\omega \int_{\boldsymbol{\ell}_m} \boldsymbol{A}_n \bullet d\boldsymbol{\ell} + \Phi_n^{m2} - \Phi_n^{m1} \tag{3.12}$$

$$V_m = \int_{\boldsymbol{\ell}_m} \boldsymbol{E}^i \bullet d\boldsymbol{\ell} \tag{3.13}$$

where

$$\boldsymbol{A}_n = \mu \iint_S \boldsymbol{g}_n \, \frac{e^{-jkR}}{4\pi R} \, dS' \tag{3.14}$$

$$\Phi_n^{m1} = \frac{-1}{j\omega\epsilon} \iint_S \nabla_s \bullet \boldsymbol{g}_n \, \frac{e^{-jkR_n^{m1}}}{4\pi R_n^{m1}} \, dS' \tag{3.15}$$

$$\Phi_n^{m2} = \frac{-1}{j\omega\epsilon} \iint_S \nabla_s \bullet \boldsymbol{g}_n \, \frac{e^{-jkR_n^{m2}}}{4\pi R_n^{m2}} \, dS' \tag{3.16}$$

$$R = \left| \boldsymbol{r} - \boldsymbol{r}' \right| \tag{3.17}$$

$$R_n^{m1} = \left| \boldsymbol{r}_{m1} - \boldsymbol{r}' \right| \tag{3.18}$$

$$R_n^{m2} = \left| \boldsymbol{r}_{m2} - \boldsymbol{r}' \right| \tag{3.19}$$

and $\boldsymbol{r}_{m1}$ and $\boldsymbol{r}_{m2}$ are the position vectors to the nodes $m1$ and $m2$, respectively, connected to the m^{th} edge.

The numerical evaluation of the vector potential, shown in (3.14), is straightforward and may be accomplished by the procedure described by Wilton et al. [35]. However, the

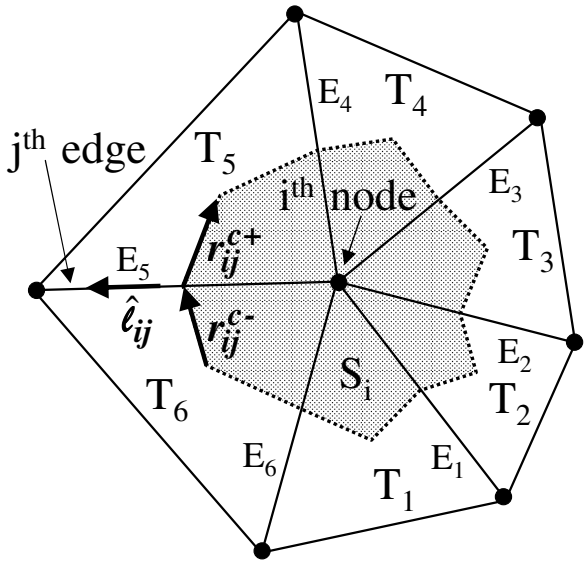

Figure 3.4: Electric charge patch around the i^{th} node.

numerical evaluation of the scalar potential terms described in (3.15) and (3.16) may be carried out as follows:

Let us define the unknown charge density q_S in (3.3) as

$$q_S = \sum_{i=1}^{N_n} \alpha_i P_i \tag{3.20}$$

where N_n represents the total number of nodes (vertices) in the model, α_i is an unknown coefficient, and

$$P_i(\boldsymbol{r}) = \begin{cases} 1, & \boldsymbol{r} \in S_i\,, \\ 0, & \text{otherwise}\,. \end{cases} \tag{3.21}$$

In (3.21), S_i is the i^{th} charge patch, formed by connecting the centers of the edges and the centroids of the triangles associated with the node i, as shown by the shaded area in Fig. 3.4.

Now, let us consider the i^{th} charge patch. Using (3.6), the well-known divergence theorem, and simple vector calculus, we have

$$\begin{aligned} \iint_{S_i} q_S \, dS &= \int_{S_i} \frac{\nabla_s \bullet \boldsymbol{J}_S}{-j\omega} \, dS \\ &= \frac{j}{\omega} \oint_{C_i} \boldsymbol{J}_S \bullet \hat{\boldsymbol{n}}_\ell \, d\ell \end{aligned} \tag{3.22}$$

where C_i is the contour bounding the charge patch S_i, and $\hat{\boldsymbol{n}}_\ell$ is the unit vector normal to the contour C_i in the plane of the triangle containing the contour segment. By considering the left hand side of (3.22), we have

$$\begin{aligned} \iint_{S_i} q_S \, dS &= \iint_{S_i} \alpha_i \, dS \\ &= \alpha_i \, \mathcal{A}_{Si} \end{aligned} \tag{3.23}$$

where $\mathcal{A}_{Si}$ represents the area of the charge patch S_i. Considering the right hand side of (3.22), we have

$$\frac{j}{\omega} \oint_{C_i} \boldsymbol{J}_S \bullet \hat{\boldsymbol{n}}_\ell \, d\ell = \frac{j}{\omega} \sum_{j=1}^{E_K} I_{ij} [\hat{\boldsymbol{\ell}}_{ij} \bullet (\hat{\boldsymbol{n}}_{ij}^{+} \times \boldsymbol{r}_{ij}^{c+} + \hat{\boldsymbol{n}}_{ij}^{-} \times \boldsymbol{r}_{ij}^{c-})] \tag{3.24}$$

where $\hat{\boldsymbol{\ell}}_{ij}$ and $\hat{\boldsymbol{n}}_{ij}^{\pm}$, respectively, represent the unit vector along the j^{th} edge connected to node i and the outward unit vector normal to the plane of the $T_{ij}^{\pm}$ triangle associated with the j^{th} edge connected to node i. As shown in Fig. 3.4, the vector $\boldsymbol{r}_{ij}^{c-}$ extends from the centroid of the T_{ij}^{-} triangle to the center of the j^{th} edge, while $\boldsymbol{r}_{ij}^{c+}$ extends from the edge center to the centroid of the T_{ij}^{+} triangle. Also, E_K represents the total number of edges connected to node i. Using (3.23) and (3.24), we have

$$\alpha_i = \frac{j}{\omega \mathcal{A}_{Si}} \sum_{j=1}^{E_K} I_{ij} [\hat{\boldsymbol{\ell}}_{ij} \bullet (\hat{\boldsymbol{n}}_{ij}^{+} \times \boldsymbol{r}_{ij}^{c+} + \hat{\boldsymbol{n}}_{ij}^{-} \times \boldsymbol{r}_{ij}^{c-})] \, . \tag{3.25}$$

Substituting the basis function $\boldsymbol{g}$ for $\hat{\boldsymbol{\ell}}$, we can write the scalar potential terms in (3.15) and (3.16) as

$$\begin{aligned}
\Phi_n^{m1} &= \frac{j}{\omega\epsilon}\left[\frac{\boldsymbol{g}_n \bullet (\hat{\boldsymbol{n}}_n^+ \times \boldsymbol{r}_n^{c+} + \hat{\boldsymbol{n}}_n^- \times \boldsymbol{r}_n^{c-})}{\mathcal{A}_{Sn1}} \iint_{S_{n1}} \frac{e^{-jkR_{n1}^{m1}}}{4\pi R_{n1}^{m1}}\, dS'\right. \\
&\quad \left. - \frac{\boldsymbol{g}_n \bullet (\hat{\boldsymbol{n}}_n^+ \times \boldsymbol{r}_n^{c+} + \hat{\boldsymbol{n}}_n^- \times \boldsymbol{r}_n^{c-})}{\mathcal{A}_{Sn2}} \iint_{S_{n2}} \frac{e^{-jkR_{n2}^{m1}}}{4\pi R_{n2}^{m1}}\, dS'\right] \\
&= \frac{j}{\omega\epsilon}\, \boldsymbol{g}_n \bullet \left(\hat{\boldsymbol{n}}_n^+ \times \boldsymbol{r}_n^{c+} + \hat{\boldsymbol{n}}_n^- \times \boldsymbol{r}_n^{c-}\right) \\
&\quad \left(\frac{1}{\mathcal{A}_{S_{n1}}} \iint_{S_{n1}} \frac{e^{-jkR_{n1}^{m1}}}{4\pi R_{n1}^{m1}}\, dS' - \frac{1}{\mathcal{A}_{S_{n2}}} \iint_{S_{n2}} \frac{e^{-jkR_{n2}^{m1}}}{4\pi R_{n2}^{m1}}\, dS'\right) \qquad (3.26) \\
\Phi_n^{m2} &= \frac{j}{\omega\epsilon}\left[\frac{\boldsymbol{g}_n \bullet (\hat{\boldsymbol{n}}_n^+ \times \boldsymbol{r}_n^{c+} + \hat{\boldsymbol{n}}_n^- \times \boldsymbol{r}_n^{c-})}{\mathcal{A}_{Sn1}} \iint_{S_{n1}} \frac{e^{-jkR_{n1}^{m2}}}{4\pi R_{n1}^{m2}}\, dS'\right. \\
&\quad \left. - \frac{\boldsymbol{g}_n \bullet (\hat{\boldsymbol{n}}_n^+ \times \boldsymbol{r}_n^{c+} + \hat{\boldsymbol{n}}_n^- \times \boldsymbol{r}_n^{c-})}{\mathcal{A}_{Sn2}} \iint_{S_{n2}} \frac{e^{-jkR_{n2}^{m2}}}{4\pi R_{n2}^{m2}}\, dS'\right] \\
&= \frac{j}{\omega\epsilon}\, \boldsymbol{g}_n \bullet \left(\hat{\boldsymbol{n}}_n^+ \times \boldsymbol{r}_n^{c+} + \hat{\boldsymbol{n}}_n^- \times \boldsymbol{r}_n^{c-}\right) \\
&\quad \left(\frac{1}{\mathcal{A}_{S_{n1}}} \iint_{S_{n1}} \frac{e^{-jkR_{n1}^{m2}}}{4\pi R_{n1}^{m2}}\, dS' - \frac{1}{\mathcal{A}_{S_{n2}}} \iint_{S_{n2}} \frac{e^{-jkR_{n2}^{m2}}}{4\pi R_{n2}^{m2}}\, dS'\right) \qquad (3.27)
\end{aligned}$$

where $\boldsymbol{r}_{m1}$, $\boldsymbol{r}_{m2}$, $\boldsymbol{r}_{n1}$, and $\boldsymbol{r}_{n2}$ are the position vectors to nodes $m1$ and $m2$ connected to the edge m, and nodes $n1$ and $n2$ connected to the edge n, respectively. Further, S_{n1} and S_{n2} are the charge patches associated with the nodes $n1$ and $n2$, respectively, as depicted in Fig. 3.5. The integrals in (3.26) and (3.27) may be evaluated with the procedures described in [35] .

Finally, once the matrices $\boldsymbol{Z}$ and $\boldsymbol{V}$ are determined, we may easily solve the system of linear equations to obtain $\boldsymbol{I}$.

3.6 Numerical Results

In this section, we present numerical results for a PEC sphere (diameter = $0.15\,\lambda$) and a cube (length = $0.15\,\lambda$), and we compare the results with the solutions obtained using the procedure presented in chapter 2. Also, for the case of the sphere, the results are compared with the exact solution. The sphere and the cube are modeled with 500 and 960 triangles,

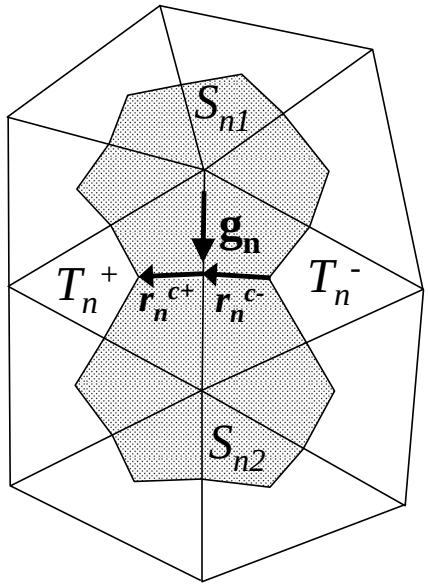

Figure 3.5: Electric source patches S_{n1} and S_{n2} for Φ_{mn} calculation.

respectively. For both examples, the body is placed symmetrically at the center of the coordinate system and illuminated by an x-polarized plane wave traveling in the negative direction along the z-axis. The bistatic radar cross sections are presented in Figs. 3.6 and 3.7. We note that the new basis function results compare well with those determined by other methods.

3.7 Summary

In this chapter, we have applied a new set of basis functions, which we called the $\boldsymbol{g}$ basis functions, for the method of moments solution of electromagnetic scattering by conducting bodies of arbitrary shape. The new basis functions are pulse basis vectors defined over a pair of triangular patches and tangential to the common edge. We have shown that similar numerical results are obtained by using the $\boldsymbol{f}$ basis function perpendicular to the edge or the $\boldsymbol{g}$ basis function tangential to the edge; in order to do this we changed the testing function as well as the basis function. The present set of basis functions along with the functions discussed in our previous chapter should prove helpful in obtaining a stable and

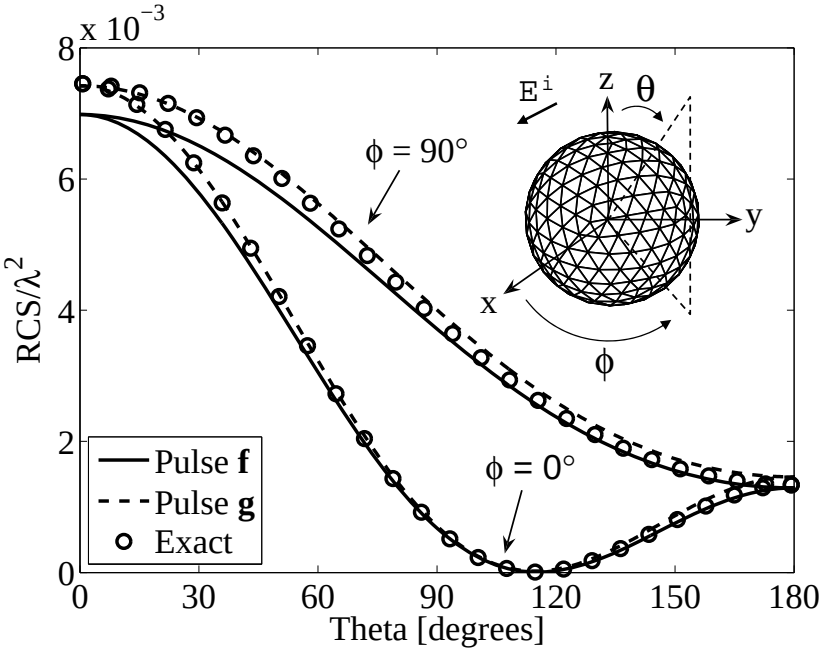

Figure 3.6: Bistatic RCS of a sphere of diameter 0.15 λ excited by a plane wave traveling in the -z direction.

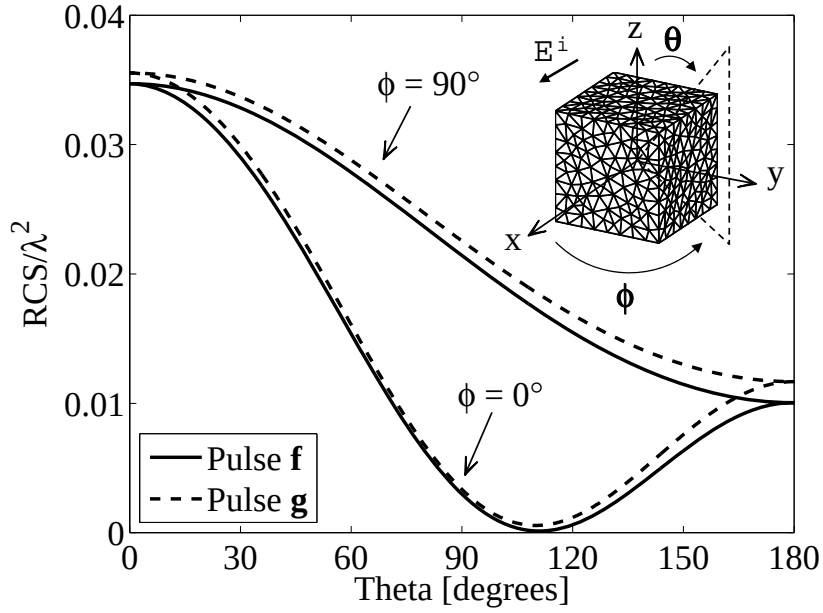

Figure 3.7: Bistatic RCS of a cube of length 0.15 λ excited by a plane wave traveling in the -z direction.

well-conditioned solution to the material body problem. The new basis function pair will be applied to material bodies in chapters 4 and 5.

Chapter 4

Electromagnetic Scattering from Arbitrarily-Shaped Dielectric Bodies Using Paired Pulse Vector Basis Functions and Method of Moments

4.1 Overview

In the previous two chapters, we demonstrated a pair of orthogonal pulse vector basis functions for the calculation of electromagnetic scattering from arbitrarily-shaped conducting bodies. In this chapter, we extend the use of the same two basis vectors, $\boldsymbol{f}$ and $\boldsymbol{g}$, to solve dielectric body problems. Further, the numerical solution procedures to calculate scalar and vector potentials for the dielectric case are based upon procedures shown in the last two chapters. The reason to use an orthogonal basis function pair is now made apparent by the calculations required for either the electric field integral equation (EFIE) or the magnetic field integral equation (HFIE) dielectric solution. The importance of demonstrating both EFIE and HFIE solutions is to show the suitability of the basis functions for combined field formulations in order to guarantee unique solutions at all frequencies. In this chapter, we detail the implementations for EFIE and HFIE formulations and show example results for canonical figures.

4.2 Introduction

For scattering problems concerning perfect electric conductors (PEC's) of arbitrary shape and of electrical size in the resonance region, the method of moments (MoM) has provided a practical means of solution using surface integral equations [3]. MoM solutions are particularly advantageous for calculating radar cross sections (RCS's) when compared to differential methods such as the finite element method, because the MoM solution incorporates a Green's function that, by definition, reduces the scattered field strengths to zero at

infinite distance. When the scattering objects are PEC or homogeneous dielectric bodies, the boundary problem can be solved by surface integral equations, resulting in a computational savings compared to volume integral equations. Numerous successful meshing schemes and basis functions have been employed for surface integral PEC MoM problems. For example, a popular combination has been triangular patch modeling in combination with Rao-Wilton-Glisson (RWG) [28] vector basis functions to expand the unknown equivalent electric surface currents [2]. For the more complex case of dielectric scattering, several authors [37], [38] have represented equivalent electric and magnetic surface currents with a single basis function. A computational difficulty then arises because the testing functions and the basis functions are all vectors having the same direction; implementation of the curl operation in the integral equations results in zero-valued or very small diagonal impedance matrix terms and an unstable numerical solution.

To provide a more stable solution for dielectric bodies, we use orthogonally placed, pulse basis vectors defined over each contiguous pair of triangular patches: one for the equivalent electric surface current $\boldsymbol{J}_S$ and one for the equivalent magnetic surface current $\boldsymbol{M}_S$. This combination ensures strongly diagonal MoM matrices. The basis functions for $\boldsymbol{M}_S$ and $\boldsymbol{J}_S$ are placed parallel and perpendicular, respectively, to each edge in the triangular patch scheme, providing a smooth transition from dielectric areas to conducting areas. Consequently, the proposed pulse vector basis functions may be used to solve composite problems. The surface integral technique described here is suitable for dielectric regions of homogeneous composition and requires the scattering bodies to be modeled as closed surfaces.

To avoid the ill-conditioned problem associated with characteristic frequencies, the paired pulse vector basis functions may be used in integral equations for any of the combined field methods. In the past, the combined field integral equation (CFIE) technique has been used to model conductors [4], while the Poggio-Miller-Chang-Harrington-Wu-Tsai (PMCHWT) [5], [6] technique or the Müller [39] technique has been used to model dielectric

bodies. Pulse pair vector basis functions allow the use of any combined field method for dielectric bodies.

In the following sections, we discuss the integral equations for dielectric scatterers. The basis and testing functions are defined and implemented for EFIE and HFIE formulations. Numerical examples are presented to show the calculated RCS for a number of canonical geometries.

4.3 Integral Equations

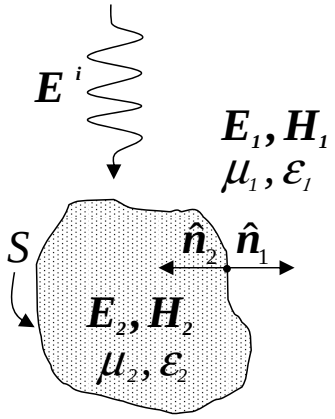

Figure 4.1: An arbitrarily-shaped dielectric body with surface S excited by an external source.

Figure 4.1 shows an arbitrarily-shaped, closed dielectric body with surface S. An unseen source in region 1 outside the body is radiating at a frequency of ω; the incident electric field is labeled $\boldsymbol{E}^i$. For this problem, there is no source inside the body in region 2. The media in regions 1 and 2 are characterized by μ_1 and ϵ_1, μ_2 and ϵ_2, respectively. We write the resulting fields, equivalent surface currents, and their associated potentials as phasor quantities that are understood to vary at the same frequency ω. Our objective will be to calculate $\boldsymbol{J}_S$ and $\boldsymbol{M}_S$, fictitious surface currents on S that would produce the same scattered $\boldsymbol{E}$ and $\boldsymbol{H}$ as the actual source. By applying the equivalence principle [2], [5], we

write the EFIE's for the dielectric body:

$$\left[j\,\omega \boldsymbol{A}_1 + \nabla \Phi_1 + \frac{1}{\varepsilon_1} \nabla \times \boldsymbol{F}_1 \right]_{tan} = \left[\boldsymbol{E}_1^i \right]_{tan} \tag{4.1}$$

$$\left[j\,\omega \boldsymbol{A}_2 + \nabla \Phi_2 + \frac{1}{\varepsilon_2} \nabla \times \boldsymbol{F}_2 \right]_{tan} = 0 \tag{4.2}$$

where the magnetic and electric vector potentials, $\boldsymbol{A}_i$ and $\boldsymbol{F}_i$ for $i = 1, 2$, are defined in terms of the equivalent currents as

$$\boldsymbol{A}_i = \mu_i \iint_S \boldsymbol{J}_S \, G_i \, dS' \tag{4.3}$$

$$\boldsymbol{F}_i = \epsilon_i \iint_S \boldsymbol{M}_S \, G_i \, dS' \tag{4.4}$$

and the electric scalar potential Φ_i is defined as

$$\Phi_i = \frac{1}{\epsilon_i} \iint_S q_S^e \, G_i \, dS' \tag{4.5}$$

$$= \frac{j}{\omega \epsilon_i} \iint_S \nabla \bullet \boldsymbol{J}_S \, G_i \, dS'. \tag{4.6}$$

The Green's function G_i is defined as

$$G_i = \frac{e^{-jk_i R}}{4\pi R} \tag{4.7}$$

$$R = |\boldsymbol{r} - \boldsymbol{r}'|, \tag{4.8}$$

μ_i and ϵ_i are the permeability and permittivity constants of the surrounding medium, S' denotes the source surface, and k_i is the wave number for each region. The vectors $\boldsymbol{r}$ and $\boldsymbol{r}'$ are position vectors to observation and source points, respectively, from a global coordinate origin. The electric charge density q_S^e is related to the unknown surface current $\boldsymbol{J}_S$ by the continuity equation, given by

$$\nabla \bullet \boldsymbol{J}_S = -j\omega \, q_S^e \, . \tag{4.9}$$

By Maue's integral [29],

$$-\hat{\boldsymbol{n}}_1 \times \nabla \times \iint_S \boldsymbol{M}_S G_1 \, dS' = \frac{\boldsymbol{M}_S}{2} - \hat{\boldsymbol{n}}_1 \times \cancel{\iint}_S \nabla G_1 \times \boldsymbol{M}_S \, dS' \tag{4.10}$$

where $\hat{\boldsymbol{n}}_1$ is the unit vector normal to S pointing away from the surface into region 1 and the deleted integral symbol $\cancel{\iint}$ indicates the principal value. The normal $\hat{\boldsymbol{n}}_1$ and its opposite, $\hat{\boldsymbol{n}}_2$, are shown in Fig. 4.1. Taking the cross product of $\hat{\boldsymbol{n}}_1$ with each side of (4.10), we may write the curl operation in (4.1) as

$$\begin{aligned} \frac{1}{\varepsilon_1} \nabla \times \boldsymbol{F}_1 &= \nabla \times \iint_S \boldsymbol{M}_S \, G_1 \, dS' \\ &= \hat{\boldsymbol{n}}_1 \times \frac{\boldsymbol{M}_S}{2} + \cancel{\iint}_S \nabla G_1 \times \boldsymbol{M}_S \, dS' \, . \end{aligned} \tag{4.11}$$

Similarly, for the surface in region 2, we obtain

$$\nabla \times \iint_S \boldsymbol{M}_S \, G_2 \, dS' = \hat{\boldsymbol{n}}_2 \times \frac{\boldsymbol{M}_S}{2} + \cancel{\iint}_S \nabla G_2 \times \boldsymbol{M}_S \, dS' \, . \tag{4.12}$$

Thus, using the modifications presented in (4.11) and (4.12), the EFIE's for the dielectric body may be written as

$$\left[j\,\omega \boldsymbol{A}_1 + \nabla \Phi_1 + \hat{\boldsymbol{n}}_1 \times \frac{\boldsymbol{M}_S}{2} + \cancel{\iint}_S \nabla G_1 \times \boldsymbol{M}_S \, dS' \right]_{tan} = \left[\boldsymbol{E}_1^i \right]_{tan} \tag{4.13}$$

$$\left[j\,\omega \boldsymbol{A}_2 + \nabla \Phi_2 + \hat{\boldsymbol{n}}_2 \times \frac{\boldsymbol{M}_S}{2} + \cancel{\iint}_S \nabla G_2 \times \boldsymbol{M}_S \, dS' \right]_{tan} = 0 \, . \tag{4.14}$$

Next, again invoking the equivalence principle, we write the HFIE's for the dielectric body:

$$\left[j\,\omega \boldsymbol{F}_1 + \nabla \Psi_1 - \frac{1}{\mu_1} \nabla \times \boldsymbol{A}_1 \right]_{tan} = \left[\boldsymbol{H}_1^i \right]_{tan} \tag{4.15}$$

$$\left[j\,\omega \boldsymbol{F}_2 + \nabla \Psi_2 - \frac{1}{\mu_2} \nabla \times \boldsymbol{A}_2 \right]_{tan} = 0 \tag{4.16}$$

where the magnetic scalar potential Ψ_i for $i = 1, 2$ is defined as

$$\Psi_i = \frac{1}{\mu_i} \iint_S q_S^m \, G_i \, dS' \tag{4.17}$$

$$= \frac{j}{\omega \mu_i} \iint_S \nabla \bullet \boldsymbol{M}_S \, G_i \, dS' \tag{4.18}$$

and q_S^m is the magnetic charge density related to the fictitious magnetic current density by the equation

$$\nabla \bullet \boldsymbol{M}_S = -j\omega \, q_S^m \, . \tag{4.19}$$

By reasoning analogous to that used in expanding the EFIE's, we may rewrite the HFIE's for the dielectric body as

$$\left[j \, \omega \boldsymbol{F}_1 + \nabla \, \Psi_1 - \hat{\boldsymbol{n}}_1 \times \frac{\boldsymbol{J}_S}{2} - \iint\!\!\!\!\!\!-_S \nabla G_1 \times \boldsymbol{J}_S \, dS' \right]_{tan} = \left[\boldsymbol{H}_1^i \right]_{tan} \tag{4.20}$$

$$\left[j \, \omega \boldsymbol{F}_2 + \nabla \, \Psi_2 - \hat{\boldsymbol{n}}_2 \times \frac{\boldsymbol{J}_S}{2} - \iint\!\!\!\!\!\!-_S \nabla G_2 \times \boldsymbol{J}_S \, dS' \right]_{tan} = 0 \, . \tag{4.21}$$

Note that for either the EFIE or the HFIE method, the region 1 and region 2 equations look similar.

When the MoM matrix is calculated for (4.13) and (4.14), the $\boldsymbol{M}_S/2$ terms will be the dominant terms in the sub-matrix dealing with the $\boldsymbol{E}(\boldsymbol{M}_S)$ portion of the evaluation. Similarly, when the MoM matrix is calculated for (4.20) and (4.21), the $\boldsymbol{J}_S/2$ terms will dominate the $\boldsymbol{H}(\boldsymbol{J}_S)$ portion of the evaluation. It is important that we choose the proper basis and testing functions so that this dominance is preserved in the numerical solution.

4.4 Basis and Testing Functions

Let us assume that the surface is modeled by a triangular mesh. T_n^+ and T_n^- represent two triangles connected to the n^{th} edge of the triangulated surface model as shown in Fig. 4.2. The edges of each triangle other than the n^{th} edge we will call *free* edges. Within each triangle, the surface is planar. We define two mutually orthogonal vector basis

functions associated with the n^{th} edge as

$$\boldsymbol{f}_n(\boldsymbol{r}) = \begin{cases} \hat{\boldsymbol{n}}^{\pm} \times \boldsymbol{g}_n, & \boldsymbol{r} \in S_n\,, \\ 0, & \text{otherwise} \end{cases} \tag{4.22}$$

and

$$\boldsymbol{g}_n(\boldsymbol{r}) = \begin{cases} \text{unit vector} \parallel n^{th} \text{ edge}, & \boldsymbol{r} \in S_n\,, \\ 0, & \text{otherwise} \end{cases} \tag{4.23}$$

where $\hat{\boldsymbol{n}}^{\pm}$ represents the unit vector normal to the plane of the triangle $T_n^{\pm}$. S_n represents the domain of the basis functions: the region whose perimeter is drawn by connecting the mid-points of the free edges to the centroids of triangles $T_n^{\pm}$ and to the nodes of edge n. Shown as a shaded area in Fig. 4.2, S_n is 2/3 of the total triangular patch area. Note that the basis functions defined in (4.22) and (4.23) are unit pulse functions orthogonal to each other. Throughout the problem solution, we will use $\boldsymbol{f}_n$ to expand $\boldsymbol{J}_S$ and $\boldsymbol{g}_n$ to expand $\boldsymbol{M}_S$.

The testing functions associated with edge m are vectors $\boldsymbol{t}_m^{\pm}$ and $\boldsymbol{\ell}_m$, for EFIE and HFIE solutions, respectively, as shown in Fig. 4.3. Vector $\boldsymbol{t}_m^{+}$ extends from the triangle T_m^{+} centroid to the edge m midpoint; $\boldsymbol{t}_m^{-}$ extends from the edge m midpoint to the triangle T_m^{-} centroid. Vector $\boldsymbol{\ell}_m$ extends from the beginning to the end of edge m, in the direction of $\boldsymbol{g}_m$.

4.5 Numerical Solution Procedure

We have discretized the surface of interest using a triangular mesh containing a total of N edges. The MoM solution procedure results in $2N$ linear equations, written as

$$\begin{Bmatrix} [\boldsymbol{Z}_1(\boldsymbol{J}_S)] & [\boldsymbol{Z}_1(\boldsymbol{M}_S)] \\ [\boldsymbol{Z}_2(\boldsymbol{J}_S)] & [\boldsymbol{Z}_2(\boldsymbol{M}_S)] \end{Bmatrix} \begin{Bmatrix} [\boldsymbol{J}_S] \\ [\boldsymbol{M}_S] \end{Bmatrix} = \begin{Bmatrix} [\boldsymbol{V}_1] \\ [\boldsymbol{V}_2] \end{Bmatrix} \tag{4.24}$$

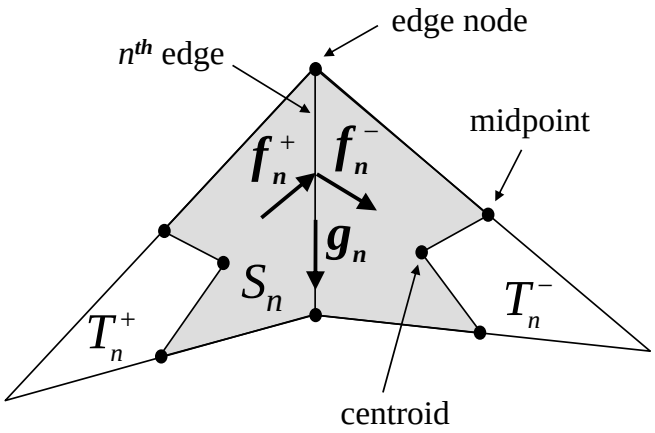

Figure 4.2: Basis functions $\boldsymbol{f}_n$ and $\boldsymbol{g}_n$ associated with the n^{th} edge.

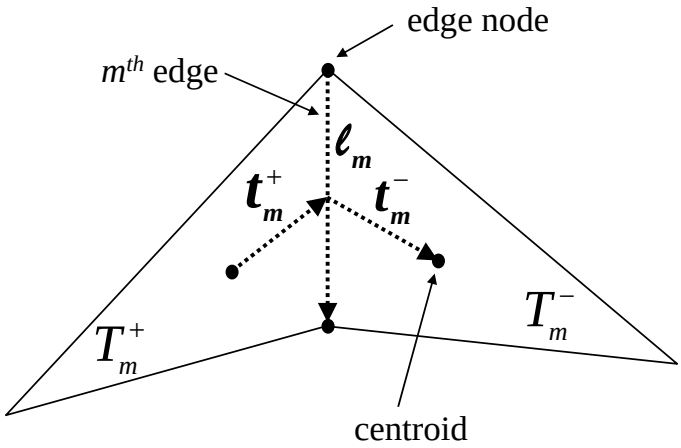

Figure 4.3: Testing functions $\boldsymbol{t}_m$ and $\boldsymbol{\ell}_m$ associated with the m^{th} edge.

where $[\boldsymbol{Z}_1(\boldsymbol{J}_S)]$, $[\boldsymbol{Z}_1(\boldsymbol{M}_S)]$, $[\boldsymbol{Z}_2(\boldsymbol{J}_S)]$, and $[\boldsymbol{Z}_2(\boldsymbol{M}_S)]$ are $N \times N$ matrices and the numerical subscripts refer to the medium in which the matrix elements are evaluated. $[\boldsymbol{J}_S]$ and $[\boldsymbol{M}_S]$ are column vectors of length N. For the EFIE solution,

$$[\boldsymbol{V}_1] = \left[\boldsymbol{E}_1^i \;\; \boldsymbol{E}_2^i \;\; \cdots \;\; \boldsymbol{E}_N^i\right]^T, \tag{4.25}$$

for the HFIE solution,

$$[\boldsymbol{V}_1] = \left[\boldsymbol{H}_1^i \;\; \boldsymbol{H}_2^i \;\; \cdots \;\; \boldsymbol{H}_N^i\right]^T, \tag{4.26}$$

and for either solution,

$$[\boldsymbol{V}_2] = [0_1 \;\; 0_2 \;\; \cdots \;\; 0_N]^T. \tag{4.27}$$

The four $\boldsymbol{Z}$ matrices represent the influence of the incident $\boldsymbol{E}$ and $\boldsymbol{H}$-fields on edge currents in regions 1 and 2.

In order to write Z_{mn} in scalar terms, we integrate each of the equations (4.13), (4.14), (4.20), and (4.21) along the appropriate m^{th} testing vector. Letting $\hat{\boldsymbol{n}}_1 = -\hat{\boldsymbol{n}}_2$, we obtain for the EFIE in region 1:

$$\begin{aligned} j\,\omega \boldsymbol{A}_1 \bullet \boldsymbol{t}_m \;\; &+ \;\; \Phi_n^- - \Phi_n^+ + \left(\hat{\boldsymbol{n}}_1 \times \frac{\boldsymbol{M}_S}{2}\right) \bullet \boldsymbol{t}_m \\ &+ \;\; \left(\iint\!\!\!\!\!\!\diagup_S \nabla G_1 \times \boldsymbol{M}_S \, dS'\right) \bullet \boldsymbol{t}_m = \boldsymbol{E}_1^i \bullet \boldsymbol{t}_m \end{aligned} \tag{4.28}$$

for the EFIE in region 2:

$$\begin{aligned} j\,\omega \boldsymbol{A}_2 \bullet \boldsymbol{t}_m \;\; &+ \;\; \Phi_n^- - \Phi_n^+ - \left(\hat{\boldsymbol{n}}_1 \times \frac{\boldsymbol{M}_S}{2}\right) \bullet \boldsymbol{t}_m \\ &+ \;\; \left(\iint\!\!\!\!\!\!\diagup_S \nabla G_2 \times \boldsymbol{M}_S \, dS'\right) \bullet \boldsymbol{t}_m = 0 \end{aligned} \tag{4.29}$$

for the HFIE in region 1:

$$j\,\omega \boldsymbol{F}_1 \bullet \boldsymbol{\ell}_m \;\; + \;\; \Psi_n^2 - \Psi_n^1 - \left(\hat{\boldsymbol{n}}_1 \times \frac{\boldsymbol{J}_S}{2}\right) \bullet \boldsymbol{\ell}_m \\ - \;\; \left(\iint\!\!\!\!\!\!\diagup_S \nabla G_1 \times \boldsymbol{J}_S \, dS'\right) \bullet \boldsymbol{\ell}_m = \boldsymbol{H}_1^i \bullet \boldsymbol{\ell}_m \tag{4.30}$$

and for the HFIE in region 2:

$$j\,\omega \boldsymbol{F}_2 \bullet \boldsymbol{\ell}_m \;\; + \;\; \Psi_n^2 - \Psi_n^1 + \left(\hat{\boldsymbol{n}}_1 \times \frac{\boldsymbol{J}_S}{2}\right) \bullet \boldsymbol{\ell}_m \\ - \;\; \left(\iint\!\!\!\!\!\!\diagup_S \nabla G_2 \times \boldsymbol{J}_S \, dS'\right) \bullet \boldsymbol{\ell}_m = 0\,. \tag{4.31}$$

In (4.28–4.31), n = 1, 2, 3, ..., N identifies the location of the source charge. Expressions of the form $\left(\int_{\boldsymbol{t}_m} \nabla \Phi \bullet \boldsymbol{t}_m\right)$ have been simplified to the form $(\Phi_n^- - \Phi_n^+)$, where Φ_n^- and Φ_n^+ are the scalar potentials due to charges near the n^{th} edge evaluated at the minus and plus ends of the testing vector, as defined by the assigned current direction [28]. Areas of magnetic positive and negative charge have been designated by superscripts *1* and *2*, respectively.

Next, we expand the currents $\boldsymbol{J}_S$ and $\boldsymbol{M}_S$ as

$$\boldsymbol{J}_S \;\; = \;\; \sum_{n=1}^{N} I_n \, \boldsymbol{f}_n \tag{4.32}$$

and

$$\boldsymbol{M}_S \;\; = \;\; \sum_{n=1}^{N} I_{N+n} \, \boldsymbol{g}_n \tag{4.33}$$

where $[I]$ is the column matrix of complex scalar coefficients. Substituting (4.32) and (4.33) into (4.28-4.31) yields a $2N \times 2N$ system of linear equations which may be written in matrix form as $[Z][I] = [V]$, corresponding to the elements of (4.24). For the EFIE solution,

region 1, the elements Z_{mn} are given by

$$Z_{mn}(\boldsymbol{J}_S) = j\omega \boldsymbol{A}_n \bullet \boldsymbol{t}_m + \Phi_n^- - \Phi_n^+ \tag{4.34}$$

$$Z_{mn}(\boldsymbol{M}_S) = \left(\hat{\boldsymbol{n}}_1 \times \frac{\boldsymbol{g}_n}{2}\right) \bullet \boldsymbol{t}_m + \left(\iint\!\!\!\!\!\!\diagup_S \nabla G_1 \times \boldsymbol{g}_n \, dS'\right) \bullet \boldsymbol{t}_m \tag{4.35}$$

where $\boldsymbol{A}_n$ and Φ_n are given by the definitions of $\boldsymbol{A}$ and Φ, (4.3) and (4.6), respectively, except that $\boldsymbol{f}_n$ has replaced $\boldsymbol{J}_S$ and the source areas are restricted to the n^{th} source regions. The elements Z_{mn} for the EFIE solution, region 2, are found in a similar manner. For the HFIE solution, region 1, the elements Z_{mn} are given by

$$Z_{mn}(\boldsymbol{J}_S) = -\left(\hat{\boldsymbol{n}}_1 \times \frac{\boldsymbol{f}_n}{2}\right) \bullet \boldsymbol{\ell}_m - \left(\iint\!\!\!\!\!\!\diagup_S \nabla G_1 \times \boldsymbol{f}_n \, dS'\right) \bullet \boldsymbol{\ell}_m \tag{4.36}$$

$$Z_{mn}(\boldsymbol{M}_S) = j\,\omega \boldsymbol{F}_n \bullet \boldsymbol{\ell}_m + \Psi_n^2 - \Psi_n^1 \tag{4.37}$$

where $\boldsymbol{F}_n$ and Ψ_n are given by the definitions of $\boldsymbol{F}$ and Ψ, (4.4) and (4.18), respectively, except that $\boldsymbol{g}_n$ has replaced $\boldsymbol{M}_S$ and the source areas are restricted to the n^{th} source regions. The elements Z_{mn} for the HFIE solution, region 2, are found in a similar manner. The calculation of the vector and scalar potentials is detailed in the following three sections.

The elements V_m are given by

$$V_{1m} = \boldsymbol{E}_m^i \bullet \boldsymbol{t}_m, \quad \text{EFIE solution, region 1} \tag{4.38}$$

$$V_{2m} = 0, \qquad \text{EFIE solution, region 2} \tag{4.39}$$

$$V_{1m} = \boldsymbol{H}_m^i \bullet \boldsymbol{\ell}_m, \quad \text{HFIE solution, region 1} \tag{4.40}$$

$$V_{2m} = 0, \qquad \text{HFIE solution, region 2}\,. \tag{4.41}$$

Once the matrices $[Z]$ and $[V]$ have been determined, the unknowns in $[I]$ may be calculated by matrix algebra. The equivalent surface currents so determined may be used to calculate fields inside or outside the scattering body, as desired.

4.5.1 Calculation of $\boldsymbol{A}$ and $\boldsymbol{F}$

The following discussion applies to both regions 1 and 2, and the subscripts have been dropped for $\boldsymbol{A}$, $\boldsymbol{F}$, ϵ, μ, and $\hat{\boldsymbol{n}}$. The vector potentials $\boldsymbol{A}_{mn}$ and $\boldsymbol{F}_{mn}$ are found by numerical integration of the Green's function over the n^{th} source region shown shaded in Fig. 4.2. The observation points $\boldsymbol{r}$ in the Green's function definition are points chosen on or near the testing vector; for this work, we obtained good EFIE and HFIE results by using one T_m^+ point and one T_m^- point. Each test point was the centroid of the smaller triangle whose nodes were the n^{th} edge nodes and the T triangle centroid. These observation points are sketched in Fig. 4.4, in which the vector potential observation points are marked by o's, the scalar potential observation points by x's. The final testing equations are written to incorporate this segmentation of the vector potential, e.g.,

$$j\,\omega \boldsymbol{A}_{mn} \bullet \boldsymbol{t}_m \;\Rightarrow\; j\,\omega \left(\boldsymbol{A}_{mn}^{+} \bullet \boldsymbol{t}_m^{+} + \boldsymbol{A}_{mn}^{-} \bullet \boldsymbol{t}_m^{-}\right) \tag{4.42}$$

$$j\,\omega \boldsymbol{F}_{mn} \bullet \boldsymbol{\ell}_m \;\Rightarrow\; \frac{j\,\omega}{2} \left(\boldsymbol{F}_{mn}^{+} + \boldsymbol{F}_{mn}^{-}\right) \bullet \boldsymbol{\ell}_m \tag{4.43}$$

where $\boldsymbol{A}_{mn}^{+}$ and $\boldsymbol{F}_{mn}^{+}$ are the vector potentials observed at $\boldsymbol{t}_m^{+}$ due to the n^{th} source region, and $\boldsymbol{A}_{mn}^{-}$ and $\boldsymbol{F}_{mn}^{-}$ are the vector potentials observed at $\boldsymbol{t}_m^{-}$ due to the n^{th} source region.

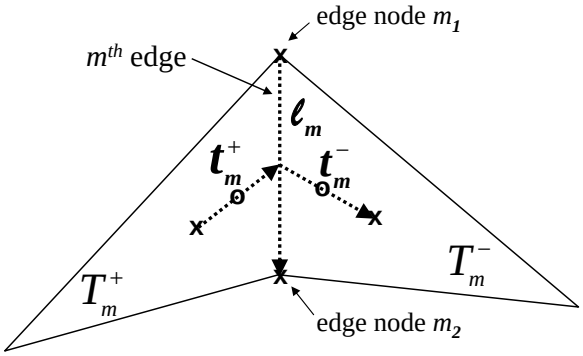

Figure 4.4: Observation points for mn^{th} vector (o) and scalar (x) potentials.

4.5.2 Calculation of $\nabla \times \boldsymbol{F}$ and $\nabla \times \boldsymbol{A}$

The dielectric EFIE contains the term $\nabla \times \boldsymbol{F}$, as shown in (4.1) and (4.2). In the corresponding testing equation,

$$\left(\frac{1}{\epsilon}\nabla \times \boldsymbol{F}_{m,n}\right) \bullet \boldsymbol{t}_m = \left(\hat{\boldsymbol{n}}^+ \times \frac{\boldsymbol{g}_n}{2}\right) \bullet \boldsymbol{t}_m^+ + \left(\hat{\boldsymbol{n}}^- \times \frac{\boldsymbol{g}_n}{2}\right) \bullet \boldsymbol{t}_m^- + \left(\iint\!\!\!\!\!\!\diagup_S \nabla G^+ \times \boldsymbol{g}_n dS'\right) \bullet \boldsymbol{t}_m^+ + \left(\iint\!\!\!\!\!\!\diagup_S \nabla G^- \times \boldsymbol{g}_n dS'\right) \bullet \boldsymbol{t}_m^- \quad (4.44)$$

where $\hat{\boldsymbol{n}}^{\pm}$ denotes the normal to the $T_m^{\pm}$ field patch and the G superscript also refers to the $T_m^{\pm}$ field patch associated with the Green's function. Because the basis function $\boldsymbol{g}_n$ is constant over the n^{th} source region, it may be moved outside the integral before the cross product is calculated. The calculation of $\nabla \times \boldsymbol{A}_{mn}$ is analogous. Thus,

$$\left(-\frac{1}{\mu}\nabla \times \boldsymbol{A}_{mn}\right) \bullet \boldsymbol{\ell}_m = -\left(\hat{\boldsymbol{n}}^+ \times \frac{\boldsymbol{f}_n^+}{2} + \hat{\boldsymbol{n}}^- \times \frac{\boldsymbol{f}_n^-}{2}\right) \bullet \frac{\boldsymbol{\ell}_m}{2} - \left(\iint\!\!\!\!\!\!\diagup_{S^{\pm}} \nabla G^+ \times \boldsymbol{f}_n^{\pm} dS' + \iint\!\!\!\!\!\!\diagup_{S^{\pm}} \nabla G^- \times \boldsymbol{f}_n^{\pm} dS'\right) \bullet \frac{\boldsymbol{\ell}_m}{2} \,. \quad (4.45)$$

4.5.3 Calculation of Φ and Ψ

We have stated in (4.6) that the electric scalar potential Φ is defined as

$$\Phi = \frac{j}{\omega\epsilon} \iint_S \nabla \bullet \boldsymbol{J}_S \, G \, dS' \,.$$

Because the basis function $\boldsymbol{f}_n$ is a pulse function, direct calculation of $\nabla \bullet \boldsymbol{f}_n$ would produce impulse functions at the edges of the source charge region. Rather than integrating impulse functions, we will use the divergence theorem to calculate $\iint_S \nabla \bullet \boldsymbol{J}_S \, dS'$ directly. Assuming that $\nabla \bullet \boldsymbol{J}_S$ is constant over a triangular source area and given that

$$\iint_S \nabla \bullet \boldsymbol{J}_S \, dS' = \oint_C \boldsymbol{J}_S \bullet \hat{\boldsymbol{n}}_C \, dC \quad (4.46)$$

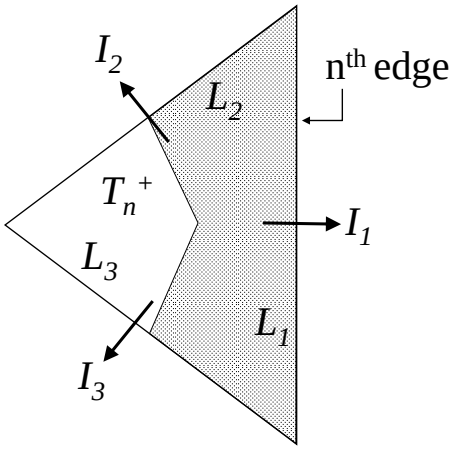

Figure 4.5: Normal electric current components for Φ calculation.

where $\hat{\boldsymbol{n}}_C$ is the unit vector normal to the contour in the plane of surface S', we may write Φ for a source triangle (shown in Fig. 4.5) as

$$\Phi = \frac{j\left(I_1 L_1 + I_2 L_2 + I_3 L_3\right)}{\omega \epsilon \mathcal{A}} \iint_S G \, dS' \tag{4.47}$$

where I_1, I_2, and I_3 are the current components of $\boldsymbol{J}_S$ normal to the three sides; L_1, L_2, and L_3 are the side lengths; and $\mathcal{A}$ is the triangle area.

The unknown electric charge density q_S^e may be defined as

$$q_S^e = \sum_{i=1}^{N_T} \alpha_i P_i \tag{4.48}$$

where N_T is the number of triangular patches in the model,

$$\alpha_i \;=\; \frac{j}{\omega}\left[\frac{I_{i_1}\ell_{i_1} + I_{i_2}\ell_{i_2} + I_{i_3}\ell_{i_3}}{\mathcal{A}_i}\right], \tag{4.49}$$

and

$$P_i(\boldsymbol{r}) = \begin{cases} 1, & \boldsymbol{r} \in T_i\,, \\ 0, & \text{otherwise}\,. \end{cases} \tag{4.50}$$

In order to calculate Φ_{mn}, we assume that the electric charge associated with $\boldsymbol{J}_n$ is now spread out from S_n (in Fig. 4.2) over the two larger, triangular regions $T_n^{\pm}$. For the mn^{th} scalar potential term,

$$\Phi_{mn}^{+} = \frac{j}{\omega\epsilon}\left(\frac{I_n L_n}{\mathcal{A}^{+}}\boldsymbol{f}_n^{+}\iint_{T_n^{+}} G^{+}\, dS' - \frac{I_n L_n}{\mathcal{A}^{-}}\boldsymbol{f}_n^{-}\iint_{T_n^{-}} G^{+}\, dS'\right) \tag{4.51}$$

where the superscript on G indicates that the observation point lies on T_m^{+}, and the potentials associated with T_n^{+} and T_n^{-} have been differenced to obtain a result for the n^{th} edge, observed from the m^{th} edge. Φ_{mn}^{-} is similarly calculated with the observation point on T_m^{-}. Equation (4.51) applies to both regions 1 and 2.

To calculate the scalar magnetic potential, we likewise start by defining areas of magnetic charge associated with each edge current $\boldsymbol{M}_n$. Let us define the unknown charge density q_S^m in (4.17) as

$$q_S^m = \sum_{i=1}^{N_N} \alpha_i P_i \tag{4.52}$$

where N_N represents the total number of nodes (vertices) in the model, α_i is a scalar to be determined, and

$$P_i(\boldsymbol{r}) = \begin{cases} 1, & \boldsymbol{r} \in S_i\,, \\ 0, & \text{otherwise}\,. \end{cases} \tag{4.53}$$

In (4.53), S_i is the i^{th} charge patch, formed by connecting the centers of the edges and the centroids of the triangles associated with the i^{th} node, as shown by the shaded area in Fig. 4.6. Again making use of the divergence theorem, we can write Ψ for the i^{th} source patch as

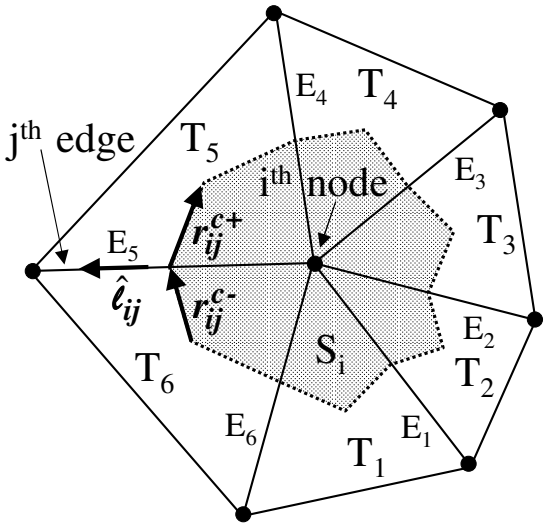

Figure 4.6: Magnetic charge source area for Ψ calculation.

$$\Psi = \frac{j}{\omega\mu}\iint_S \nabla \bullet \boldsymbol{M}_S\, G\, dS' \tag{4.54}$$

$$= \frac{j}{\omega\mu}\oint_C \boldsymbol{M}_S \bullet \hat{\boldsymbol{n}}_C\, dC \iint_S G\, dS' \tag{4.55}$$

$$= \frac{j}{\omega\mu\mathcal{A}_i}\left\{\sum_{j=1}^{N_E} I_{ij}\left[\hat{\boldsymbol{\ell}}_{ij} \bullet (\hat{\boldsymbol{n}}_{ij}^{+} \times \boldsymbol{r}_{ij}^{c+} + \hat{\boldsymbol{n}}_{ij}^{-} \times \boldsymbol{r}_{ij}^{c-})\right]\right\}\left\{\iint_S G dS'\right\} \tag{4.56}$$

where $\hat{\boldsymbol{\ell}}_{ij}$ and $\hat{\boldsymbol{n}}_{ij}^{\pm}$, respectively, represent the unit vector along the j^{th} edge connected to node i and the outward unit vector normal to the plane of the $T_{ij}^{\pm}$ triangle associated with the j^{th} edge connected to node i. The vector $\boldsymbol{r}_{ij}^{c-}$ extends from the centroid of the T_{ij}^{-} triangle to the center of the j^{th} edge, while $\boldsymbol{r}_{ij}^{c+}$ extends from the edge center to the centroid of the T_{ij}^{+} triangle. N_E represents the total number of edges connected to node i and $\mathcal{A}_i$ is the area of S_i. From (4.56), we see that α_i in (4.52) is

$$\alpha_i = \frac{j}{\omega\mathcal{A}_i}\sum_{j=1}^{N_E} I_{ij}\left[\hat{\boldsymbol{\ell}}_{ij} \bullet (\hat{\boldsymbol{n}}_{ij}^{+} \times \boldsymbol{r}_{ij}^{c+} + \hat{\boldsymbol{n}}_{ij}^{-} \times \boldsymbol{r}_{ij}^{c-})\right]. \tag{4.57}$$

In order to calculate Ψ_{mn}, we will use the positive and negative magnetic charge patches, designated S_{n1} and S_{n2} respectively, associated with the n^{th} edge and shown in Fig. 4.7. We will find the normal components of $\boldsymbol{g}_n$ flowing across the mutual boundary, designated $\boldsymbol{r}_n^{c+}$ and $\boldsymbol{r}_n^{c-}$ in Fig. 4.7. The value of Ψ_{mn}^{1}, the scalar potential at the n^{th} edge as observed from end node 1 on the m^{th} edge, is

$$\begin{aligned}
\Psi_{mn}^{1} &= \frac{j}{\omega\mu\mathcal{A}_{S_{n1}}}\boldsymbol{g}_n \bullet \left(\hat{\boldsymbol{n}}_n^{+} \times \boldsymbol{r}_n^{c+} + \hat{\boldsymbol{n}}_n^{-} \times \boldsymbol{r}_n^{c-}\right)\left(\iint_{S_{n1}} G^1 dS'\right) \\
&\quad -\frac{j}{\omega\mu\mathcal{A}_{S_{n2}}}\boldsymbol{g}_n \bullet \left(\hat{\boldsymbol{n}}_n^{+} \times \boldsymbol{r}_n^{c+} + \hat{\boldsymbol{n}}_n^{-} \times \boldsymbol{r}_n^{c-}\right)\left(\iint_{S_{n2}} G^1 dS'\right) \\
&= \frac{j}{\omega\mu}\boldsymbol{g}_n \bullet \left(\hat{\boldsymbol{n}}_n^{+} \times \boldsymbol{r}_n^{c+} + \hat{\boldsymbol{n}}_n^{-} \times \boldsymbol{r}_n^{c-}\right) \\
&\quad \left(\frac{1}{\mathcal{A}_{S_{n1}}}\iint_{S_{n1}} G^1 dS' - \frac{1}{\mathcal{A}_{S_{n2}}}\iint_{S_{n2}} G^1 dS'\right). \qquad (4.58)
\end{aligned}$$

In (4.58), the superscript on G refers to the end of the m^{th} edge where the observation is made. A similar calculation is done to find Ψ_{mn}^{2}. The equations are the same for regions 1 and 2.

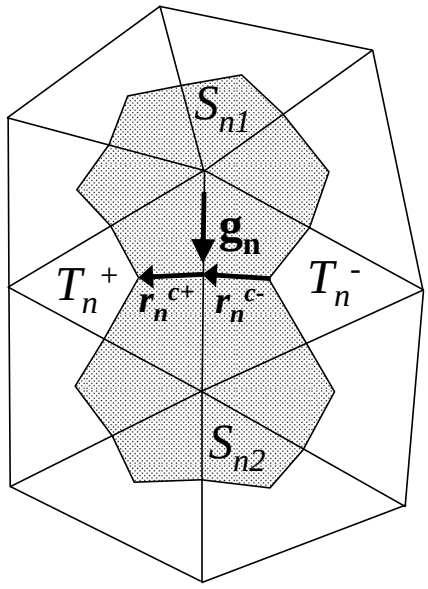

Figure 4.7: Magnetic source patches S_{n1} and S_{n2} for Ψ_{mn} calculation.

4.5.4 Testing the Incident Fields

We test the $\boldsymbol{V}$ matrix as follows:

$$V_m = \boldsymbol{t}_m^+ \bullet \boldsymbol{E}^{i+} + \boldsymbol{t}_m^- \bullet \boldsymbol{E}^{i-}, \quad \text{EFIE solution} \tag{4.59}$$

where $\boldsymbol{E}^i$ is evaluated at the vector potential test points, near the midpoints of the test vectors $\boldsymbol{t}$.

$$V_m = \boldsymbol{\ell}_m \bullet \boldsymbol{H}^i, \quad \text{HFIE solution} \tag{4.60}$$

where $\boldsymbol{H}^i$ is evaluated at the midpoint of the test vector $\boldsymbol{\ell}$.

4.6 Numerical Examples

For three dielectric scatterers, a sphere, a cube, and a cone, the bistatic RCS has been calculated by both EFIE and HFIE solution methods, incorporating pulse basis vector functions. The MoM solutions are compared to solutions from at least one other calculation method.

A sphere of radius 0.1 λ and $\epsilon_R = 4$ is irradiated by a plane wave traveling in the +z direction. Its mesh contains 500 patches and 750 edges. The MoM RCS is calculated by using pulse basis functions and is compared to the Mie series analytic result. The orientation of the sphere and the cube to the incident wave are shown in Fig. 4.8; the sphere RCS plots are shown in Figs. 4.10 and 4.11.

A cube of length 0.2 λ and $\epsilon_R = 4$ is irradiated by a plane wave traveling in the +z direction. Its mesh contains 480 patches and 720 edges. The MoM RCS is calculated by using pulse basis functions and is compared to surface and volume integral results reported by Sarkar, Arvas, and Ponapalli [40] for the same case. The cube RCS plots are shown in Figs. 4.12 and 4.13.

A cone of radius 0.1 λ, apex half-angle = 30°, and $\epsilon_R = 3$ is irradiated by a plane wave traveling in the -z direction. Its mesh contains 606 patches and 909 edges. The MoM RCS

is calculated by using pulse basis functions and is compared to MoM body of revolution (BOR) results. The orientation of the cone to the incident wave is shown in Fig. 4.9; the RCS plots are shown in Figs. 4.14 and 4.15.

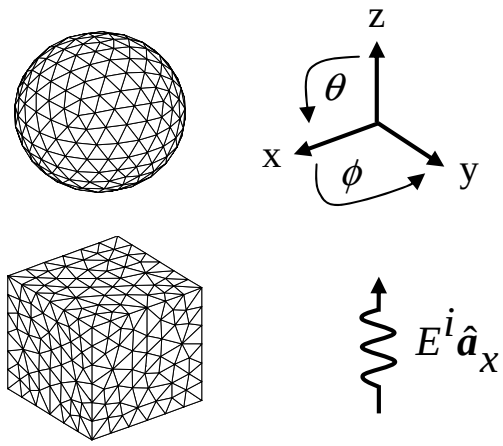

Figure 4.8: Orientation of dielectric sphere and cube to the incident plane wave. Sphere radius = 0.1 λ; $\epsilon_R = 4$. Cube length = 0.2 λ; $\epsilon_R = 4$.

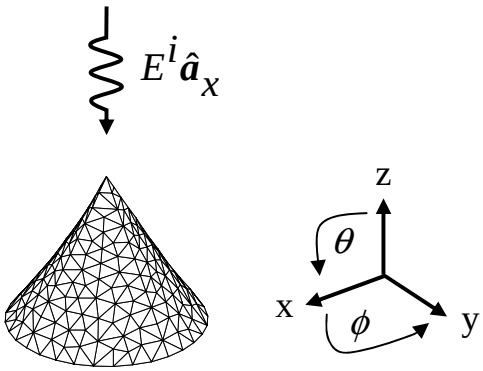

Figure 4.9: Orientation of dielectric cone to the incident plane wave. Cone radius = 0.1 λ; apex half-angle = 30 °; $\epsilon_R = 3$.

The RCS plots show good agreement between the pulse vector basis results and the standards of comparison. There is some difference between the EFIE and HFIE results; at this time, no generalizations can be made concerning the conditions under which either

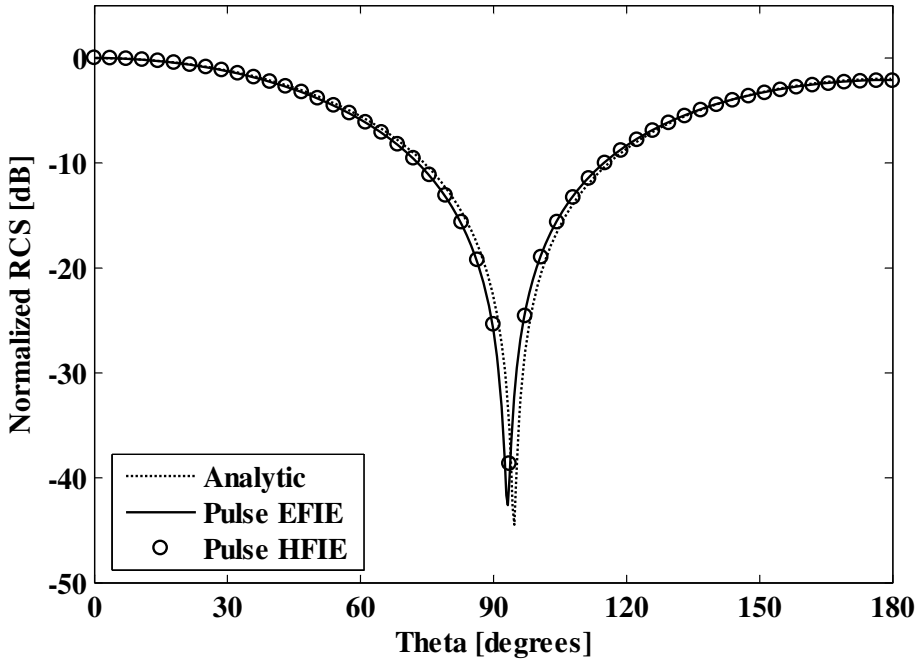

Figure 4.10: Bistatic RCS for a dielectric sphere at $\phi = 0\,^\circ$, radius = 0.1 λ, $\epsilon_R = 4$.

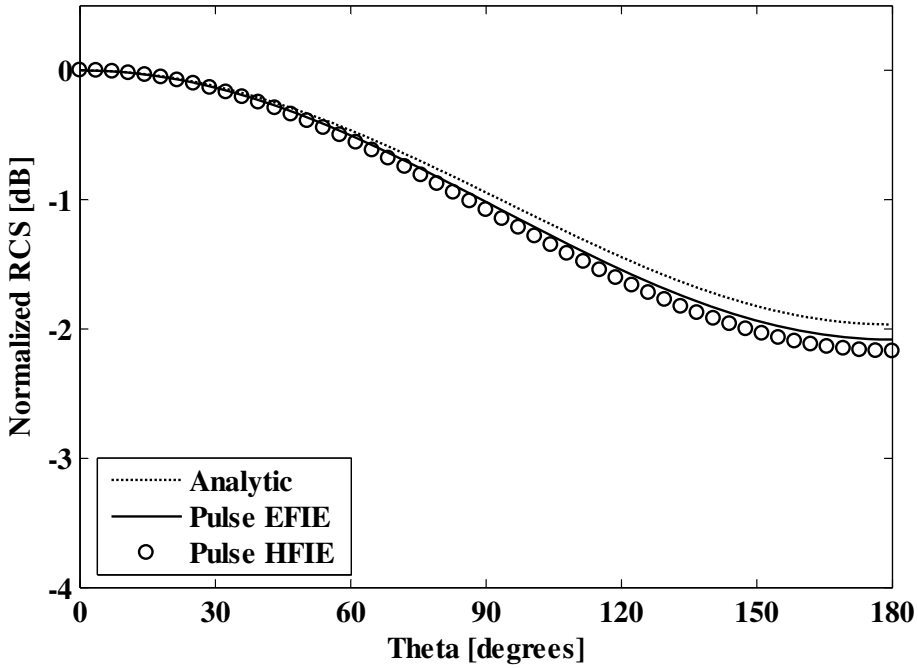

Figure 4.11: Bistatic RCS for a dielectric sphere at $\phi = 90\,^\circ$, radius = 0.1 λ, $\epsilon_R = 4$.

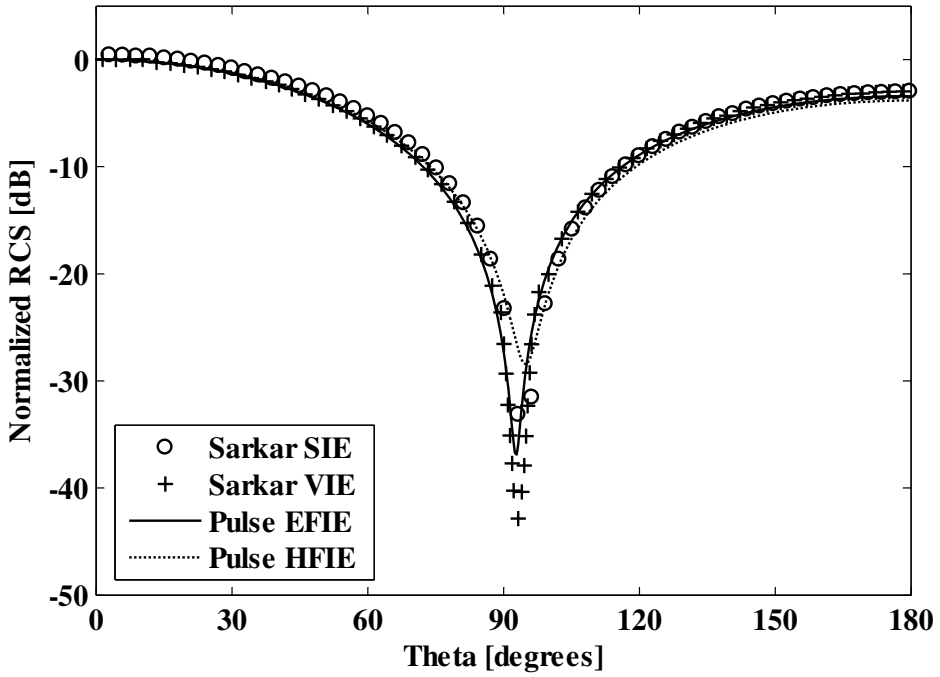

Figure 4.12: Bistatic RCS for a dielectric cube at $\phi = 0\,^\circ$, length = 0.2 λ, $\epsilon_R = 4$.

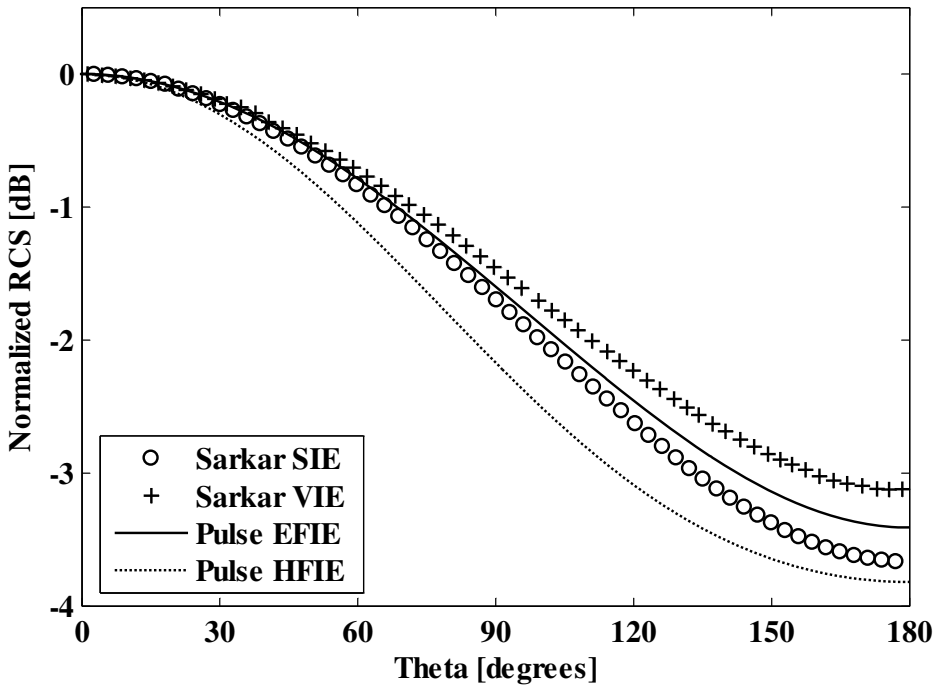

Figure 4.13: Bistatic RCS for a dielectric cube at $\phi = 90\,^\circ$, length = 0.2 λ, $\epsilon_R = 4$.

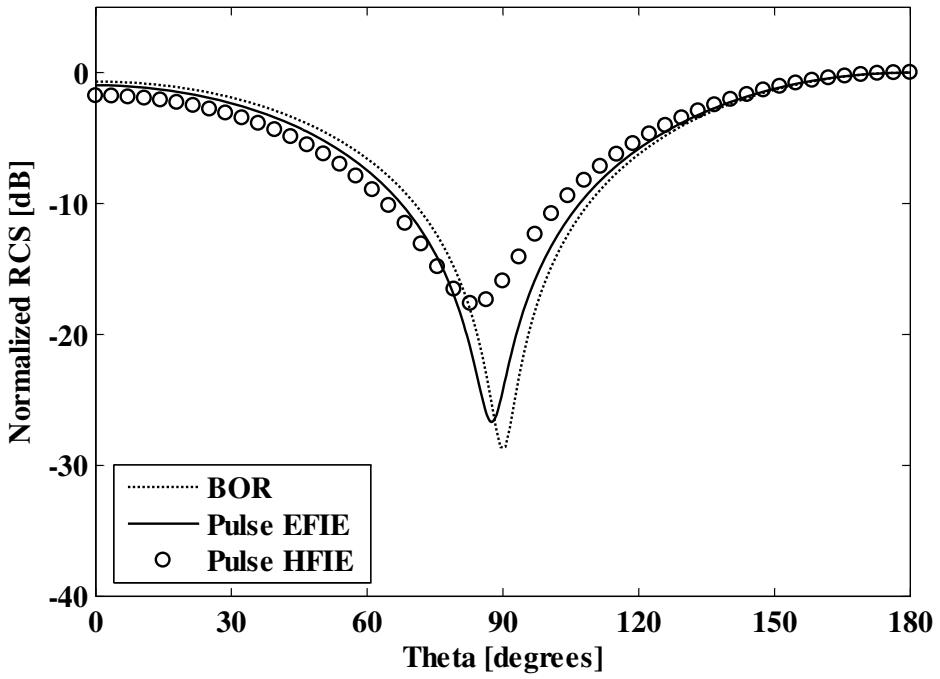

Figure 4.14: Bistatic RCS for a dielectric cone at $\phi = 0°$, radius = 0.1 λ, apex half-angle = 30°, $\epsilon_R = 3$, incident wave traveling toward apex.

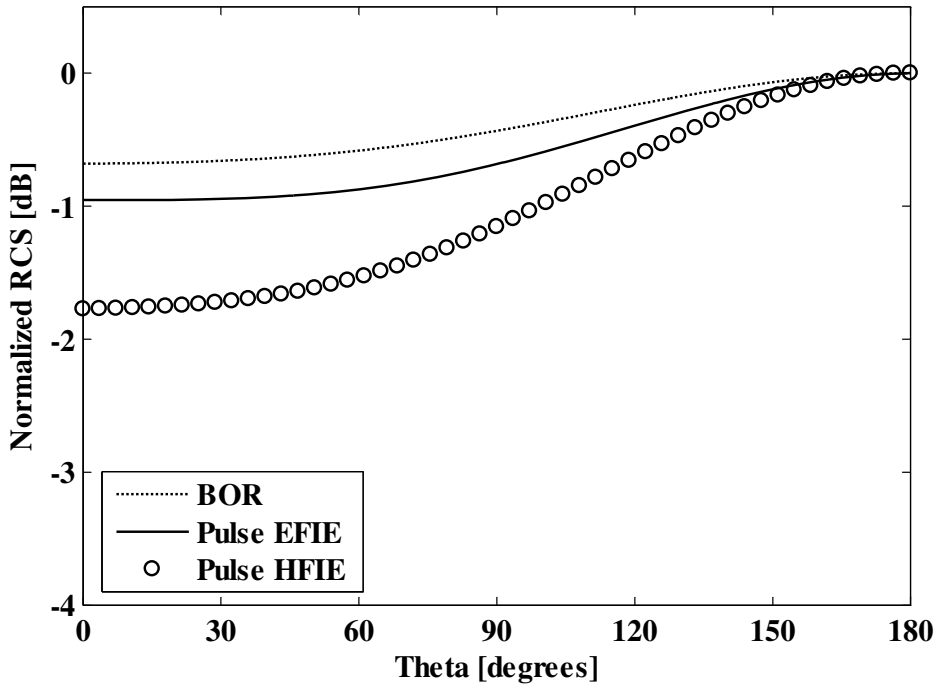

Figure 4.15: Bistatic RCS for a dielectric cone at $\phi = 90°$, radius = 0.1 λ, apex half-angle = 30°, $\epsilon_R = 3$, incident wave traveling toward apex.

method is superior. Scattering from smoother objects, as expected, is more easily modeled than from ones with sharp corners or points.

4.7 Summary

In this chapter we have demonstrated the use of a pair of orthogonal pulse vector basis functions to solve dielectric MoM surface integral problems for closed bodies. We used the $\boldsymbol{f}$ basis function for electric surface currents and the $\boldsymbol{g}$ basis function for magnetic surface currents. Together with the pair of pulse basis vectors, we used testing vectors $\boldsymbol{t}$ and $\boldsymbol{\ell}$ for EFIE and HFIE solutions, respectively. An important part of the numerical solution procedure was the expression of the electric and magnetic scalar and vector potentials, which themselves were expanded in terms of the basis functions. The pulse basis functions may be used in combined field methods to insure unique solutions at resonant frequencies. Use of these basis functions will allow reliable and accurate scattering solutions for conductors, dielectric bodies, or composites of arbitrary shape.

Chapter 5

Electromagnetic Scattering from Arbitrarily Shaped Composites Using Paired Pulse Vector Basis Functions and Method of Moments

5.1 Overview

In previous chapters, a pair of orthogonal pulse vector basis functions was demonstrated for the calculation of electromagnetic scattering from arbitrarily-shaped perfect electric conductors (PEC's) (chapters 2 and 3) or dielectric bodies (chapter 4). In this chapter, the basis functions are applied to dielectric/PEC composites. For the general case, i.e., perfect or lossy dielectric surfaces, the $\boldsymbol{f}$ and $\boldsymbol{g}$ pulse vector basis function pair is used to represent equivalent electric and magnetic surface currents. For the special case of PEC surfaces, only the $\boldsymbol{f}$ pulse vector basis function is needed to represent the equivalent electric surface current. The composite scatterer may contain multiple dielectric and PEC parts, either touching or non-touching. We describe here the scattering solution for a composite structure and we show example electric field integral equation (EFIE) and magnetic field integral equation (HFIE) results for several two- or three-part figures.

5.2 Introduction

Due to the increasing development and use of a variety of building materials, metallic and non-metallic, for all structures large and small, it is very important to be able to model correctly the scattering behavior of composite structures. For homogeneous regions in dielectric bodies, we may often calculate electromagnetic scattering more efficiently by using equivalent surface currents [2] rather than the polarization volume currents. PEC bodies naturally lend themselves to surface current modeling for another reason: the actual currents occur in a thin layer near the surface. In the previous chapters, we described a

surface integral method using orthogonally placed, pulse basis vectors for the method of moments (MoM) solution of scattering problems involving dielectric bodies [3]. The surface integral technique described here is suitable for dielectric and PEC regions of homogeneous composition; a triangular patch scheme is used for the surface mesh [28].

We wish to be able to use a common formulation for both the dielectric and the PEC components of a closed body composite structure in order to calculate scattering accurately and efficiently while avoiding the ill-conditioned problem associated with characteristic frequencies. Kishk and Shafai [32] have reviewed a number of available composite formulations. These include the combined field integral equation (CFIE) [4], the Poggio-Miller-Chang-Harrington-Wu-Tsai (PMCHWT) [5], [6], and the Müller [7] formulations. For dielectric problems, the paired pulse basis functions may be used with any of these integral equation formulations to guarantee unique solutions. However, for a composite problem, only the CFIE can be used throughout. The paired pulse basis functions allow use of the CFIE for composite scattering solutions. But, if a portion of the composite structure is described as an open body, the HFIE cannot be written; consequently, a combined field formulation cannot be used.

To provide stable EFIE or HFIE solutions for dielectric bodies, we use orthogonally placed, pulse basis vectors defined over each contiguous pair of triangular patches: one for the equivalent electric surface current $\boldsymbol{J}_S$ and one for the equivalent magnetic surface current $\boldsymbol{M}_S$. This combination allows correct calculation of the curl terms in the EFIE and HFIE, ensuring strongly diagonal moment matrices. To solve a composite problem, we model all surface currents on both the dielectric and the PEC elements with pulse vector basis functions. For the dielectric elements, we employ the orthogonal basis vector pair; for the PEC elements we retain only the electric current basis vector.

In the following sections, we discuss solutions for composite dielectric/PEC scatterers. The basis and testing functions are defined and the matrix equation is explained. Numerical examples of EFIE and HFIE solutions are presented to show the calculated radar cross sections (RCS's) for several canonical geometries, including two non-touching spheres, a

disk/cone structure, a simplified missile shape, and a cube capped with PEC plates at two ends.

5.3 Integral Equations

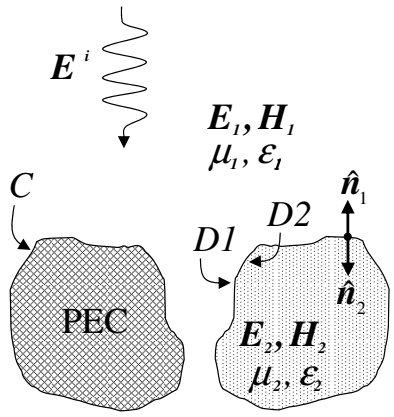

Figure 5.1: Arbitrarily-shaped PEC and dielectric bodies with surfaces C, *D1*, and *D2* excited by an external source.

Figure 5.1 shows two arbitrarily-shaped bodies, one PEC and one dielectric. An unseen source in region 1 outside the bodies is radiating at a frequency of ω. In region 1, fields $\boldsymbol{E}_1$ and $\boldsymbol{H}_1$ exist as a result of the incident energy combined with scattering from the two bodies. Surface C on the conductor exterior marks the boundary between region 1, characterized by μ_1 and ϵ_1, and the interior of the conductor, where no fields exist. Surfaces *D1* and *D2* are the two sides of the dielectric body surface separating region 1 from region 2. Region 2 inside the dielectric is characterized by μ_2 and ϵ_2 and contains fields $\boldsymbol{E}_2$ and $\boldsymbol{H}_2$. By applying the equivalence principle [2], [5], we will calculate $\boldsymbol{J}_C$, $\boldsymbol{J}_D$, and $\boldsymbol{M}_D$, fictitious surface currents on the surfaces that would produce the same scattered $\boldsymbol{E}$ and $\boldsymbol{H}$ as the actual volume sources. We write the fields, equivalent surface currents, and their associated potentials as phasor quantities that are understood to vary at the frequency ω. To solve the scattering problem by either the EFIE or the HFIE surface integral method, three equations are required. Table I lists the surfaces where the field points and current sources are located for each equation.

Table 5.1: Integral Equation Surfaces

Equation	**Field Point Location**	**Source Current Location**
I	C	C, D1
II	D1	C, D1
III	D2	D2

The EFIE's to be solved simultaneously are of the form

$$-\left[\boldsymbol{E}^s(\boldsymbol{J}_C, \boldsymbol{J}_D, \boldsymbol{M}_D)\right]_{tan} = \left[\boldsymbol{E}^i\right]_{tan} \tag{5.1}$$

where s denotes *scattered* and i denotes *incident*.

EFIE I:

$$\Big[j\,\omega\boldsymbol{A}(\boldsymbol{J}_C, \mu_1) + \nabla\Phi(\boldsymbol{J}_C, \mu_1, \varepsilon_1) + j\,\omega\boldsymbol{A}(\boldsymbol{J}_{D1}, \mu_1) + \nabla\Phi(\boldsymbol{J}_{D1}, \mu_1, \varepsilon_1) + \frac{1}{\varepsilon_1}\nabla \times \boldsymbol{F}(M_{D1}, \varepsilon_1)\Big]_{tan} = \left[\boldsymbol{E}^i_C\right]_{tan}. \tag{5.2}$$

EFIE II:

$$\Big[j\,\omega\boldsymbol{A}(\boldsymbol{J}_C, \mu_1) + \nabla\Phi(\boldsymbol{J}_C, \mu_1, \varepsilon_1) + j\,\omega\boldsymbol{A}(\boldsymbol{J}_{D1}, \mu_1) + \nabla\Phi(\boldsymbol{J}_{D1}, \mu_1, \varepsilon_1) + \frac{1}{\varepsilon_1}\nabla \times \boldsymbol{F}(M_{D1}, \varepsilon_1)\Big]_{tan} = \left[\boldsymbol{E}^i_{D1}\right]_{tan}. \tag{5.3}$$

EFIE III:

$$\Big[j\,\omega\boldsymbol{A}(\boldsymbol{J}_{D2}, \mu_2) + \nabla\Phi(\boldsymbol{J}_{D2}, \mu_2, \varepsilon_2) + \frac{1}{\varepsilon_2}\nabla \times \boldsymbol{F}(M_{D2}, \varepsilon_2)\Big]_{tan} = \left[\boldsymbol{E}^i_{D2}\right]_{tan}. \tag{5.4}$$

The magnetic and electric vector potentials, $\boldsymbol{A}$ and $\boldsymbol{F}$, respectively, are defined in terms of the equivalent currents as

$$\boldsymbol{A} = \mu \iint_S \boldsymbol{J}_S \, G \, dS' \tag{5.5}$$

$$\boldsymbol{F} = \epsilon \iint_S \boldsymbol{M}_S \, G \, dS' \tag{5.6}$$

where S represents the source surface of interest. The electric scalar potential Φ is defined as

$$\Phi = \frac{1}{\epsilon} \iint_S q_S^e \, G \, dS' \tag{5.7}$$

$$= \frac{j}{\omega\epsilon} \iint_S \nabla \bullet \boldsymbol{J}_S \, G \, dS' \tag{5.8}$$

where q_S^e is the electric charge density related to the fictitious electric current density by the equation

$$\nabla \bullet \boldsymbol{J}_S = -j\omega \, q_S^e \, . \tag{5.9}$$

The Green's function G is defined as

$$G = \frac{e^{-jkR}}{4\pi R} \tag{5.10}$$

$$R = |\boldsymbol{r} - \boldsymbol{r}'| \, , \tag{5.11}$$

μ and ϵ are the permeability and permittivity constants of the surrounding medium, S' denotes the source surface, and k is the wave number. The vectors $\boldsymbol{r}$ and $\boldsymbol{r}'$ are position vectors to observation and source points, respectively, from a global coordinate origin.

Using Maue's integral [29], we express the $\frac{1}{\varepsilon}\nabla \times \boldsymbol{F}$ portion of the EFIE's as

$$\frac{1}{\varepsilon_i}\nabla \times \boldsymbol{F}_i = \nabla \times \iint_S \boldsymbol{M}_S \, G_i \, dS'$$

$$= \hat{\boldsymbol{n}}_i \times \frac{\boldsymbol{M}_S}{2} + \iint_S \nabla G_i \times \boldsymbol{M}_S \, dS' \tag{5.12}$$

for $i = 1, 2$, where $\hat{\boldsymbol{n}}_i$ is the unit vector normal to S pointing away from the surface into region i and the deleted integral symbol $\iint\!\!\!\!\!\!-$ indicates the principal value. The normal $\hat{\boldsymbol{n}}_1$ and its opposite, $\hat{\boldsymbol{n}}_2$, are shown in Fig. 5.1.

Referring to Table I again, for the same surfaces we may write three simultaneous HFIE's of the form

$$-[\boldsymbol{H}^s(\boldsymbol{J}_C, \boldsymbol{J}_D, \boldsymbol{M}_D)]_{tan} = [\boldsymbol{H}^i]_{tan} \,. \tag{5.13}$$

HFIE I:

$$\left[-\frac{1}{\mu_1}\nabla \times \boldsymbol{A}(\boldsymbol{J}_C, \mu_1) - \frac{1}{\mu_1}\nabla \times \boldsymbol{A}(\boldsymbol{J}_{D1}, \mu_1) \right. \\ \left. + j\,\omega \boldsymbol{F}(\boldsymbol{M}_{D1}, \varepsilon_1) + \nabla\,\Psi(\boldsymbol{M}_{D1}, \mu_1, \varepsilon_1)\right]_{tan} = \left[\boldsymbol{H}^i_C\right]_{tan} \,. \tag{5.14}$$

HFIE II:

$$\left[-\frac{1}{\mu_1}\nabla \times \boldsymbol{A}(\boldsymbol{J}_C, \mu_1) - \frac{1}{\mu_1}\nabla \times \boldsymbol{A}(\boldsymbol{J}_{D1}, \mu_1) \right. \\ \left. + j\,\omega \boldsymbol{F}(\boldsymbol{M}_{D1}, \varepsilon_1) + \nabla\,\Psi(\boldsymbol{M}_{D1}, \mu_1, \varepsilon_1)\right]_{tan} = \left[\boldsymbol{H}^i_{D1}\right]_{tan} \,. \tag{5.15}$$

HFIE III:

$$\left[-\frac{1}{\mu_2}\nabla \times \boldsymbol{A}(\boldsymbol{J}_{D2}, \mu_2) + j\,\omega \boldsymbol{F}(\boldsymbol{M}_{D2}, \varepsilon_2) + \nabla\,\Psi(\boldsymbol{M}_{D2}, \mu_2, \varepsilon_2)\right]_{tan} = \left[\boldsymbol{H}^i_{D2}\right]_{tan} \,. \tag{5.16}$$

The magnetic scalar potential Ψ is defined as

$$\Psi = \frac{1}{\mu} \iint_S q^m_S \; G \; dS' \tag{5.17}$$

$$= \frac{j}{\omega\mu} \iint_S \nabla \bullet \boldsymbol{M}_S \; G \; dS' \tag{5.18}$$

and q_S^m is the magnetic charge density related to the unknown magnetic current density by the equation

$$\nabla \bullet \boldsymbol{M}_S = -j\omega\, q_S^m\,. \tag{5.19}$$

Using Maue's integral, we express the $-\frac{1}{\mu}\nabla \times \boldsymbol{A}$ portion of the HFIE's as

$$\begin{aligned} -\frac{1}{\mu_i}\nabla \times \boldsymbol{A}_i &= -\nabla \times \iint_S \boldsymbol{J}_S\, G_i\, dS' \\ &= -\hat{\boldsymbol{n}}_i \times \frac{\boldsymbol{J}_S}{2} - \iint\!\!\!\!\!\!-_S \nabla G_i \times \boldsymbol{J}_S\, dS' \end{aligned} \tag{5.20}$$

for $i = 1, 2$.

5.4 Basis and Testing Functions

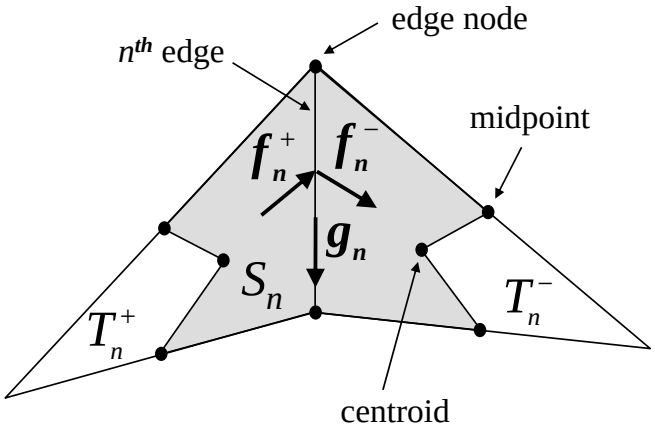

Figure 5.2: Basis functions $\boldsymbol{f}_n$ and $\boldsymbol{g}_n$ associated with the n^{th} edge.

Let us assume that the surface is modeled by a triangular mesh. T_n^+ and T_n^- represent two triangles connected to the n^{th} edge of the triangulated surface model as shown in Fig. 5.2. The edges of each triangle other than the n^{th} edge we will call *free* edges. Within each triangle, the surface is planar. We define two mutually orthogonal vector basis

functions associated with the n^{th} edge as

$$\boldsymbol{f}_n(\boldsymbol{r}) = \begin{cases} \hat{\boldsymbol{n}}^{\pm} \times \boldsymbol{g}_n, & \boldsymbol{r} \in S_n\,, \\ 0, \quad \text{otherwise} \end{cases} \tag{5.21}$$

and

$$\boldsymbol{g}_n(\boldsymbol{r}) = \begin{cases} \text{unit vector} \parallel n^{th} \text{ edge}, & \boldsymbol{r} \in S_n\,, \\ 0, \quad \text{otherwise} \end{cases} \tag{5.22}$$

where $\hat{\boldsymbol{n}}^{\pm}$ represents the unit vector normal to the plane of the triangle $T_n^{\pm}$. S_n represents the domain of the basis functions: the region whose perimeter is drawn by connecting the mid-points of the free edges to the centroids of triangles $T_n^{\pm}$ and to the nodes of edge n. Shown as a shaded area in Fig. 5.2, S_n is 2/3 of the total triangular patch area. Note that the basis functions defined in (5.21) and (5.22) are unit pulse functions, orthogonal to each other. Throughout the problem solution, we will use $\boldsymbol{f}_n$ to expand $\boldsymbol{J}_S$ and $\boldsymbol{g}_n$ to expand $\boldsymbol{M}_S$.

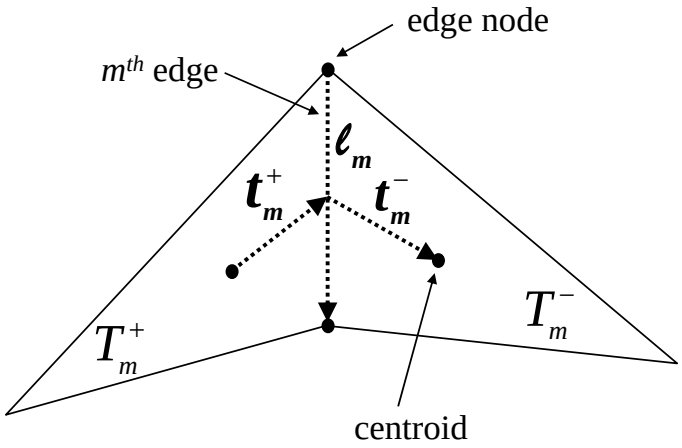

Figure 5.3: Testing functions $\boldsymbol{t}_m$ and $\boldsymbol{\ell}_m$ associated with the m^{th} edge.

The testing functions associated with edge m are vectors $\boldsymbol{t}_m^{\pm}$ and $\boldsymbol{\ell}_m$, for the EFIE and HFIE solutions, respectively, as shown in Fig. 5.3. Vector $\boldsymbol{t}_m^+$ extends from the triangle T_m^+ centroid to the edge m midpoint; $\boldsymbol{t}_m^-$ extends from the edge m midpoint to the triangle T_m^-

centroid. Vector $\boldsymbol{\ell}_m$ extends from the beginning to the end of edge m, in the direction of $\boldsymbol{g}_m$.

5.5 Numerical Solution Procedure

In this section, the EFIE and HFIE solution methods are shown for one PEC body and one dielectric body. After meshing each surface of interest, we obtain N_C edges for the conductor and N_D edges for the dielectric body. The MoM solution procedure results in $N_C + 2N_D$ linear equations, written as

$$\begin{Bmatrix} [\,\boldsymbol{Z}_C(\boldsymbol{J}_C)] & [\boldsymbol{Z}_C(\boldsymbol{J}_D)] & [\boldsymbol{Z}_C(\boldsymbol{M}_D)] \\ [\boldsymbol{Z}_{D1}(\boldsymbol{J}_C)] & [\boldsymbol{Z}_{D1}(\boldsymbol{J}_D)] & [\boldsymbol{Z}_{D1}(\boldsymbol{M}_D)] \\ [0] & [\boldsymbol{Z}_{D2}(\boldsymbol{J}_D)] & [\boldsymbol{Z}_{D2}(\boldsymbol{M}_D)] \end{Bmatrix} \begin{Bmatrix} [\boldsymbol{J}_C] \\ [\boldsymbol{J}_D] \\ [\boldsymbol{M}_D] \end{Bmatrix} = \begin{Bmatrix} [\boldsymbol{V}_C] \\ [\boldsymbol{V}_{D1}] \\ [0] \end{Bmatrix}. \quad (5.23)$$

The $\boldsymbol{Z}$ subscripts C, $D1$, and $D2$ indicate the conductor, outer dielectric, and inner dielectric surfaces, respectively, where the field points reside. $\boldsymbol{J}$ and $\boldsymbol{M}$ subscripts C and D, respectively, indicate the conductor and dielectric surfaces where the source currents reside. The (3,1) block of the moment matrix contains only zeros because, in the equivalent problem, at the inner dielectric surface, no fields are observed due to currents on the conductor.

For the EFIE solution, $[\boldsymbol{V}_C]$ and $[\boldsymbol{V}_{D1}]$ are written

$$[\boldsymbol{V}] = \begin{bmatrix} \boldsymbol{E}_1^i & \boldsymbol{E}_2^i & \cdots & \boldsymbol{E}_N^i \end{bmatrix}^T, \quad (5.24)$$

for the HFIE solution, $[\boldsymbol{V}_C]$ and $[\boldsymbol{V}_{D1}]$ are written

$$[\boldsymbol{V}] = \begin{bmatrix} \boldsymbol{H}_1^i & \boldsymbol{H}_2^i & \cdots & \boldsymbol{H}_N^i \end{bmatrix}^T, \quad (5.25)$$

and for either solution

$$[\boldsymbol{V}_{D2}] = [0_1 \;\; 0_2 \;\; \cdots \;\; 0_N]^T. \quad (5.26)$$

The $[\boldsymbol{V}_{D2}]$ column of the incident field matrix contains only zeros because the incident fields from the external source in this problem strike only the outer surfaces of each body.

In order to write Z_{mn} in scalar terms, we integrate each of the EFIE's or HFIE's along the appropriate m^{th} testing vector. Thus, we obtain for the EFIE's:

$$j\,\omega \boldsymbol{A}_i \bullet \boldsymbol{t}_m + \Phi_n^- - \Phi_n^+ + \left(\hat{\boldsymbol{n}}_i \times \frac{\boldsymbol{M}_S}{2}\right) \bullet \boldsymbol{t}_m + \left(\iint_S \nabla G_i \times \boldsymbol{M}_S \, dS'\right) \bullet \boldsymbol{t}_m = \boldsymbol{E}_i^i \bullet \boldsymbol{t}_m \quad (5.27)$$

where the subscripts on $\boldsymbol{A}$, $\hat{\boldsymbol{n}}$, G, and $\boldsymbol{E}^i$ denote the region into which the source current is radiating. Expressions of the form $\left(\int_{\boldsymbol{t}_m} \nabla \Phi \bullet \boldsymbol{t}_m\right)$ have been simplified to the form $(\Phi_n^- - \Phi_n^+)$, where Φ_n^- and Φ_n^+ are the scalar potentials due to charges near the n^{th} edge evaluated at the minus and plus ends of the testing vector, as defined by the assigned current direction [28].

Similarly, we obtain for the HFIE's:

$$j\,\omega \boldsymbol{F}_i \bullet \boldsymbol{\ell}_m + \Psi_n^2 - \Psi_n^1 - \left(\hat{\boldsymbol{n}}_i \times \frac{\boldsymbol{J}_S}{2}\right) \bullet \boldsymbol{\ell}_m - \left(\iint_S \nabla G_i \times \boldsymbol{J}_S \, dS'\right) \bullet \boldsymbol{\ell}_m = \boldsymbol{H}_i^i \bullet \boldsymbol{\ell}_m \,. \quad (5.28)$$

Next, we expand the currents $\boldsymbol{J}_S$ and $\boldsymbol{M}_S$ as

$$\boldsymbol{J}_S = \sum_{n=1}^{N} I_n \, \boldsymbol{f}_n \quad (5.29)$$

and

$$\boldsymbol{M}_S = \sum_{n=1}^{N} I_n \, \boldsymbol{g}_n \quad (5.30)$$

where $[I]$ is a column matrix of complex scalar coefficients. Substituting (5.29) and (5.30) into equations of the form (5.27) and (5.28) yields a $(2N_C + N_D) \times (2N_C + N_D)$ system of

linear equations which may be written in matrix form as $[Z][I] = [V]$, corresponding to the elements of (5.23). For the EFIE solution, the elements Z_{mn} are of the form

$$\begin{aligned} Z_{mn}(\boldsymbol{J}_S) &= j\omega \boldsymbol{A}_n \bullet \boldsymbol{t}_m + \Phi_n^- - \Phi_n^+ && (5.31) \\ Z_{mn}(\boldsymbol{M}_S) &= \left(\hat{\boldsymbol{n}}_i \times \frac{\boldsymbol{g}_n}{2}\right) \bullet \boldsymbol{t}_m \\ &\quad + \left(\iint_S \nabla G_i \times \boldsymbol{g}_n \, dS'\right) \bullet \boldsymbol{t}_m && (5.32) \end{aligned}$$

where $\boldsymbol{A}_n$ and Φ_n are given by the definitions of $\boldsymbol{A}$ and Φ, (5.5) and (5.8), respectively, except that $\boldsymbol{f}_n$ has replaced $\boldsymbol{J}_S$ and the source areas are restricted to the n^{th} source regions. For the HFIE solution, the elements Z_{mn} are of the form

$$\begin{aligned} Z_{mn}(\boldsymbol{J}_S) &= -\left(\hat{\boldsymbol{n}}_i \times \frac{\boldsymbol{f}_n}{2}\right) \bullet \boldsymbol{\ell}_m \\ &\quad - \left(\iint_S \nabla G_i \times \boldsymbol{f}_n \, dS'\right) \bullet \boldsymbol{\ell}_m && (5.33) \\ Z_{mn}(\boldsymbol{M}_S) &= j\,\omega \boldsymbol{F}_n \bullet \boldsymbol{\ell}_m + \Psi_n^2 - \Psi_n^1 && (5.34) \end{aligned}$$

where $\boldsymbol{F}_n$ and Ψ_n are given by the definitions of $\boldsymbol{F}$ and Ψ, (5.6) and (5.18), respectively, except that $\boldsymbol{g}_n$ has replaced $\boldsymbol{M}_S$ and the source areas are restricted to the n^{th} source regions. The calculation of the vector and scalar potentials is detailed in the following three sections.

The elements V_m are given by

$$\begin{aligned} V_m &= \boldsymbol{E}_m^i \bullet \boldsymbol{t}_m, \quad \text{EFIE solution} && (5.35) \\ V_m &= \boldsymbol{H}_m^i \bullet \boldsymbol{\ell}_m, \quad \text{HFIE solution}\,. && (5.36) \end{aligned}$$

Once the matrices $[Z]$ and $[V]$ have been determined, the unknowns in $[I]$ may be calculated by matrix algebra. The equivalent surface currents so determined may be used to calculate fields inside or outside the scattering body, as desired.

5.5.1 Calculation of $\boldsymbol{A}$ and $\boldsymbol{F}$

The following discussion applies to both regions 1 and 2, and the subscripts have been dropped for $\boldsymbol{A}$, $\boldsymbol{F}$, ϵ, μ, and $\hat{\boldsymbol{n}}$. The vector potentials $\boldsymbol{A}_{mn}$ and $\boldsymbol{F}_{mn}$ are found by numerical integration of the Green's function over the n^{th} source region shown shaded in Fig. 5.2. The observation points $\boldsymbol{r}$ in the Green's function definition are points chosen on or near the testing vector; for this work, we obtained good EFIE and HFIE results by using one T_m^+ point and one T_m^- point. Each test point was the centroid of the smaller triangle whose nodes were the n^{th} edge nodes and the T triangle centroid. These observation points are sketched in Fig. 5.4, in which the vector potential observation points are marked by o's, the scalar potential observation points by x's.

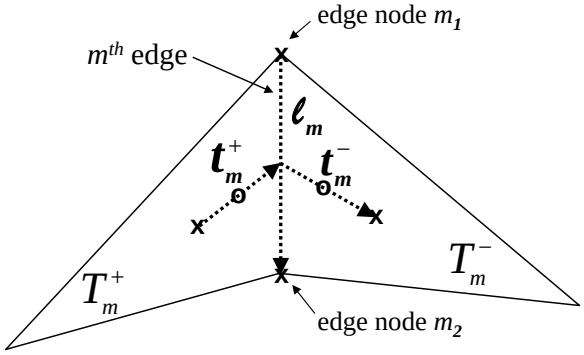

Figure 5.4: Observation points for mn^{th} vector (o) and scalar (x) potentials.

The final testing equations are written to incorporate this segmentation of the vector potential, e.g.,

$$j\,\omega \boldsymbol{A}_{mn} \bullet \boldsymbol{t}_m \;\Rightarrow\; j\,\omega\left(\boldsymbol{A}_{mn}^{+} \bullet \boldsymbol{t}_m^{+} + \boldsymbol{A}_{mn}^{-} \bullet \boldsymbol{t}_m^{-}\right) \tag{5.37}$$

$$j\,\omega \boldsymbol{F}_{mn} \bullet \boldsymbol{\ell}_m \;\Rightarrow\; \frac{j\,\omega}{2}\left(\boldsymbol{F}_{mn}^{+} + \boldsymbol{F}_{mn}^{-}\right) \bullet \boldsymbol{\ell}_m \tag{5.38}$$

where $\boldsymbol{A}_{mn}^{+}$ and $\boldsymbol{F}_{mn}^{+}$ are the vector potentials observed at $\boldsymbol{t}_m^{+}$ due to the n^{th} source region, and $\boldsymbol{A}_{mn}^{-}$ and $\boldsymbol{F}_{mn}^{-}$ are the vector potentials observed at $\boldsymbol{t}_m^{-}$ due to the n^{th} source region.

5.5.2 Calculation of $\nabla \times \boldsymbol{F}$ and $\nabla \times \boldsymbol{A}$

The dielectric EFIE contains the term $\nabla \times \boldsymbol{F}$, as shown in (5.1) and (5.2). In the corresponding testing equation,

$$\left(\frac{1}{\epsilon}\nabla \times \boldsymbol{F}_{m,n}\right) \bullet \boldsymbol{t}_m = \left(\hat{\boldsymbol{n}}^+ \times \frac{\boldsymbol{g}_n}{2}\right) \bullet \boldsymbol{t}_m^+ + \left(\hat{\boldsymbol{n}}^- \times \frac{\boldsymbol{g}_n}{2}\right) \bullet \boldsymbol{t}_m^- + \left(\iint\!\!\!\!\!\!\diagup_S \nabla G^+ \times \boldsymbol{g}_n dS'\right) \bullet \boldsymbol{t}_m^+ + \left(\iint\!\!\!\!\!\!\diagup_S \nabla G^- \times \boldsymbol{g}_n dS'\right) \bullet \boldsymbol{t}_m^- \quad (5.39)$$

where $\hat{\boldsymbol{n}}^{\pm}$ denotes the normal to the $T_m^{\pm}$ field patch and the G superscript also refers to the $T_m^{\pm}$ field patch associated with the Green's function. Because the basis function $\boldsymbol{g}_n$ is constant over the n^{th} source region, it may be moved outside the integral before the cross product is calculated. The calculation of $\nabla \times \boldsymbol{A}_{mn}$ is analogous. Thus,

$$\left(-\frac{1}{\mu}\nabla \times \boldsymbol{A}_{mn}\right) \bullet \boldsymbol{\ell}_m = -\left(\hat{\boldsymbol{n}}^+ \times \frac{\boldsymbol{f}_n^+}{2} + \hat{\boldsymbol{n}}^- \times \frac{\boldsymbol{f}_n^-}{2}\right) \bullet \frac{\boldsymbol{\ell}_m}{2} - \left(\iint\!\!\!\!\!\!\diagup_{S^{\pm}} \nabla G^+ \times \boldsymbol{f}_n^{\pm} dS' + \iint\!\!\!\!\!\!\diagup_{S^{\pm}} \nabla G^- \times \boldsymbol{f}_n^{\pm} dS'\right) \bullet \frac{\boldsymbol{\ell}_m}{2}\,. \quad (5.40)$$

5.5.3 Calculation of Φ and Ψ

We have stated in (5.8) that the electric scalar potential Φ is defined as

$$\Phi = \frac{j}{\omega\epsilon} \iint_S \nabla \bullet \boldsymbol{J}_S \; G \; dS'\,.$$

Because the basis function $\boldsymbol{f}_n$ is a pulse function, direct calculation of the $\nabla \bullet \boldsymbol{f}_n$ would produce impulse functions at the edges of the source charge region. Rather than integrating impulse functions, we will use the divergence theorem to calculate $\iint_S \nabla \bullet \boldsymbol{J}_S \; dS'$ directly. Assuming that $\nabla \bullet \boldsymbol{J}_S$ is constant over a triangular source area and given that

$$\iint_S \nabla \bullet \boldsymbol{J}_S \; dS' = \oint_C \boldsymbol{J}_S \bullet \hat{\boldsymbol{n}}_C \, dC \quad (5.41)$$

where $\hat{\boldsymbol{n}}_C$ is the unit vector normal to the contour in the plane of surface S', we can write Φ for a source triangle (shown in Fig. 5.5) as

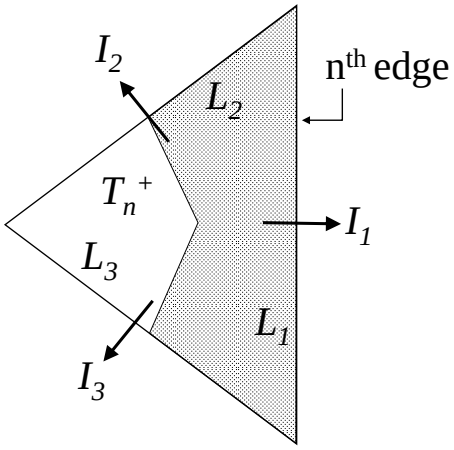

Figure 5.5: Normal electric current components for Φ calculation.

$$\Phi = \frac{j\,(I_1 L_1 + I_2 L_2 + I_3 L_3)}{\omega \epsilon \mathcal{A}} \iint_S G\, dS' \tag{5.42}$$

where I_1, I_2, and I_3 are the current components of $\boldsymbol{J}_S$ normal to the three sides; L_1, L_2, and L_3 are the side lengths; and $\mathcal{A}$ is the triangle area. Let us define the unknown electric charge density q_S^e in (5.7) as

$$q_S^e = \sum_{i=1}^{N_T} \alpha_i P_i \tag{5.43}$$

where N_T is the number of triangular patches in the model,

$$\alpha_i \;=\; \frac{j}{\omega}\left[\frac{I_{i_1}\ell_{i_1} + I_{i_2}\ell_{i_2} + I_{i_3}\ell_{i_3}}{\mathcal{A}_i}\right], \tag{5.44}$$

and

$$P_i(\boldsymbol{r}) = \begin{cases} 1, & \boldsymbol{r} \in T_i\,, \\ 0, & \text{otherwise}\,. \end{cases} \tag{5.45}$$

The electric charge associated with $\boldsymbol{J}_n$ is now spread out from S_n (in Fig. 5.2) over the two larger, triangular regions $T_n^{\pm}$; T_n^+ is drawn in Fig. 5.5. For the mn^{th} scalar potential term,

$$\Phi_{mn}^{+} = \frac{j}{\omega\epsilon}\left(\frac{I_n L_n}{\mathcal{A}^+}\boldsymbol{f}_n^+ \iint_{T_n^+} G^+ \, dS' - \frac{I_n L_n}{\mathcal{A}^-}\boldsymbol{f}_n^- \iint_{T_n^-} G^+ \, dS'\right) \tag{5.46}$$

where the superscript on G indicates that the observation point lies on T_m^+, and the potentials associated with T_n^+ and T_n^- have been differenced to obtain a result for the n^{th} edge, observed from the m^{th} edge. Φ_{mn}^- is similarly calculated with the observation point on T_m^-. Equation (5.46) applies to both regions 1 and 2.

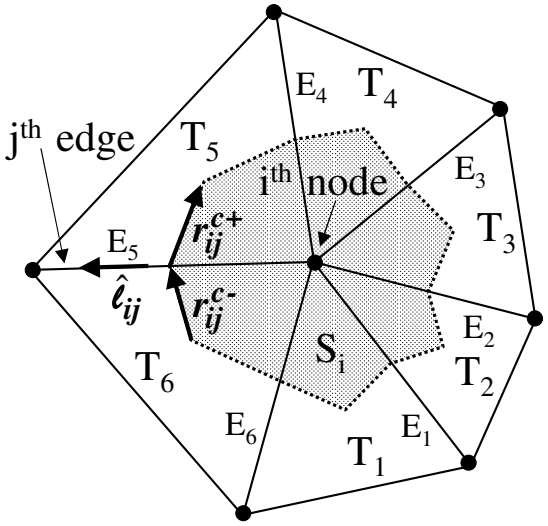

Figure 5.6: Magnetic charge source area for Ψ calculation.

To calculate the scalar magnetic potential, we likewise start by defining areas of magnetic charge associated with each edge current $\boldsymbol{M}_n$. Let us define the unknown charge density q_S^m in (5.17) as

$$q_S^m = \sum_{i=1}^{N_N} \alpha_i P_i \tag{5.47}$$

where N_N represents the total number of nodes (vertices) in the model, α_i is a scalar to be determined, and

$$P_i(\boldsymbol{r}) \;=\; \begin{cases} 1, & \boldsymbol{r} \in S_i\,, \\ 0, & \text{otherwise}\,. \end{cases} \tag{5.48}$$

In (5.48), S_i is the i^{th} charge patch, formed by connecting the centers of the edges and the centroids of the triangles associated with the i^{th} node, as shown by the shaded area in Fig. 5.6. Again making use of the divergence theorem, we can write Ψ for the i^{th} source patch as

$$\Psi = \frac{j}{\omega\mu} \iint_S \nabla \bullet \boldsymbol{M}_S \, G \, dS' \tag{5.49}$$

$$= \frac{j}{\omega\mu} \oint_C \boldsymbol{M}_S \bullet \hat{\boldsymbol{n}}_C \, dC \iint_S G \, dS' \tag{5.50}$$

$$= \frac{j}{\omega\mu\mathcal{A}_i} \left\{ \sum_{j=1}^{N_E} I_{ij} \left[\hat{\boldsymbol{\ell}}_{ij} \bullet (\hat{\boldsymbol{n}}_{ij}^{+} \times \boldsymbol{r}_{ij}^{c+} + \hat{\boldsymbol{n}}_{ij}^{-} \times \boldsymbol{r}_{ij}^{c-}) \right] \right\} \left\{ \iint_S G dS' \right\} \tag{5.51}$$

where $\hat{\boldsymbol{\ell}}_{ij}$ and $\hat{\boldsymbol{n}}_{ij}^{\pm}$, respectively, represent the unit vector along the j^{th} edge connected to node i and the outward unit vector normal to the plane of the $T_{ij}^{\pm}$ triangle associated with the j^{th} edge connected to node i. The vector $\boldsymbol{r}_{ij}^{c-}$ extends from the centroid of the T_{ij}^{-} triangle to the center of the j^{th} edge, while $\boldsymbol{r}_{ij}^{c+}$ extends from the edge center to the centroid of the T_{ij}^{+} triangle. N_E represents the total number of edges connected to node i and $\mathcal{A}_i$ is the area of S_i. From (5.51), we see that α_i in (5.47) is

$$\alpha_i = \frac{j}{\omega\mathcal{A}_i} \sum_{j=1}^{N_E} I_{ij} \left[\hat{\boldsymbol{\ell}}_{ij} \bullet (\hat{\boldsymbol{n}}_{ij}^{+} \times \boldsymbol{r}_{ij}^{c+} + \hat{\boldsymbol{n}}_{ij}^{-} \times \boldsymbol{r}_{ij}^{c-}) \right] . \tag{5.52}$$

In order to calculate Ψ_{mn}, we will use the positive and negative magnetic charge patches, designated S_{n1} and S_{n2} respectively, associated with the n^{th} edge and shown in

Fig. 5.7. We will find the normal components of $\boldsymbol{g}_n$ flowing across the mutual boundary, designated $\boldsymbol{r}_n^{c+}$ and $\boldsymbol{r}_n^{c-}$ in Fig. 5.7. The value of Ψ_{mn}^1, the scalar potential at the n^{th} edge as observed from node 1 on the m^{th} edge, is

$$\begin{aligned}
\Psi_{mn}^1 &= \frac{j}{\omega\mu\mathcal{A}_{S_{n1}}}\boldsymbol{g}_n \bullet \left(\hat{\boldsymbol{n}}_n^+ \times \boldsymbol{r}_n^{c+} + \hat{\boldsymbol{n}}_n^- \times \boldsymbol{r}_n^{c-}\right)\left(\iint_{S_{n1}} G^1 dS'\right) \\
&\quad -\frac{j}{\omega\mu\mathcal{A}_{S_{n2}}}\boldsymbol{g}_n \bullet \left(\hat{\boldsymbol{n}}_n^+ \times \boldsymbol{r}_n^{c+} + \hat{\boldsymbol{n}}_n^- \times \boldsymbol{r}_n^{c-}\right)\left(\iint_{S_{n2}} G^1 dS'\right) \\
&= \frac{j}{\omega\mu}\boldsymbol{g}_n \bullet \left(\hat{\boldsymbol{n}}_n^+ \times \boldsymbol{r}_n^{c+} + \hat{\boldsymbol{n}}_n^- \times \boldsymbol{r}_n^{c-}\right) \\
&\quad \left(\frac{1}{\mathcal{A}_{S_{n1}}}\iint_{S_{n1}} G^1 dS' - \frac{1}{\mathcal{A}_{S_{n2}}}\iint_{S_{n2}} G^1 dS'\right). \qquad (5.53)
\end{aligned}$$

In (5.53), the superscript on G refers to the end of the m^{th} edge where the observation is made. A similar calculation is done to find Ψ_{mn}^2. The equations are the same for regions 1 and 2.

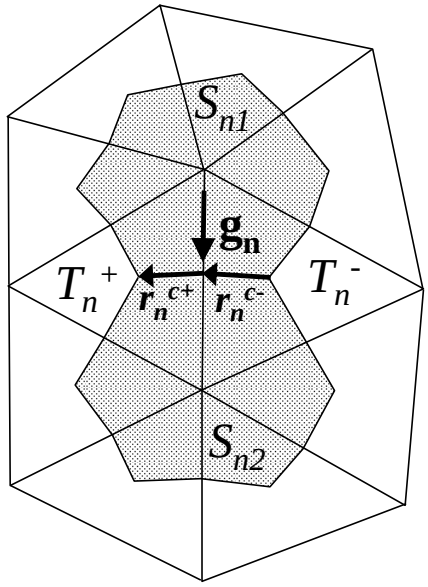

Figure 5.7: Magnetic source patches S_{n1} and S_{n2} for Ψ_{mn} calculation.

5.5.4 Testing the Incident Fields

We test the $\boldsymbol{V}$ matrix as follows:

$$V_m = \boldsymbol{t}_m^+ \bullet \boldsymbol{E}^{i+} + \boldsymbol{t}_m^- \bullet \boldsymbol{E}^{i-}, \quad \text{EFIE solution} \tag{5.54}$$

where $\boldsymbol{E}^i$ is evaluated at the vector potential test points, near the midpoints of the test vectors $\boldsymbol{t}$.

$$V_m = \boldsymbol{\ell}_m \bullet \boldsymbol{H}^i, \quad \text{HFIE solution} \tag{5.55}$$

where $\boldsymbol{H}^i$ is evaluated at the midpoint of the test vector $\boldsymbol{\ell}$.

5.6 Numerical Examples

The scattering solution using an orthogonal pair of pulse basis vectors is demonstrated by calculating the bistatic RCS for four composite cases: a dielectric sphere close to a PEC sphere, a dielectric cone capped with a PEC disk, a missile composed of a dielectric nose cone and a PEC cylinder, and a cube capped with PEC plates at opposite ends. The geometries are shown in Figs. 5.8 and 5.13; the EFIE solution method was employed for all four cases. In addition, the two-spheres problem was also solved by using the HFIE.

In the first problem, a dielectric sphere of radius 0.2 λ and $\epsilon_R = 4$ and a PEC sphere of radius 0.3 λ are situated on the z-axis. There is a gap of 0.1 λ between them, and a plane wave traveling in the -z direction impinges on the dielectric sphere first. The dielectric sphere mesh has 324 edges, or $N_D = 324$, while the conducting sphere mesh has 750 edges, or $N_C = 750$. The bistatic RCS results are shown for the pulse basis MoM EFIE and HFIE solutions and compared to a body of revolution (BOR) MoM solution in Fig. 5.9. The vertical axis represents RCS normalized by the region 1 wavelength.

In the second problem, a dielectric cone has height = 0.6 λ, radius = 0.3 λ, and $\epsilon_R = 2$. The circular end of the cone is covered by a PEC disk. Because the EFIE solution was chosen and the disk was PEC, it was allowable to model the disk as an open body in

contact with the closed dielectric cone portion of the figure, thus reducing the size of the required PEC mesh. The results are shown for $N_D = 741$ and $N_C = 205$. For an HFIE solution, the disk would be modeled as a closed body having a larger mesh. The plane wave was assumed to be traveling in the -z direction, and the bistatic RCS is shown in Fig. 5.10 for the pulse basis MoM solution, again compared to a BOR MoM solution.

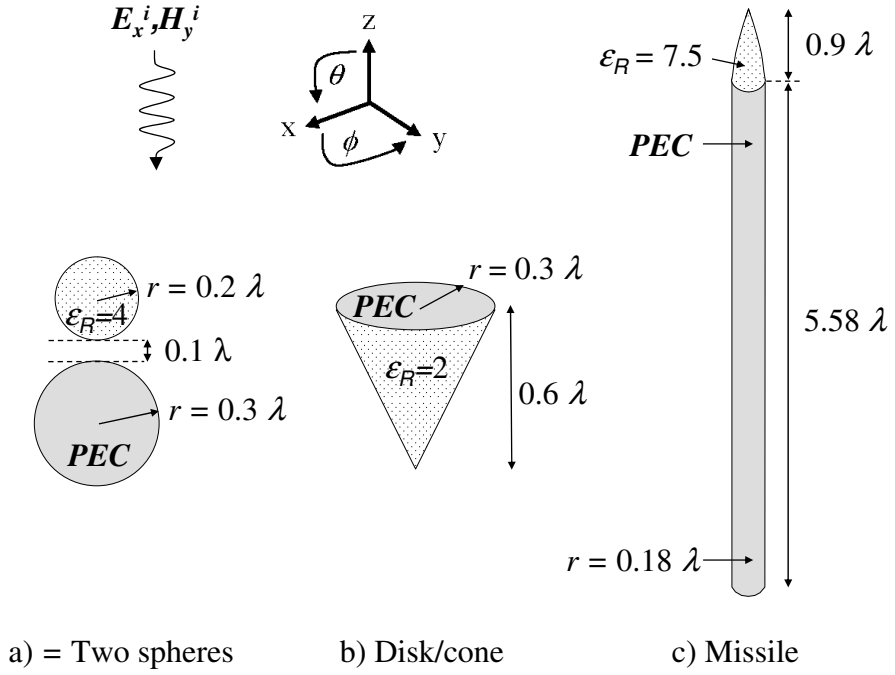

Figure 5.8: Geometries for which bistatic RCS was calculated, including a) two spheres, b) a disk/cone, and c) a missile.

In the third problem, an air-to-air missile shape was selected having a curved dielectric nose cone with length = 0.9 λ and $\epsilon_R = 7.5$. The PEC cylinder has length = 5.58 λ and radius = 0.18 λ. $N_D = 483$, while $N_C = 3681$. A plane wave was assumed to be traveling in the -z direction, toward the nose. The bistatic RCS is shown for the pulse basis MoM EFIE solution in Fig. 5.11. Additional results are shown in Fig. 5.12 for the case where the incident wave is traveling in the +z direction, toward the tail.

In the fourth problem, a dielectric cube having length = 0.1 λ and $\epsilon_R = 4$ is sandwiched between two PEC plates and the structure is irradiated from below as shown in Fig. 5.13.

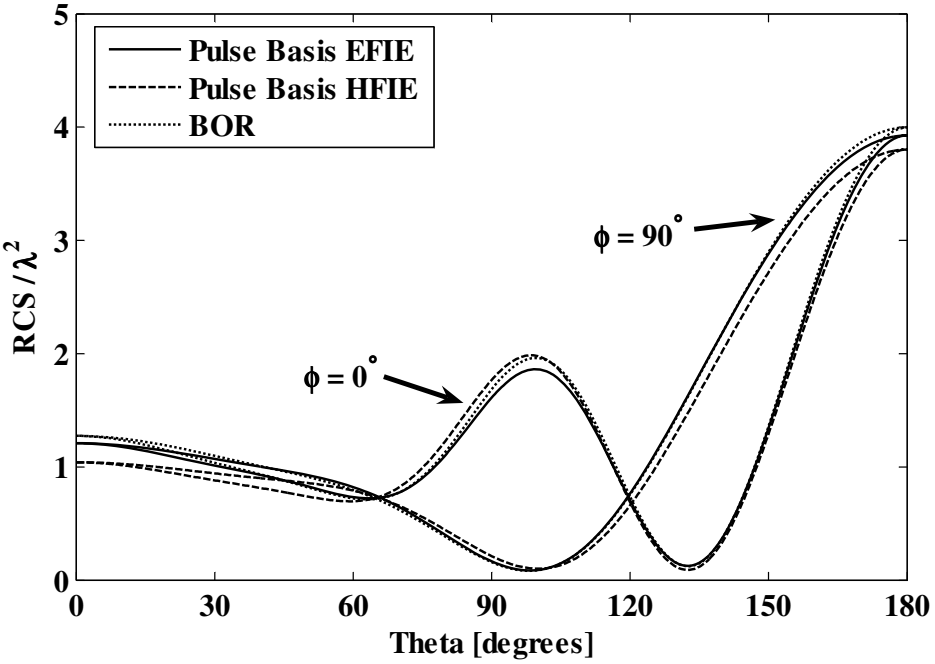

Figure 5.9: Bistatic RCS for two nontouching spheres, one dielectric, $\epsilon_R = 4$, and one PEC.

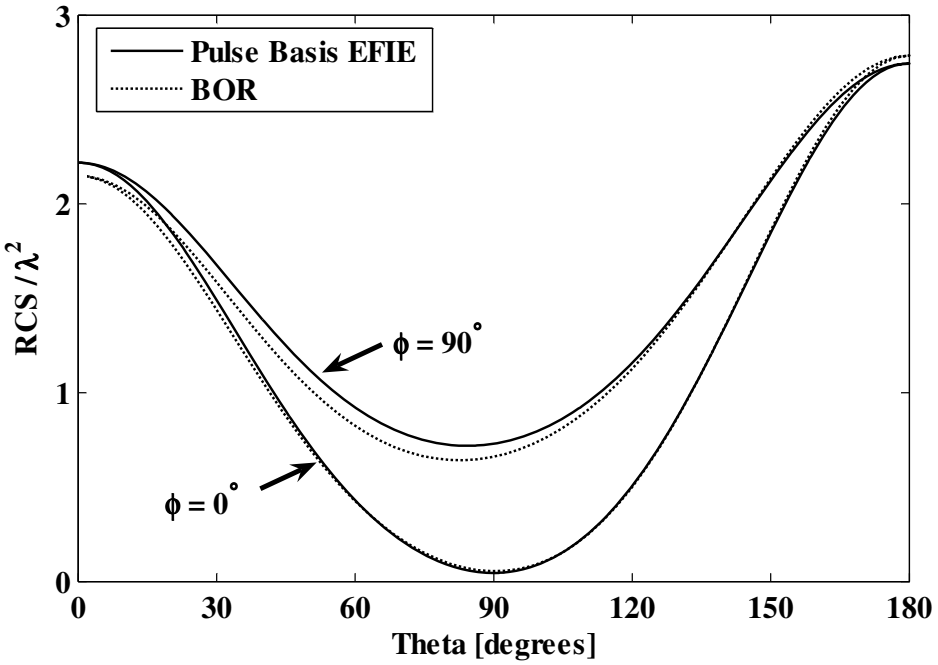

Figure 5.10: Bistatic RCS for a composite disk/cone, cone $\epsilon_R = 2$, PEC disk.

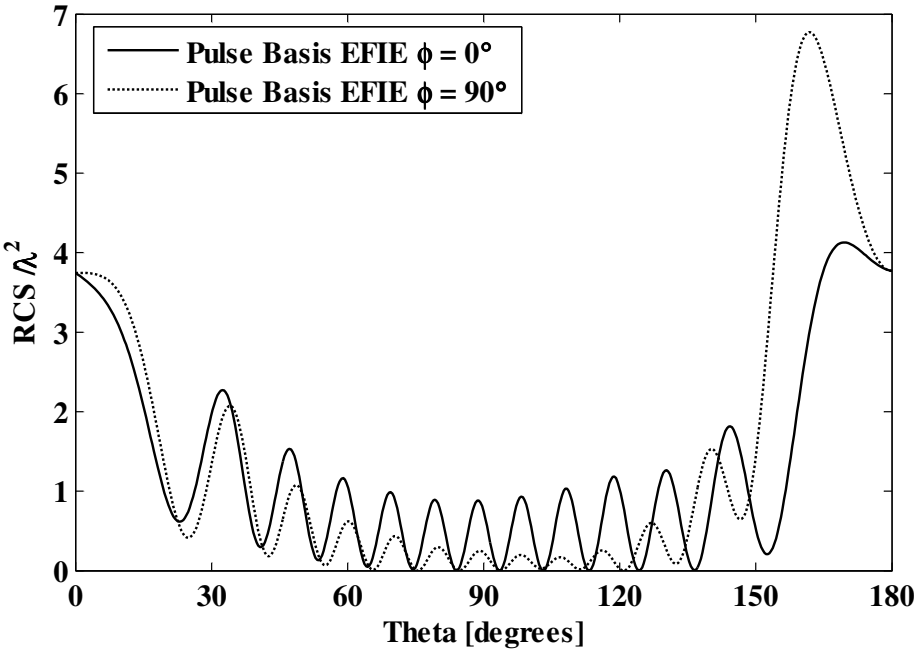

Figure 5.11: Bistatic RCS for a composite missile, nose cone $\epsilon_R = 7.5$, PEC cylinder, incident wave approaching the nose of the missile.

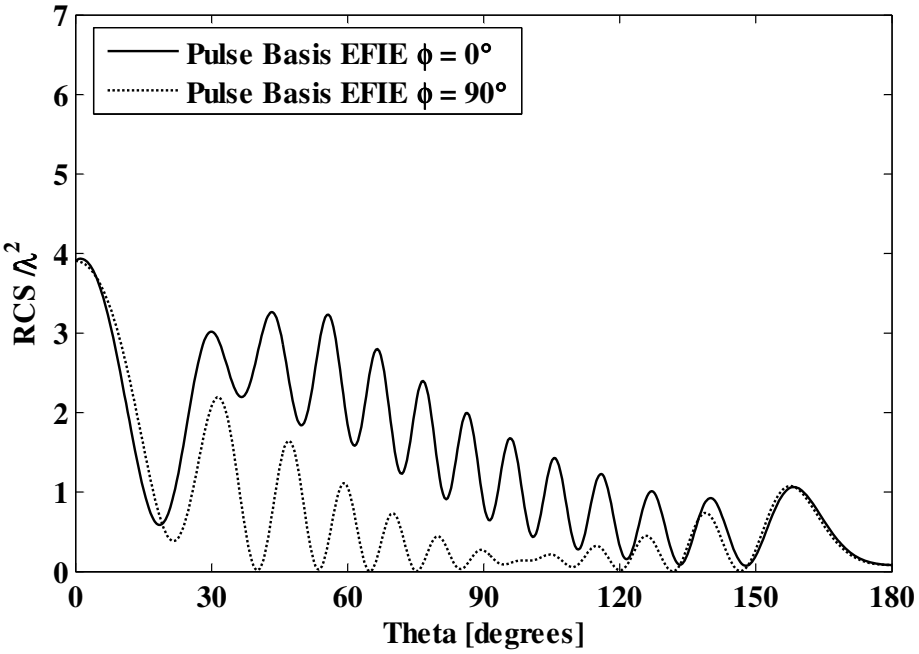

Figure 5.12: Bistatic RCS for a composite missile, nose cone $\epsilon_R = 7.5$, PEC cylinder, incident wave approaching the tail of the missile.

Two pulse basis EFIE results are shown for the structure, one obtained by using a coarse mesh and one using a finer mesh. For the coarse mesh, $N_D = 144$ and for each plate, $N_C = 20$. For the finer mesh, $N_D = 909$ and for each plate, $N_C = 136$. The normalized bistatic RCS in dB is shown in Figs. 5.14 and 5.15 and compared with combination volume integral equation (VIE) and surface integral equation (SIE) results from Sarkar et al. [41]. Their formulation used 192 unknowns for the dielectric volume currents and 32 unknowns for the PEC plate currents.

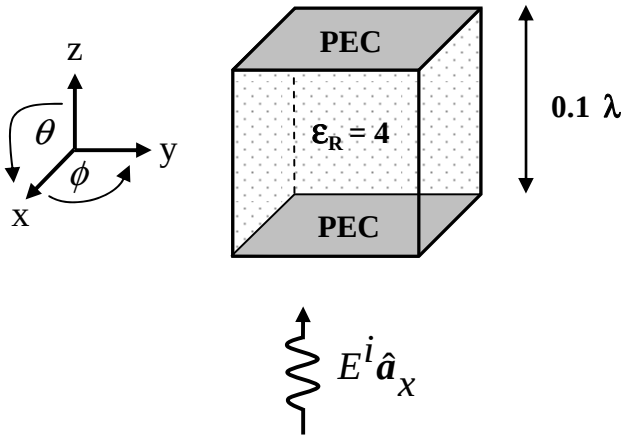

Figure 5.13: Dielectric cube of length $0.1\,\lambda$ capped with PEC plates, $\epsilon_R = 4$.

The graphical results show very good agreement between RCS plots calculated with orthogonal pulse basis vectors and their corresponding BOR plots. In the example of the dielectric cube with PEC plates at top and bottom, the pulse basis and VIE/SIE methods similarly indicate a deep null at $\theta = 90°$ in the $\phi = 0°$ RCS curve (Fig. 5.14). Compared to the finely meshed pulse basis RCS curve (Fig. 5.15), the coarsely meshed pulse basis RCS curve at $\phi = 90°$ more closely resembles the VIE/SIE results of Sarkar et al., who also used a coarse mesh for the PEC plates. Finer meshes show convergence to an almost flat $\phi = 90°$ RCS curve.

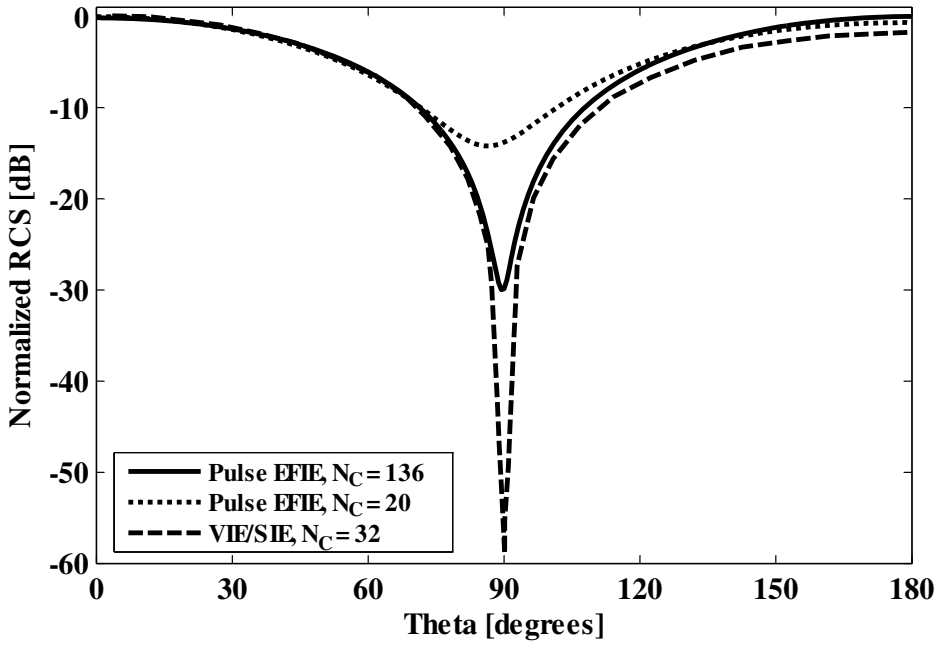

Figure 5.14: Bistatic RCS at $\phi = 0°$ for a dielectric cube of length $0.1\,\lambda$ capped with PEC plates, $\epsilon_R = 4$.

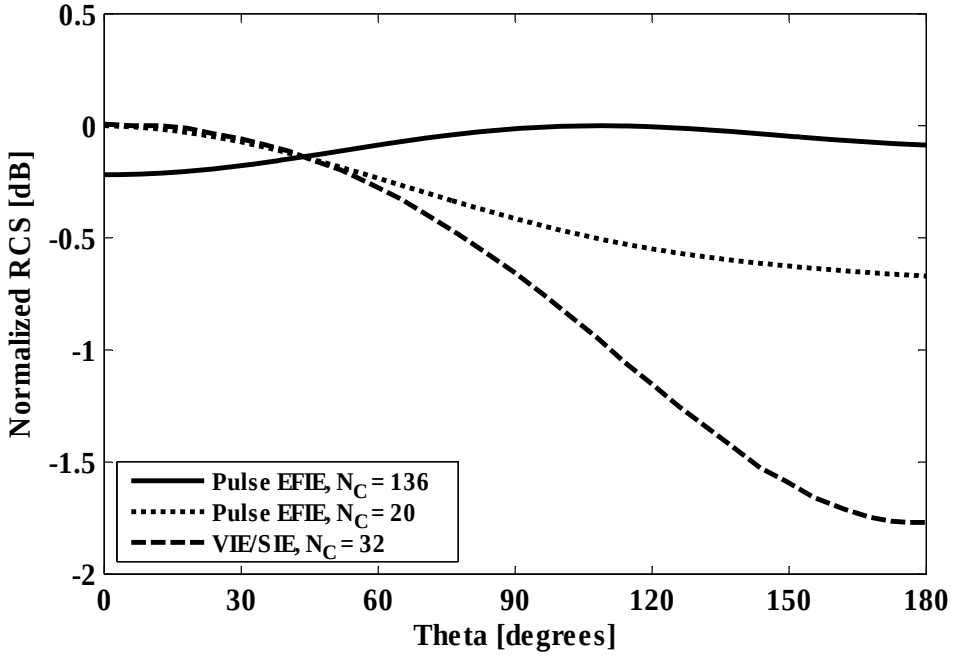

Figure 5.15: Bistatic RCS at $\phi = 90°$ for a dielectric cube of length $0.1\,\lambda$ capped with PEC plates, $\epsilon_R = 4$.

5.7 Summary

We have demonstrated the solution of PEC/dielectric composite scattering problems by using a pair of orthogonally placed pulse basis vectors. These basis functions, which model equivalent electric and magnetic surface currents, allow for the correct implementation of the EFIE and HFIE for dielectric bodies. In addition, the electric current pulse basis vector allows the implementation of the EFIE and HFIE for PEC bodies. For the example composite EFIE solutions, the EFIE has been implemented with $\boldsymbol{f}$ and $\hat{\boldsymbol{n}} \times \boldsymbol{g}$ basis vectors and $\boldsymbol{t}$ testing vectors. The corresponding composite HFIE solutions for closed bodies required $\hat{\boldsymbol{n}} \times \boldsymbol{f}$ and $\boldsymbol{g}$ basis vectors and $\boldsymbol{\ell}$ testing vectors. By arithmetically combining the EFIE and the HFIE expanded with pulse basis vectors, the CFIE may be used to guarantee unique solutions for composite scattering problems.

Chapter 6

Conclusion

We have demonstrated a new pair of basis functions for the solution of dielectric scattering problems by the method of moments (MoM) surface integral method. These basis functions may be used for perfect electric conductor (PEC), dielectric, or composite structures. They are particularly advantageous for PEC/dielectric composites, offering a simpler solution method than has been previously published. The basis functions are designed for use with triangular meshing, which is a convenient way to mesh three-dimensional objects of arbitrary shape. While there are MoM techniques that offer more accurate solutions for specialized geometries, we expect that the numerical procure developed here will allow quite accurate solutions for most shapes of objects. It is therefore a solution of very wide applicability.

In the surface integral problem solution, an electric surface current $\boldsymbol{J}$ and a magnetic surface current $\boldsymbol{M}$ are determined for each mesh edge. For the n^{th} mesh edge, $\boldsymbol{J}_n$ is expanded by the associated $\boldsymbol{f}_n^+$ and $\boldsymbol{f}_n^-$ basis vectors over a portion of the adjacent triangles, and $\boldsymbol{M}_n$ is expanded by the associated $\boldsymbol{g}_n$ basis vector over the same area. The vectors $\boldsymbol{f}_n^+$ and $\boldsymbol{f}_n^-$ are perpendicular to the edge, while $\boldsymbol{g}_n$ is parallel to the edge; each basis function is a unit vector. The orthogonality of the basis function pair within each triangle and their relationship to the testing vectors is the key to the correct numerical solution of the dielectric electric field integral equation (EFIE) and magnetic field integral equation (HFIE). We showed that the pulse basis vectors will correctly solve dielectric and composite problems in a straightforward manner.

An important part of the development of the numerical procedure was the representation of the electric and magnetic vector and scalar potentials in the expanded matrix equations. Each vector potential component was expressed as a surface integral of the basis

functions over a current source patch; the components were then summed. Each scalar potential component was expressed as the sum of contour integrals of the normal components of the basis functions out of two charge source patches; the components were then differenced.

Using canonical figures, we showed the numerical method and scattering results for PEC bodies using $\boldsymbol{f}$ or $\boldsymbol{g}$ basis functions for an EFIE solution. For dielectric bodies, we showed $\boldsymbol{f}$ and $\boldsymbol{g}$ basis functions used in EFIE and HFIE solutions. Finally, for composite bodies, we showed $\boldsymbol{f}$ and $\boldsymbol{g}$ basis functions used in EFIE and HFIE solutions. Both methods were detailed so that the combined field integral equation (CFIE) solution could be implemented if desired for closed bodies. Application of this method for composites should be more efficient and accurate than previous surface integral methods.

A future problem to solve with paired pulse basis functions would be a composite problem where one body is partly embedded in the other. Then, layered or coated bodies would be a further application of interest.

Bibliography

[1] M. I. Skolnik, *Introduction to Radar Sytems*. New York: McGraw-Hill Book Company, 1980, p. 34.

[2] R. F. Harrington, *Time-Harmonic Electric Fields*. New York: McGraw-Hill, 1961.

[3] R. F. Harrington, *Field Computation by Moment Methods*. New York: Macmillan, 1968.

[4] J. R. Mautz and R. F. Harrington, "H-field, E-field, and combined-field solutions for conducting bodies of revolution," *AEU*, vol. 32, pp. 157–164, Apr. 1978.

[5] Y. Chang and R. F. Harrington, "A surface formulation for characteristic modes of material bodies," *IEEE Trans. Antennas Propagat.*, vol. AP-25, no. 6, pp. 789–795, Nov. 1977.

[6] J. R. Mautz and R. F. Harrington, " Electromagnetic scattering from a homogeneous material body of revolution," *AEU*, vol. 33, pp. 71–80, Feb. 1979.

[7] C. Müller, *Foundations of the Mathematical Theory of Electromagnetic Waves*. Berlin, Germany: Springer, 1969.

[8] P. Moon and D. E. Spencer, "Eleven Coordinate Systems" and "The Vector Helmholtz Equation," Ch. 1 and 5 in *Field Theory Handbook, Including Coordinate Systems, Differential Equations, and Their Solutions, 2nd ed.* New York: Springer-Verlag, pp. 1–48 and 136–143, 1988.

[9] C. A. Balanis, *Advanced Engineering Electromagnetics*. New York: John Wiley & Sons, 1989.

[10] J. H. Richmond, "Scattering by a dielectric cylinder of arbitrary cross section shape," *IEEE Trans. Antennas Propagat.*, vol. AP-13, pp. 334–341, Mar. 1965.

[11] R. G. Kouyoumjian, L. Peters, Jr., and D. T. Thomas, "A modified geometrical optics method for scattering by dielectric bodies," *IEEE Trans. Antennas Propagat.*, vol. AP-11, pp. 690–703, Nov. 1963.

[12] A. W. Biggs and S. B. McMillian, "Analytical study of the bistatic radar cross-section of a prolate spheroid," Final Report for the Air Force Office of Scientific Research, Contract No. AFOSR-79-0105, The University of Kansas Center for Research, Inc., Mar. 1980.

[13] J. B. Keller, "Geometrical Theory of Diffraction," *J. Opt. Soc. Amer.*, vol. 52, no. 2, pp. 116–130, Feb. 1962.

[14] P. Y. Ufimtsev, "Approximate computation of the diffraction of plane electromagnetic waves at certain metal bodies," *Sov. Phys.-Tech. Phys.*, pp. 1708–1718, 1957.

[15] Molinet, "Geometric theory of diffraction part II: extensions and future trends of the theory," *IEEE Antennas and Propagat. Soc. Newsletter*. pp. 5–16, Oct. 1987.

[16] C. Eftimiu, "Electromagnetic scattering by rough conducting circular cylinders–I: angular corrugation," *IEEE Trans. Antennas and Propagat.* vol. 36, no. 5, pp. 651–658, May 1988.

[17] C. Eftimiu, "Electromagnetic scattering by rough conducting circular cylinders–II: axial corrugation," *IEEE Trans. Antennas and Propagat.* vol. 36, no. 5, pp. 659–663, May 1988.

[18] M. H. Cohen, "Application of the reaction concept to scattering problems," *IRE Trans. Antennas Propagat.*, vol. AP-3, pp. 193–199, Oct. 1955.

[19] D. R. Rhodes, "On the theory of scattering by dielectric bodies," Rept. 475-1, Antenna Lab, The Ohio State University, Columbus, Jul. 1953.

[20] M. G. Andreasen, "Back-scattering cross section of a thin, dielectric, spherical shell," *IRE Trans. Antennas Propagat.*, vol. AP-5, pp. 267–270, Jul. 1957.

[21] S. Govind, D. R. Wilton, and A. W. Glisson, "Scattering from inhomogeneous penetrable bodies of revolution," *IEEE Trans. Antennas Propagat.*, vol. AP-32, no. 11, pp. 1163–1173, Nov. 1984.

[22] K. K. Mei, "Unimoment method for solving antenna and scattering problems," *IEEE Trans. Antennas and Propagat.*, vol. AP-22, pp. 760–766, Nov. 1974.

[23] R. Harrington, "Origin and development of the method of moments for field computation," *IEEE Antennas and Propagat. Society Magazine*, pp. 32–36, Jun. 1990.

[24] V. H. Rumsey, "The reaction concept in electromagnetic theory," *Phys. Rev.*, Series 2, vol. 94, pp. 1483–1491, Jun. 1954.

[25] L. V. Kantorovich and G. P. Akilov, *Functional Analysis in Normed Spaces*, translated by D. E. Brown, Oxford: Pergamon Press, 1964, pp. 586–687.

[26] K. K. Mei and J. G. Van Bladel, "Scattering by perfectly-conducting rectangular cylinders," *IEEE Trans. Antennas and Propagat.*, vol. AP-11, pp. 185–192, Mar. 1963.

[27] S. A. Schelkunoff, "On diffraction and radiation of electromagnetic waves," *Phys. Rev.*, vol. 56, pp. 308–316, Aug. 1939.

[28] S. M. Rao, D. R. Wilton, and A.W. Glisson, "Electromagnetic scattering by surfaces of arbitrary shape," *IEEE Trans. Antennas Propagat.*, vol. AP-30, no. 3, pp. 409–418, May 1982.

[29] J. Van Bladel, *Electromagnetic Fields*. New York: Hemisphere Publishing Corporation, 1985, p. 355.

[30] A. D. Yaghjian, "Augmented electric- and magnetic-field integral equations," *Radio Science*, vol. 16, no. 6, pp. 987–1001, Nov.–Dec. 1981.

[31] X. Q. Sheng, J.-M. Jin, J. Song, W. C. Chew, and C.-C. Lu, "Solution of combined-field integral equation using multilevel fast multipole algorithm for scattering by homogeneous bodies," *IEEE Trans. Antennas and Propagat.*, vol. 46, no. 11, pp. 1718–1726, Nov. 1998.

[32] A. A. Kishk, and L. Shafai, "Different formulations for numerical solution of single or multibodies of revolution with mixed boundary conditions," *IEEE Trans. Antennas Propagat.*, vol. AP-34, no. 5, pp. 666–673, May 1986.

[33] S. M. Rao and D. R. Wilton, "E-field, H-field, and combined field solution for arbitrary shaped three dimensional dielectric objects," *Electromagnetics*, vol. 10, pp. 407–421, Oct.–Dec. 1990.

[34] S. M. Rao, T. K. Sarkar, P. Midya, and A. R. Djordjevic, "Electromagnetic scattering from finite conducting and dielectric structures: surface/surface formulation," *IEEE Trans. Antennas and Propagat.*, vol. 39, pp. 1034–1037, Jul. 1991.

[35] D. R. Wilton, S. M. Rao, A. W. Glisson, D. H. Schaubert, O. M. Al-Bundak, and C. M. Butler, "Potential integrals for uniform and linear source distributions on polygonal and polyhedral domains," *IEEE Trans. Antennas and Propagat.*, vol. 32, pp. 276–281, Mar. 1984.

[36] A. J. Poggio and E. K. Miller, "Integral Equation Solution of Three Dimensional Scattering Problems," in *Computer Techniques for Electromagnetics*. R. Mittra, Ed., England: Pergammon, 1973, Ch 4.

[37] K. Umashankar, A. Taflove, and S. M. Rao, "Electromagnetic scattering by arbitrary shaped three-dimensional homogeneous lossy dielectric objects," *IEEE Trans. Antennas Propagat.*, vol. AP-34, no. 6, pp. 758–766, Jun. 1986.

[38] E. Arvas, A. Rahhal-Arabi, A. Sadigh, and S. M. Rao, "Scattering from multiple conducting and dielectric bodies of arbitrary shape," *IEEE Antennas and Propagation Magazine*, vol. 33, no. 2, pp. 29–36, Apr. 1991.

[39] P. Ylä-Oijala and M. Taskinen, "Well-conditioned Müller formulation for electromagnetic scattering by dielectric objects," *IEEE Trans. Antennas Propagat.*, vol. 53, no. 10, pp. 3316–3323, Oct. 2005.

[40] T. K. Sarkar, E. Arvas, and S. Ponnapalli, "Electromagnetic scattering from dielectric bodies," *Communication in IEEE Trans. Antennas Propagat.*, vol. 37, no. 5, pp. 673–676, May 1989.

[41] T. K. Sarkar, S. M. Rao, and A. R. Djordjevic, "Electromagnetic scattering and radiation from finite microstrip structures," *IEEE Trans. Antennas Propagat.*, vol. AP-38, no. 11, pp. 1568–1575, Nov. 1990.

Appendices

Appendix A

Derivation of Dielectric Field Equations

We start with Maxwell's equations in phasor form. Here, a steadily oscillating source having frequency ω is assumed and each time varying quantity is written as its complex peak value, which is understood to be multiplied by $e^{j\omega t}$.

$$\nabla \times \boldsymbol{E} = -\boldsymbol{M}_i - j\omega\mu\boldsymbol{H} \tag{A-1}$$

$$\nabla \times \boldsymbol{H} = \boldsymbol{J}_i + \boldsymbol{J}_c + \boldsymbol{J}_d = \boldsymbol{J}_i + j\omega\varepsilon\boldsymbol{E} \tag{A-2}$$

$$\nabla \bullet \boldsymbol{E} = \frac{q^e}{\varepsilon} \tag{A-3}$$

$$\nabla \bullet \boldsymbol{H} = \frac{q^m}{\mu} \tag{A-4}$$

where $\boldsymbol{E}$ and $\boldsymbol{H}$, $\boldsymbol{J}$ and $\boldsymbol{M}$ are the electric and magnetic fields and electric and magnetic currents, respectively, i, c, and d denote *impressed*, *conduction*, and *displacement*, respectively, q^e is the time-varying electric charge density, q^m is the time-varying magnetic charge density, ε is the complex permittivity, and μ is the complex permeability. In order to describe currents within a general material that may be a perfect dielectric, a lossy dielectric, or a perfect conductor, $\boldsymbol{J}_c$ and $\boldsymbol{J}_d$ have been combined as follows:

$$\boldsymbol{J}_c + \boldsymbol{J}_d = j\omega\varepsilon\boldsymbol{E} \tag{A-5}$$

$$= j\omega(\varepsilon' + \frac{\sigma}{j\omega})\boldsymbol{E} \tag{A-6}$$

$$= j\omega(\varepsilon' - j\varepsilon'')\boldsymbol{E} \tag{A-7}$$

where ε' and ε'' are the real and imaginary parts of ε, respectively, $\varepsilon'' \stackrel{\triangle}{=} \sigma/\omega$, and σ is the conductivity. For the problems concerned in this work, the source is distant from the

scatterer. Therefore, $\boldsymbol{J}_i = \boldsymbol{M}_i = 0$, and (A-1) and (A-2) may be simplified to

$$\nabla \times \boldsymbol{E} = -j\omega\mu\boldsymbol{H} \tag{A-8}$$

$$\nabla \times \boldsymbol{H} = j\omega\varepsilon\boldsymbol{E}\,. \tag{A-9}$$

We define the equivalent surface currents $\boldsymbol{J}_S$ and $\boldsymbol{M}_S$ on surface S as

$$\boldsymbol{J}_S = \hat{\boldsymbol{n}} \times \boldsymbol{H}_{tan} \tag{A-10}$$

$$\boldsymbol{M}_S = \boldsymbol{E}_{tan} \times \hat{\boldsymbol{n}} \tag{A-11}$$

where $\hat{\boldsymbol{n}}$ is a unit vector normal to the surface, pointing into the region on the side of S where the field is tangent. We further define magnetic vector potential $\boldsymbol{A}$ and electric vector potential $\boldsymbol{F}$ in relation to the scattered fields such that

$$\boldsymbol{H}^s(\boldsymbol{J}_S) = \frac{1}{\mu}\nabla \times \boldsymbol{A} \tag{A-12}$$

$$\boldsymbol{E}^s(\boldsymbol{M}_S) = -\frac{1}{\varepsilon}\nabla \times \boldsymbol{F} \tag{A-13}$$

where s denotes *scattered*. Applying (A-8) to scattered fields, substituting for $\boldsymbol{H}^s$, and rearranging terms, we obtain:

$$\nabla \times \boldsymbol{E}^s(\boldsymbol{J}_S) = -j\omega\nabla \times \boldsymbol{A} \tag{A-14}$$

$$\nabla \times \boldsymbol{E}^s(\boldsymbol{J}_S) + \nabla \times j\omega\boldsymbol{A} = 0 \tag{A-15}$$

$$\nabla \times [\boldsymbol{E}^s(\boldsymbol{J}_S) + j\omega\boldsymbol{A}] = 0\,. \tag{A-16}$$

For the problems treated in this work, we use the vector identity that says that the curl of a gradient equals 0 and equate $\boldsymbol{E}^s(J_S) + j\omega\boldsymbol{A}$ to a gradient $-\nabla\Phi$. We now invoke the Lorenz gauge condition to define the scalar electric potential Φ such that

$$\Phi = \frac{-1}{j\omega\mu\varepsilon}\nabla \bullet \boldsymbol{A}\,. \tag{A-17}$$

Given that

$$\boldsymbol{E}^s(\boldsymbol{J}_S) = -j\omega\boldsymbol{A} - \nabla\Phi\,, \tag{A-18}$$

we combine (A-18) with (A-13) to obtain the total scattered $\boldsymbol{E}$:

$$\begin{aligned} \boldsymbol{E}^s &= \boldsymbol{E}^s(\boldsymbol{J}_S) + \boldsymbol{E}^s(\boldsymbol{M}_S) && \text{(A-19)} \\ &= -j\omega\boldsymbol{A} - \nabla\Phi - \frac{1}{\varepsilon}\nabla\times\boldsymbol{F}\,. && \text{(A-20)} \end{aligned}$$

Similarly, we apply (A-9) to scattered fields and substitute for $\boldsymbol{E}^s$ to obtain

$$\nabla\times\boldsymbol{H}^s(\boldsymbol{M}_S) = -j\omega\nabla\times\boldsymbol{F} \tag{A-21}$$

$$\nabla\times\boldsymbol{H}^s(\boldsymbol{M}_S) + j\omega\nabla\times\boldsymbol{F} = 0 \tag{A-22}$$

$$\nabla\times[\boldsymbol{H}^s(\boldsymbol{M}_S) + j\omega\boldsymbol{F}] = 0\,. \tag{A-23}$$

Defining the scalar magnetic potential Ψ such that

$$\Psi = \frac{-1}{j\omega\mu\varepsilon}\nabla\bullet\boldsymbol{F}\,, \tag{A-24}$$

we equate $\boldsymbol{H}^s(\boldsymbol{M}_S) + j\omega\boldsymbol{F}$ to the gradient $-\nabla\Psi$. Now,

$$\boldsymbol{H}^s(\boldsymbol{M}_S) = -j\omega\boldsymbol{F} - \nabla\Psi\,. \tag{A-25}$$

Combining (A-25) with (A-12), we obtain the total scattered $\boldsymbol{H}$:

$$\begin{aligned} \boldsymbol{H}^s &= \boldsymbol{H}^s(\boldsymbol{M}_S) + \boldsymbol{H}^s(\boldsymbol{J}_S) && \text{(A-26)} \\ &= -j\omega\boldsymbol{F} - \nabla\Psi + \frac{1}{\mu}\nabla\times\boldsymbol{A}\,. && \text{(A-27)} \end{aligned}$$

Solving for the vector potentials yields the following:

$$\boldsymbol{A} = \mu \iint_S \boldsymbol{J}_S \frac{e^{-jkR}}{4\pi R} dS' \tag{A-28}$$

$$\boldsymbol{F} = \varepsilon \iint_S \boldsymbol{M}_S \frac{e^{-jkR}}{4\pi R} dS' \tag{A-29}$$

where S' is the source surface, $e^{-jkR}/(4\pi R)$ is the Green's function, k is the wave number $2\pi/\lambda_0$, and R is the distance from the potential evaluation point to a source point on S.

Equations (A-20) and (A-27) will be implemented at the boundary surface of the scatterer. If the scatterer is a perfect electric conductor, then $\boldsymbol{M}= 0$ and the field equations simplify to

$$\boldsymbol{E}^s = \boldsymbol{E}^s(\boldsymbol{J}_S) = -j\omega\boldsymbol{A} - \nabla\Phi \tag{A-30}$$

$$\boldsymbol{H}^s = \boldsymbol{H}^s(\boldsymbol{J}_S) = \frac{1}{\mu}\nabla \times \boldsymbol{A}\,. \tag{A-31}$$

In surface integral problems, the boundary conditions equate the tangential components of the scattered and incident fields:

$$\left[j\,\omega\boldsymbol{A} + \nabla\Phi + \frac{1}{\varepsilon}\nabla \times \boldsymbol{F}\right]_{tan} = \left[\boldsymbol{E}^i\right]_{tan} \tag{A-32}$$

$$\left[j\,\omega\boldsymbol{F} + \nabla\Psi - \frac{1}{\mu}\nabla \times \boldsymbol{A}\right]_{tan} = \left[\boldsymbol{H}^i\right]_{tan}\,. \tag{A-33}$$

Equations of the form (A-32) and (A-33) are written for each side of the boundary surface, except in the case of a PEC, where only one side need be considered. More description of these derivations is given in [2] and [9].

Appendix B

Pulse Basis Functions in EFIE and HFIE Solutions

Chapters 2 and 3 demonstrated the use of $\boldsymbol{f}$ and $\boldsymbol{g}$ basis vectors to expand the electric surface currents $\boldsymbol{J}_S$ for EFIE PEC solutions. As a point of interest, however, either set of basis functions could be also used to expand $\boldsymbol{J}_S$ for the HFIE solution. Figure B.1 shows a PEC sphere of diameter 0.18 λ illuminated by a plane wave traveling in the -z direction. The scattering problem was worked four times using either $\boldsymbol{f}$ or $\boldsymbol{g}$ basis functions in the EFIE or HFIE solution. The bistatic RCS results are shown in Fig. B.2.

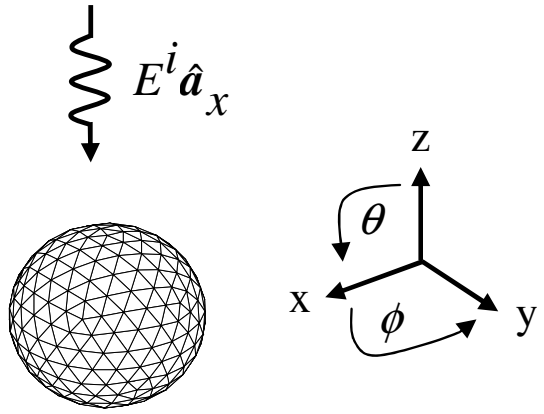

Figure B.1: Bistatic RCS for a PEC sphere, diameter = 0.18 λ.

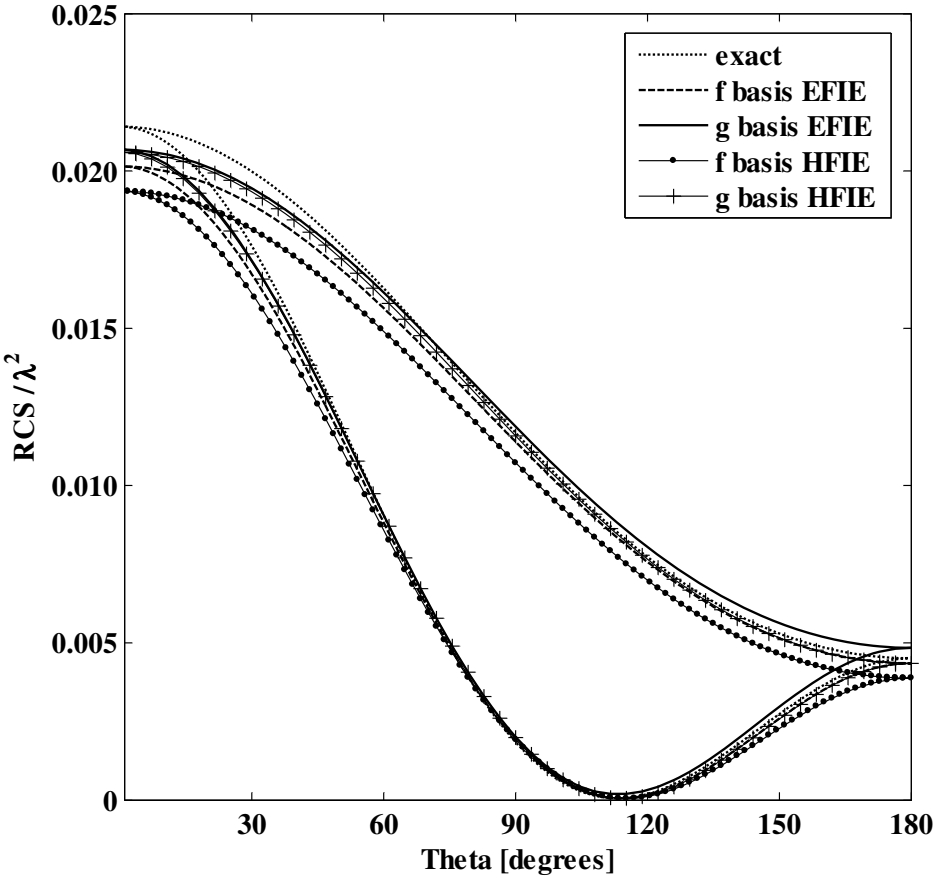

Figure B.2: Bistatic RCS for a PEC sphere, diameter = 0.18 λ.